Doctoral thesis

Studies on Imaging of Sound Field using High-speed Polarization Interferometry

February 2019

Kenji ISHIKAWA

Doctoral thesis

Studies on Imaging of Sound Field using High-speed Polarization Interferometry

February 2019

Waseda University

Graduate School of Fundamental Science and Engineering

Department of Intermedia Studies

Research on Communication Acoustics

Kenji ISHIKAWA

Contents

List of Figures

List of Tables

Acknowledgements

Foremost, I would like to express my sincere thanks to Prof. Yasuhiro Oikawa, the supervisor of my doctoral study. This study could not have accomplished without his continuous and dedicated guidance and support.

I am grateful to Prof. Yoshio Yamasaki for his helpful comments and encouragement on this study. He gave me an opportunity to start the study of the OMS when I was an undergraduate student in his laboratory. Besides, I would like to thank Prof. Tetsuya Ogata and Prof. Takashi Kawai, the referees of my thesis, for their great effort. Their insightful comments and discussions improve the quality of this thesis.

I am grateful to Dr. Kohei Yatabe for his very precise advice and discussions. I also thank Ms. Risako Tanigawa for her dedicated support to my experiments, particularly in the experiments in Chapter 7. I thank all members of Oikawa lab and Yamasaki lab. I was really enjoyed my laboratory life thanks to my friends. I would like to express my thanks to PHOTRON LIMITED, especially Dr. Takashi Onuma, Mr. Hayato Niwa, and Mr. Tomohiko Tateshima, for their world-leading technology and generous support.

Last but not least, I would like to express my deepest gratitude to everyone involved with me.

Chapter 1

Introduction

1.1 Measurement in acoustics

The terminology *measurement* is defined in the International Vocabulary of Metrology as follows: *process of experimentally obtaining one or more quantity values that can reasonably be attributed to a quantity* [1]. Informally, the measurement projects the real world onto the system of numbers. Representing a quantity by a one or more values enables us to record, compare, and evaluate the quantity. This fundamental process is the basis of all fields in modern science, engineering, economics, and society.

Acoustics, which pertain to the study related to sound and vibration, aims at understanding physical phenomena related to those. From an engineering perspective, it aims at creating a suitable acoustic environment for humans, controlling and reducing unpleasant noises, understanding and promoting speech communications, and probing information of objects and media via sound. Sound measurement is critical in all of the acoustics investigations listed above, and studies on acoustical measurements are necessary for the development of acoustics. Sound has been the subject of study since ancient Greece. In the history of acoustics, the invention of a microphone was an outstanding breakthrough. A microphone enables us to measure the acoustical quantity in terms of sound pressure. This enabled sound waves to be recorded and became the cornerstone of modern acoustics.

1.2 Microphones

1.2.1 Fundamentals

A microphone is a standard and practical instrument for sound measurement; it has sufficient accuracy, precision, dynamic range, high-stability, and easy to use in most practical applications. Further, it is used in wide varieties of commercial products.

The recording of sound, which was the long-standing dream of humans from the ancient era, using a microphone was achieved during the 19th century. As a measurement device of sound pressure, a condenser microphone is currently used, which was first described by Wente in 1917 [2]. The condenser microphone consists

of a diaphragm and backplate with a small air gap between them. The backplate is polarized by an external electric current, and the output voltage of the microphone depends on the displacement of the diaphragm imposed by sound pressure.

The quantitative measurement of sound pressure by a condenser microphone is achieved by the determination of microphone sensitivity by reciprocity pressure calibration [3, 4]. Each pair of three condenser microphones is inserted to a coupler and the product of the sensitivities is measured. From these measurements, the sensitivity of an individual microphone is determined.

1.2.2 Microphone array

A microphone array is an effective tool for obtaining the spatial information of a sound field. The microphone array has been used for many applications including speech enhancement, noise reduction, and source localization [5]. The visualization of a sound field is also an interesting topic pertaining to the microphone array. Two types of visualization exists: one displays time-averaged values such as power and intensity, and the other displays an instantaneous pressure field. Beamforming and near-field acoustic holography is often used for the former type of visualization. As the position of the sound sources can be estimated from the visualization results of those methods, they are frequently employed in the noise engineering community. On the contrary, few papers have presented the visualization of an instantaneous field by a microphone array [6] owing to the drawbacks described below.

1.2.3 Limitation of microphone measurement

A microphone presents some drawbacks although it has widely been used. A severe limitation of the microphone arises from the fact that the microphone is a contact-type sensor. As the microphone detects sound pressure at the position of the diaphragm, the microphone must be inserted into a position where the sound pressure is measured. This evokes an inevitable issue associated with a contact-type sensor: the variation in the quantity to be measured owing to the presence of the instrument itself. For sound pressure measurement by a microphone, this effect can be compensated in ideal situations: a free, pressure, or diffused field is measured by a single condenser microphone. Thus, this is not a problem provided that the simple experimental condition is satisfied. However, this causes a severe problem when a more realistic sound field is considered by complicated measurement instruments, as often the case when a microphone array is used. As the number and the density of the microphone increases, the insertion effect of the instruments increases. This might contaminate the measurement results and lead to their inaccurate interpretation. Particularly, if one considers measuring a three-dimensional sound field directly using a microphone array, the original field would not be maintained.

Another problem of the microphone is that situations occur in which the microphone cannot be used. In a flow field, a fluid flow acting on a diaphragm of a microphone imposes additional noise to the output of the microphone; further, the fluid flow is disturbed by the existence of the microphone. The microphone cannot

be used for the measurement of a sound field enclosed by objects or in a small space whose dimensions are smaller than the size of the microphone diaphragm.

These limitations arise from the contact nature of the microphone. Thus, to achieve a measurement with high-spatial-resolution or in situations where a microphone cannot be used, a non-contact sound measurement method is required. This has been achieved by using optical techniques as described in the following.

1.3 Optical measurement of sound (OMS)

The optical measurement of sound (OMS) has garnered considerable attention owing to its contactless nature. In this thesis, the OMS is defined as methods that use light as a sensing probe of pressure fluctuation or the particle velocity imposed by sound. In other words, sound pressure or acoustic particle velocity is transformed into a property of the probing light such as intensity and phase based on the physical interaction between light and sound. As light can probe a sound field and does not affect the sound field provided that the intensity of light is not too high to generate a pressure wave, no occlusion to the field exists. This is a crucial difference between the light and the microphone as an acoustic sensor. Owing to the possibility of contactless measurement, numerous studies have been conducted for measuring and imaging of sound fields using optical methods. A review of the OMS is detailed in Chapter 2.

Among the OMS, methods of which the principle relies on the acousto-optic effect (AOE) are sensitive to the sound within a probing light beam; thus, those can be regarded as a continuous sensor with respect to space, in principle. Note that the AOE is a physical phenomenon where light passing through a sound field is influenced by sound, as explained in Chapter 3. As the probing light beam contains all information of a sound field within the measurement volume, it is possible to measure a whole sound field in the volume if one can extract the information of the whole field from the light. In this context, the OMS presents a significant advantage for spatial measurement.

As sound is the temporal and spatial variation of pressure, the complete understanding of an acoustical phenomenon would be achieved by measuring both the temporal and spatial variations. As already stated, the spatial sampling of a sound field by microphones would disturb the field, and the distortion becomes larger as the density of the spatial sampling increases. Meanwhile, because the OMS is contactless, it does not disturb the sound field to be measured even if the spatial sampling frequency is high to satisfy the spatial sampling theorem. Therefore, the OMS can achieve the measurement of a whole sound field, which can be regarded as an acoustical phenomenon itself. Currently, the direct observation of a three-dimensional sound field by the OMS has not been achieved because the data measured by the OMS based on the AOE are an array of values proportional to the line integrals of sound pressure rather than point-wise sound pressure as a microphone measures. This implies that the OMS probes the projection of a sound field. Because the projection loses information along one dimension in space, a measured field by those methods is neither identical to a three-dimensional sound

field nor a slice of a three-dimensional sound field. Nevertheless, the effectiveness of the imaging of a projected two-dimensional sound field is verified by numerous previous studies.

According to the review given in Chapter 2, it is found that the instantaneous and quantitative imaging of a sound field in the air, particularly in human hearing range, has not been accomplished. As audible sound is the most important sound for humans, the measurement of such a sound field is crucial. If an optical method for the instantaneous and quantitative measurement of those fields is established, it will solve many acoustical problems including the design of transducers and musical instruments, identification of sound source positions, and understanding the physical process of noise source generation. Thus, the development of such a method is strongly desired.

1.4 Research objective and thesis organization

The objective of this research is to establish an optical method that enables an instantaneous two-dimensional sound field to be measured in a quantitative and high-speed manner, and to demonstrate the effectiveness of the proposed method in various situations in acoustics. The summary of this thesis is illustrated graphically in Fig. 1.1. To achieve the objective, an optical method named high-speed polarization interferometry is proposed. Owing to the combination of a high-speed polarization camera and parallel phase-shifting interferometry (PPSI), the quantitative imaging of a sound field with a sufficient speed of up to 1.5 MHz is achieved. Note that the proposed method, the high-speed polarization interferometry, is sometimes referred as PPSI. The quantitative measurement of the proposed method was tested by a comparison with the microphone measurement, and the validity of the obtained images was examined from numerical simulations. In addition, the proposed method was applied to existing problems in engineering acoustics, musical acoustics, aero-acoustics, and acoustic metrology; further, it was confirmed that the proposed method is a powerful tool for measurements in various acoustical situations. In particular, it is effective for investigating the generation process of sound sources owing to its ability to measure a very near field of objects and sources. The sound-imaging-method established in this study enables the measurement of sound fields that were previously impossible to measure. It is expected that the proposed method will yield new research topics in acoustics and contribute to the future development of acoustics.

The organization of this thesis is illustrated in Fig. 1.2. Chapter 2 provides a review on the OMS, of which the principle is based on acousto-optic effect (AOM). The physical theories related to the OMS are described in Chapter 3. Light propagation in a sound field in the air can be represented by using geometrical optics approximation, and the AOE can be modeled as the phase modulation of light. Therefore, to measure a sound field by the OMS, a method that enables the measurement of an optical phase map quantitatively is required. The proposed method, high-speed polarization interferometry, is described in Chapter 4 [7]. Using a high-speed polarization camera as an image sensor, the recording of a sound field with

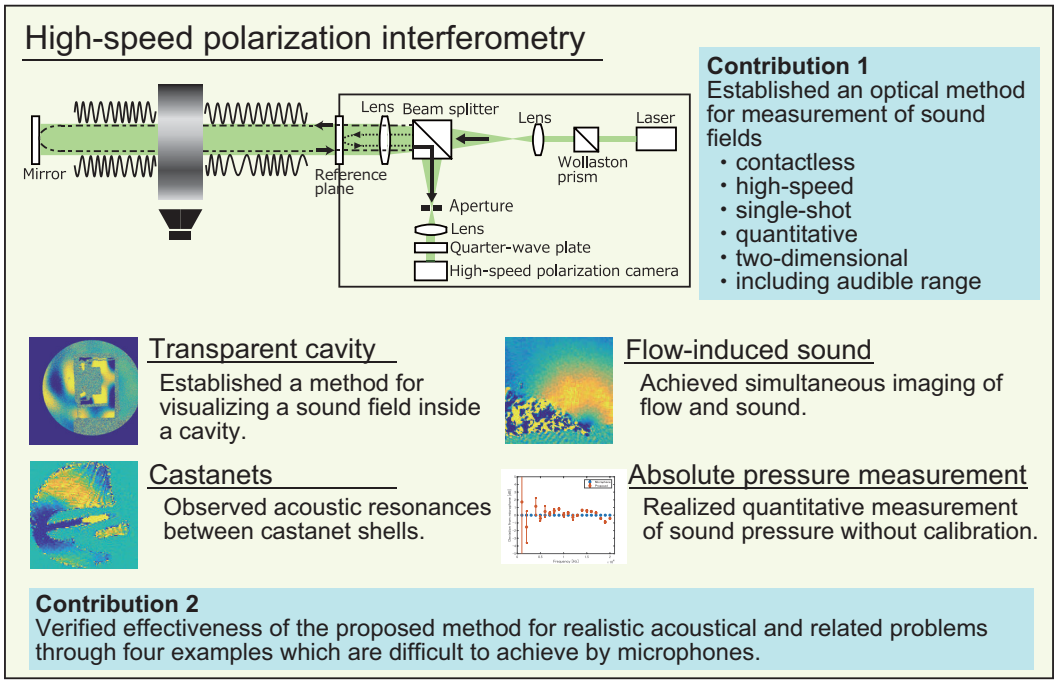

Figure 1.1: Summary of this thesis.

sufficient speed to visualize a propagating sound wave is achieved.

In Chapters 5, 6, 7, and 8, the applied measurements of the proposed method are presented. The proposed method can be applied effectively to those fields owing to its three properties: contactless, instantaneous, and quantitative. Chapter 5 describes the evaluations of transducers by the sound field visualization [8–10]. The imaging of sound fields near transducers and inside a speaker box was performed. For the imaging inside the speaker box, the box material must be transparent and the polarization state of transmitted light must be unchanged. Three transparent material: an ordinal polymethyl methacrylate (PMMA) plate, a cell-casted PMMA plate, and a silica glass plate, were tested, in which the cell-casted PMMA plate was selected. The availability of the proposed method for investigating acoustic phenomena such as radiation, propagation, and resonance is represented. In Chapter 6, the measurements of sound radiations from castanets are presented. By analyzing the near fields of the instruments, the initial waves radiated from the castanets soon after impact and frequency-dependent wavefronts were investigated. Apart from the radiating sound wave, the acoustic resonances between the castanet shells were observed. It was revealed that the first and second mode of sound radiation from the castanets were due to the acoustic resonance inside the shells. Chapter 7 presents the visualization of flow-induced sound by the proposed method [11–13]. The simultaneous imaging of flow and the sound emitted from a whistle was achieved by injecting a gas whose density was different from the surrounding air and applying time-directional filtering to balance the visibility of flow and sound. In Chapter 8, a method to reconstruct a three-dimensional sound field from a two-dimensional projection measured by high-speed polarization interfer-

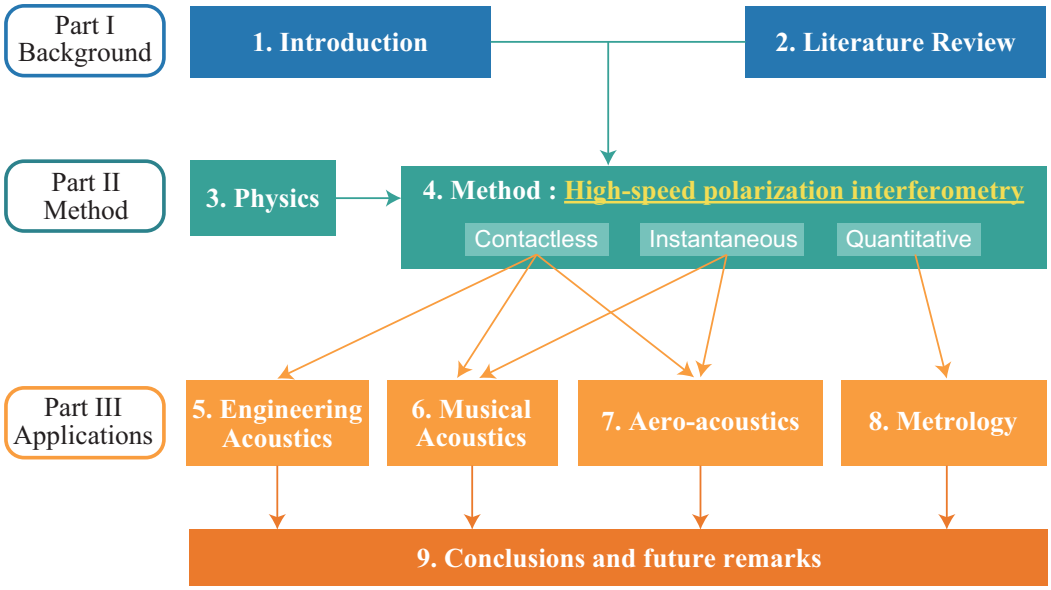

Figure 1.2: Organization of this thesis.

ometry is proposed. By assuming an axisymmetric sound field and modeling the sound field using the Helmholtz equation in the spherical coordinate, the problem is formulated as estimating the coefficients of the Helmholtz equation from the observed line-integral values. Comparison with microphone values confirmed that the proposed method can be applied to obtain a quantitative three-dimensional sound field without any calibration.

Chapter 9 summarizes this thesis and discusses future perspectives of the high-speed polarization interferometry and the OMS.

Chapter 2

Literature review of OMS

The first literature on the OMS was written by Toepler in 1867. He observed and sketched the shock waves generated by an electric spark in water by using the Schlieren optical system [14]. This visualization was based on the AOE, i.e., the modulation of light caused by sound. The AOE theory was proposed by Brillioun in 1922 [15]; ten years later, it was confirmed experimentally by Debye and Sears [16], and Lucas and Biquard [17]. Subsequently, numerous studies have been conducted to investigate the AOE [18–22] and visualize sound waves based on the AOE. The categorical review of the OMS employing the AOE is presented in the following.

2.1 Classification of OMS

The OMS can be categorized into several types based on its measurement principles. It is noteworthy that vibration and surface pressure measurement methods are not included in this review. A typical property of the OMS is to emit probing light to the measurement volume and receive it after being affected by sound. The first branch is based on how a medium is modeled. One is the continuous medium that allows for sound to be described by wave theories; the other is the discrete particles of which the number density depends on sound. When the continuous medium model is employed, the interaction of light and sound is represented by the AOE. The other uses the scattering of light caused by particles, where the intensity of the scattered light depends on a local density. The scattering methods typically seed additional particles to increase the intensity of the scattered light, except for an extreme case that uses an extremely high-power light source such that the scattered light from the air particles can be detected. The advantages of the scattering methods include the possibility of directly measuring the point-wise quantities of a sound field. On the contrary, methods based on the AOE detect integrated quantities along an optical path rather than the quantities owned by a specific point in space. This is because the transmitted light is modulated by sound wherever sound exists along the optical path [22].

The methods based on the AOE are further divided into several subcategories based on the AOE modeling. The most rigorous description of the AOE by the wave optics theory can be derived from the Maxwell equation where the refractive index

of a medium is a function of space and time, as described in Sec. 3.2. This model is, however, difficult to solve. Therefore, simpler models for describing the AOE have been developed. Theoretical treatments of the AOE had been studied from the 1930s [18–22]. The key parameters of the modeling are the ratio of the optical beam width to the acoustic wavelength, acoustic beam width, and amplitude of an acoustic wave. Based on these three factors, four models of the AOE are derived: Bragg diffraction, Raman-Nath diffraction, deflection of ray, and phase modulation. The diffraction models are appropriate for representing the strong modulation of light often caused by strain waves in solid and high-amplitude ultrasound in water. When the ratio of the optical beam width to the acoustic wavelength is much smaller than unity and the amplitude of the sound is small, as often the case for audible sound, phase modulation is suitable to describe the AOE. In this case, the modulated light can be described by only the temporal phase modulation as a function of an optical path. The deflection model is the intermediate state between the Raman-Nath diffraction and phase modulation; the ray propagating through the sound wave is characterized by a deflection angle. It is noteworthy that as no explicit border exists between them, the phase modulation model and deflection model are often used for describing the same sound field, and the choice depends on the measurement method employed.

Because the deflection and phase modulation models are used for representing weak sound fields in the air, of which measurement is the primary scope of this thesis, the following discussions focus on them. One must consider how light modulation is to be observed, especially the phase of light. Because the frequency of light is several hundreds of terahertz, the direct observation of its phase is currently impossible, and an observable property of light is its intensity. Hence, numerous methods have been studied in the optical community for a long time to observe the phase of light. Since Toepler's first visualization, lots of methods have been proposed to measure the optical phase modulation caused by acoustic waves in the air, water, and solid.

Fig. 2.1 shows the classification of the OMS based on the method to measure the phase of the modulated light. Ten methods are firstly categorized into three groups: direct observation of the intensity, methods using a lens to form the spatial Fourier transform of the wavefront, and interferometry. The following sections review the listed methods.

2.2 Direct observation: Shadowgraphy

Because sound is the phase object for light, the amplitude is not changed. However, once the wavefront of light is bent by the sound, the light forms a bright and dark contrast on a screen at a distance. Shadowgraphy is the simplest method to visualize such a pattern. The intensity distribution of the pattern is proportional to the second spatial derivative of the refractive index. Owing to its simplicity, shadowgraphy has been used for the visualization of shock waves, gas flows, and thermal convection [23]. In the field of acoustics, Pitts *et al.* visualized two-dimensional and three-dimensional sound fields generated by an underwater transducer operated at

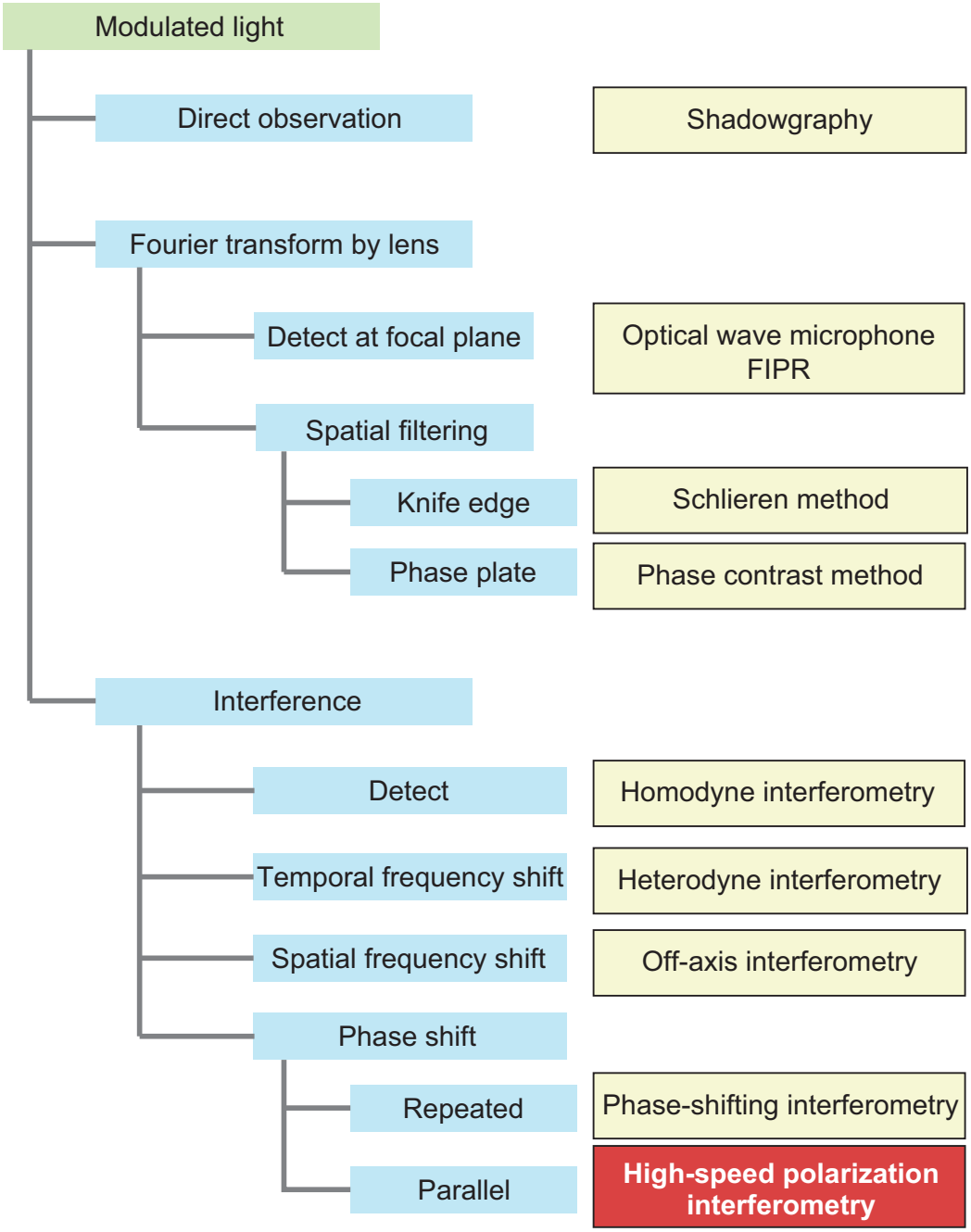

Figure 2.1: Classification of OMS

2.25 MHz using holographic shadowgraphy based on the Gabor holography [24,25]. Subsequently, shadowgraphy has been primarily used for the visualization of ultrasound in water generated by transducers operating at a frequency higher than 1 MHz [26–30]. Yuldashev *et al.* used shadowgraphy for characterizing the nonlinear propagation of spark-generated N-waves in air [31]. As the sensitivity of shadowgraphy is proportional to the second spatial derivative of the refractive index, meaning that a shorter wavelength yields a greater contrast, it is difficult to apply this method to an audible sound field. Therefore, no report regarding the shadowgraphy visualization of an audible sound field is presented.

2.3 Methods using Fourier transform by lens

Another choice is using the Fourier transform by a lens. The spatial Fourier transform of the wavefront at an aperture is formed on a focal plane of a lens. When no sound exists, the incident plane wavefront of light forms a spot at the center of the focal plane of the lens. When the wavefront is modulated by sound, its modulated components appear at a point determined by its spatial frequency on the focal plane. Therefore, observing the intensity on the focal plane or applying an optical spatial filter at the plane and performing the inverse Fourier transform enable the measurement of sound.

2.3.1 Optical wave microphone

The optical wave microphone was proposed by Sonoda *et al.* in 1994 and several papers have been published pertaining to it [32–37]. The intensity of light on the focal plane of a lens is detected by a pair of photodetectors aligned at a symmetry position against the optical axis. This method originates from the measurement technique for long-wavelength plasma waves. It was first developed for low-frequency ultrasound in the air; recently, it was applied to audible sound. The advantage of the optical wave microphone includes its simple and low-cost configuration compared with interferometric methods.

2.3.2 Fraunhofer iterative phase retrieval (FIPR)

Another method detecting the intensity of light at the focal plane of a lens is Fraunhofer iterative phase retrieval (FIPR). The sound measurement by FIPR was proposed by Kuroyama *et al.* [38]. They measured an ultrasonic standing wave at 47 kHz inside a glass cell filled with water.

2.3.3 Schlieren method

The Schlieren method is used to visualize transparent phenomena involving a change in the refractive index of a medium such as air and water [23]. A knife-edge is inserted in a focal plane of a lens, and acts as a spatial filter to cut the DC component. The inverse Fourier transform is applied by another lens and the intensity of the filtered light is detected. The intensity distribution is proportional to the spatial

derivative of the refractive index. Toepler used the Schlieren method and successfully visualized shock waves generated by an electric spark in 1867 [14]. In 1949, Barnes *et al.* reported the visualization of sound radiated from ultrasonic transducers in water [39]. The frequency of the sound was 5 MHz, and only time-averaged power maps were captured. They presented many visualization results including the reflection of sound by plates and the diffraction from an edge of an obstacle and a slit. Bucaro and Dardy established a theoretical treatment of Schlieren imaging of sound [40]. Subsequently, numerous studies had been dedicated to the Schlieren visualization of acoustic waves in water (see for example [41–53]). For the visualization in air, Bucaro and Dardy first reported ultrasonic visualizations [54]. They investigated the feasibility of the Schlieren imaging of ultrasound in air and stated that sounds of 20 kHz to 700 kHz radiated from an electrostatic transducer of diameter 15 cm excited by 100 V could be visualized. They presented the visualization of a 200-kHz ultrasound. Thirty-three years had passed since Bucaro's visualization before the first report of the Schlieren visualization of audible sound wave was introduced. This is primarily because as the sensitivity of the Schlieren method is proportional to the spatial derivative of sound pressure, therefore the sensitivity decreases as the frequency of sound decreases.

In 2010, Hargather *et al.* successfully visualized audible sound using the Schlieren method [55]. They visualized sound waves at the sound pressure level of 109.2 dB and frequency of 10 kHz, and those at sound pressure level of 102.5 dB and frequency of 15 kHz. They also developed a visibility criterion: $fp = K$, where f is the frequency of sound, p is the amplitude of sound, and K is the constant representing measurement sensitivity depending on the measurement system. In their paper, $K = 35,000$. Because they used a photograph editing software to increase the visibility of sound wave and the sensitivity constant K should depend on the image processing method, the definition of sensitivity should be reconsidered. Chitanont *et al.* proposed signal processing methods for extracting a sound field from Schlieren images [56–58]. The spatio-temporal filter bank designed based on the wave equation was used. They visualized a sound field generated by a chirp signal starting from 4 kHz. Several studies have used the Schlieren method for investigating acoustical phenomena in air. Shock waves from musical instruments such as a trumpet and trombone were visualized [59,60] and their geometrical properties were identified [61]. Karzova *et al.* reconstructed a three-dimensional pressure profile of a shock wave generated by an electric spark using Schlieren images and the Abel transform [62], and characterized the nonlinear propagation of the waves. Song *et al.* used the Schlieren method for the quantitative measurement of density gradient associated with a one-dimensional acoustic wave in a transparent duct [63].

2.3.4 Phase contrast method

The phase contrast method is a similar optical technique as the Schlieren method except for the use of a phase plate instead of a knife edge on the focal plane of a lens. This method was proposed by Zernike as a microscopic observation method [64,65]. By retarding the phase of the DC component $\pi/2$ by a phase plate, the interfer-

ence of the DC and diffracted components occurs. The intensity of the interfered light becomes the affine transformation of phase retardation imposed by sound. This method has been applied to the quantitative measurement of two-dimensional and three-dimensional sound fields in water [66–72]. To apply different phase retardations by a phase plate, the DC component and diffracted components must be separated on the focal plane. For the sound in air, especially for the audible sound, however, as the spatial frequency of sound is low, it is difficult to separate the two components on the plane. The application of the phase contrast method is, therefore, currently limited to sound fields generated by transducers in water; no attempt is reported for the use of this method to a sound field in air.

2.4 Interferometry and holography

Optical interferometry is an important measurement technique in modern science and engineering. By the superposition of two lights that are generally emitted from a single source and split into two, the phase difference between them can be observed as the intensity of interference fringes. The theoretical description of the principle is described in Section 4.1. This technique enables spatial and temporal variations in the phase of light to be obtained. Because the change in the phase is imposed by the reflection surface and medium, their geometrical and electromagnetic properties are measured.

Interferometry appeared more than 300 years ago; currently, several interferometers own the names of famous scientists such as Newton, Twyman-Green, Michaelson, Fizeau, Mach-Zehnder, and Haidinger. The breakthrough was the successful operation of the first laser by Maiman in 1960 [73]. Owing to the high spatial and spectral coherence of lasers as well as their ability to generate high-power light beams, the quality of interference fringes increased significantly. This resulted in the high accuracy measurement of small changes in length and refractive index in the order of $\lambda/100$ to $\lambda/1000$ where λ is the wavelength of light. As λ for visible light is several hundreds of nanometers, the optical interferometer can achieve length measurements of nano to angstrom order, and smaller distance measurements can be achieved by introducing specific measures.

Owing to these advantages, optical interferometry has been used for a number of science and engineering applications. The metrological standard of length is realized using an optical frequency comb generated by a mode-locked laser. The laser interferometer gravitational-wave observatory (known as LIGO) was first detected a gravitational wave in 2015. The interferometric technique is also used in many fields, for example, quantum physics, medical diagnostics, mechanics, fluid mechanics, thermodynamics, and acoustics.

The interferometric methods for sound measurement are categorized into five groups based on the method to extract the phase of light, as illustrated in Fig. 2.1. It is noteworthy that this categorization is independent of the configuration of optical systems. For example, electric speckle-pattern interferometry (ESPI), also known as TV holography or speckle interferometry, has been widely used for sound measurement since the 1990s. This term, in general, represents that either an object

or reference light forms speckles, which is independent of the method to extract the light phase. Therefore, for the proposed classification, ESPI does not appear as a certain category.

2.4.1 Homodyne and in-line interferometry

The simplest configuration of the interferometer is the homodyne and in-line type. The homodyne type indicates that the frequencies of two lights are the same, and the opposite is the heterodyne type that uses two lights of different frequencies. The in-line type implies that the spatial frequencies of two lights are the same, while the off-axis type implies that the spatial frequencies of those are different. Homodyne and in-line interferometry is the most standard and classic type.

This class of interferometry was used for the earliest studies in the 1970s. Palmer *et al.* used differential interferometry to detect the dilatational wave caused by a piezo-electric transducer operated at 8 MHz [74]. Ultrasound generated by a supersonic jet in air was observed by using the Mach-Zehnder interferometer by Smeets [75]. Clark used analog holograms to record the perturbation of refractive index caused by sound [76–78]. He observed the sound fields as the deformation of the fringes of interferograms. Homodyne interferometry has also been used with filtering [79, 80]. When a sound field is sinusoidal, the light intensity can be represented by the sum of the Bessel function. Using a band-pass filter for extracting a term containing the first order of the acoustic frequency, the filtered signal is proportional to the line integral of the sound field. More recently, the interferometry has been used for the measurement and reconstruction of two-dimensional sound fields. Ohbuchi *et al.* employed a quadrature detection system with homodyne interferometry for the reconstruction of ultrasonic sound fields in water [81–83]. The spark generated shock waves was measured using the Mach-Zehnder interferometer with a stabilization system by Yuldashev *et al.* [84]. Bertling *et al.* used laser feedback interferometry for the measurement of an ultrasonic sound field [85].

2.4.2 Heterodyne interferometry

Heterodyne interferometry is the technique to extract a phase from interferograms by imposing frequency shift to either an object or reference light. The frequency shift is often imposed by the acousto-optic modulator called the Bragg cell. The intensity of the interfered light becomes a phase-modulated signal and its modulation is caused by sound. Thus, by demodulating the signal, the phase difference between two lights, which is caused by the AOE, can be obtained. Jia *et al.* proposed the heterodyne technique for sound measurement in both air and water [86, 87]. Bou Matar *et al.* combined it with the tomographic reconstruction technique and successfully reconstructed two-dimensional sound fields [88].

A frequently used optical method for measuring and visualizing a sound field is the laser Doppler vibrometer (LDV), which often utilizes the heterodyne detection technique. A significant reason for the acceptance in the acoustics community is its commercial success. As the LDV has been widely accepted and well established as a vibration measurement instrument in both the academic and industrial community,

acousticians who wish to study sound measurement using an optical technique can obtain the instrument and are ready to start their research without considering and handling a complicated (at least for typical acousticians) optical measurement system.

The first paper, from the best of my knowledge, using the LDV for measuring sound wave was presented by Zipser and Lindner at the international congress on acoustics in 2001 [89]. They visualized an ultrasonic wave of frequency 71 kHz in air as well as the vortexes formed by an air-flow incident into an edge. In 2002, Harland *et al.* published a study regarding underwater sound pressure measurement by using the LDV [90]. A number of studies have been reported for the measurement and imaging of sound fields using the LDV [91–133]. Among them, most were regarding visualization of sound fields generated by transducers, except for the visualization of a vortex and associated pressure fluctuation [89, 96], the sound radiation from a mechanically bowed violin [105, 106], and measurement of noise generation from a jet nozzle [123]. This fact reflects the limitation of sound field imaging by the LDV owing to the requirement of scanning process: only a reproducible sound field can be visualized. Applications of the imaging by the LDV includes the identification of sound source position [104, 109, 115], acousto-optic beamformer [120], microphone calibration [127], the investigation of the Mach cone generation around a metal rod [131], and evaluation of diffused materials [132].

2.4.3 Off-axis holographic interferometry

Off-axis holographic interferometry is the technique to extract a phase map from an interferogram by imposing spatial frequency shift to the reference light. For applying the off-axis technique, the spatial distribution of interfered light must be observed. By applying a spatial filter to the recorded interferogram, the amplitude and phase map of the object light can be extracted. The off-axis configuration has been employed with an image sensor, and two-dimensional sound fields have been observed instantaneously [134–138]. Note that, although a typical hologram involves the process of reconstruction that can calculate a three-dimensional object field, the physical meaning and validity of the reconstruction process of the holography for sound measurement has not been disclosed yet.

2.4.4 Phase-shifting interferometry (PSI)

PSI introduces artificial phase retardations to reference light to calculate the quantitative phase from an interferogram. The principle of the PSI is described in Section 4.1.2.

Several types of PSIs have been used for the OMS. ESPI measures the phase of an optical wavefront from speckle patterns on an image sensor. The speckle is formed by inserting a diffuser into an optical path or using a rough surface wall as a reflector. The pioneering works on the imaging of audible sound fields using ESPI were conducted by a Norwegian research group in 1990s [139–145]. They introduced ESPI for the visualization of sound fields radiated from a loudspeaker in air. By synchronizing an optical imaging system and transducer signal, a sound

field at a certain instant can be obtained even though repeated acquisitions are necessary to apply a phase-shifting technique. Using a camera device, this method enables field information to be captured by a few acquisitions of images, and thus reduce time significantly for obtaining the two-dimensional information of sound fields. Their works include the visualization of two-dimensional projections of sound fields [139,140], reconstruction of three-dimensional sound fields by using computed tomography (CT) method [141, 142], application of their method to an underwater sound field [143], investigation of a sound field near a loudspeaker [145], and characterization of medical ultrasonic transducers [144]. Gren *et al.* applied ESPI to the imaging of a transient shock pulse generated by an electric discharge [146]. Runnemalm recorded standing waves in a rectangular duct [147]. More recently, Joost and Hinsch applied ESPI with tomographic reconstruction to the optimization of the array configuration of ultrasonic transducers consisting a parametric array speaker aimed at the maximization of radiated sound power and the minimization of the directivity of its main lobe [148]. Souris *et al.* used the Jamin interferometer and visualized a highly focused ultrasonic pulse [149]. One disadvantage of the typical PSI is that repeated measurements are required for changing the phase of the reference light. This implies that the measurable target is limited to reproducible phenomena such as sound radiation from a transducer.

The instantaneous realization of PSI for sound measurement was first reported by Wahlin *et al.* using double-pulsed holographic interferometry (DPHI) [150]; further, it was used by Schedin *et al.* for investigating transient impacted sound radiation [151, 152]. Two short pulses (25 ns) are emitted: a stationary field is firstly recorded; subsequently, a disturbed field by a sound wave is recorded onto a holographic plate. The incident angle of the reference beam is slightly changed during the two recording. Reconstruction of the two holograms yields the interference of the two recorded object lights: stationary and disturbed fields. During the rendering process, the phase of the first hologram (stationary field) was changed by certain steps, and the rendered *phase shifted* interferograms were measured by a CCD camera. According to the instantaneous recording and repeated rendering process, a transient acoustic field at a certain moment was captured. To observe the time-evolution of a phenomenon, though, repeated measurements are necessary.

2.5 Summary and challenges

2.5.1 Summary

As described above, a number of methods for the OMS based on the AOE have been studied. Table 2.1 lists the characteristics and problems of the methods. The second column indicates the measured quantities. The shadowgraphy and Schlieren method detect a value related to the spatial derivative of the optical phase; thus, the sensitivity decreases as the frequency of sound decreases. Similarly, as the LDV detects a value proportional to the time derivative of the optical phase, the sensitivity also decreases as the frequency of sound decreases. The quantitative phase can be obtained by the phase contrast method and interferometry. The phase

contrast method is effective for a high-amplitude underwater ultrasound, while an airborne sound is difficult to apply due to its measurement principle that requires the DC and diffracted components to be separated at a focal plane of a lens.

The interferometric methods can measure the sound field in air quantitatively. Among them, the LDV is most frequently used. For the imaging of a sound field, however, scanning is necessary. This limits the applicable target to reproducible sound fields such as the sound wave generated by a loudspeaker and transducer. The same is true for ESPI. Although ESPI detects a two-dimensional field by an image sensor, repeated measurements are required for the phase-shifting process. Meanwhile, DPHI and off-axis interferometry can capture a two-dimensional sound field instantaneously. Therefore, they have been used for the measurement of non-reproducible sounds such as an impacted plate [150–152] and voice [136, 137]. Because DPHI uses a holographic plate to record a sound field to be measured, only a single image is captured for a single measurement. To observe the time evolution of a sound field, repeated measurements are necessary. The off-axis interferometry can measure a two-dimensional sound field by a sufficient speed to capture the time-evolution of an acoustic phenomenon using a high-speed camera. In this sense, the off-axis interferometry and the proposed method, high-speed polarization interferometry, are similar; the difference is the method to calculate the phase from an interferogram. A problem for the off-axis interferometry is the degradation of the image quality owing to inaccuracies in the reference light and spatial filtering. Further, for the sound measurement method, the quantitative measurement of the reconstructed hologram has not been disclosed yet.

Table 2.1: Comparison of OMS. Meas.: Measured quantity, Quant.: feasibility of quantitative measurement, Inst.: feasibility of instantaneous measurement, P/2D: point or 2D measurement. ϕ denotes the phase of light, $\frac{\partial}{\partial x}$ denotes the spatial derivative, and $\frac{\partial}{\partial t}$ denotes the time derivative.

Method	Meas.	Quant.	Inst.	P/2D	Problems
Shadowgraphy	$\frac{\partial^2\phi}{\partial x^2}$	×	◯	2D	Sensitivity decreases as the frequency of sound decreases.
Optical wave microphone	ϕ	×	◯	Point	Scanning is necessary for 2D imaging. Measured value is qualitative.
Schlieren method	$\frac{\partial\phi}{\partial x}$	△	◯	2D	Sensitivity decreases as the frequency of sound decreases. Additional measures is required for quantitative measurement.
Phase contrast method	ϕ	◯	◯	2D	Modulation caused by sound has to be large so that DC and diffracted light are separated at a focal plane of a lens. Application is limited to underwater ultrasound.
LDV	$\frac{\partial\phi}{\partial t}$	◯	◯	Point	Scanning is necessary for 2D imaging. Sensitivity decreases as the frequency of sound decreases.
ESPI	ϕ	◯	×	2D	Non-reproducible sound field cannot be measured.
DPHI	ϕ	◯	◯	2D	Only a single image is obtained by single measurement; thus, high-speed measurement is impossible.
Off-axis interferometry	ϕ	◯	◯	2D	Fringe quality is degraded due to the error involved in the alignment of the reference light and spatial filtering.

2.5.2 Challenge 1: high-speed and quantitative imaging of audible sound field

Among the methods listed in Table 2.1, the imaging of an audible sound field is achieved by the optical wave microphone, Schlieren method, LDV, ESPI, and DPHI. The optical wave microphone, LDV, and ESPI require repeated measurements; thus, an instantaneous measurement cannot be achieved. The Schlieren method has been used to achieved a single-shot imaging of audible sound fields; however, a quantitative measurement is difficult. Although DPHI is capable of the instantaneous and quantitative imaging of an audible sound field at a certain moment, consecutive imaging is impossible. It is noteworthy that the off-axis interferometry proposed by Matoba *et al.* has been used to measure audible sound waves but not to visualize the audible sound fields.

Until now, the high-speed and quantitative imaging of an audible sound field has not been accomplished. This is because the requirement for the measurement system of an audible sound field is demanding. The modulation of light caused by audible sound is small, and its spatial and temporal derivatives are small as well. When light propagates 1 m where the sound pressure is 1 Pa, the phase of light changes by only 0.0232 rad. This requires a high-precision measurement of the phase. In addition, as the wavelength of the audible sound is long, a large observation area is necessary for the effective visualization of the field. Although shadowgraphy and the Schlieren method can easily achieve a large observation area, they are not suitable for the measurement of audible sound because the sensitivity of these methods decreases as the frequency of sound decreases. On the other hand, interferometry cannot easily expand the size of the measurement area because high-quality optical components and alignment are necessary to form interferometric fringes. In summary, for the measurement system of an audible sound field, a high-speed, high-precision, and large observation area has to be achieved simultaneously. These are the major reasons for the gap despite the importance of the measurement of the audible sound.

2.5.3 Challenge 2: application to existing problems

One problem of the OMS is that most of the studies measured sound fields generated by a transducer to evaluate the validity of the proposed optical method and less discussion has been conducted on how to apply the optical methods to the existing acoustic problems. Among the 125 papers cited in the review, more than 100 papers measured the sound fields generated by a transducer. Other sound sources include the electric spark [14, 31, 75, 146], impacted plate [150–152], shock wave from brass instruments [59–61], mechanically bowed violin [105, 106], jet noise [34, 36, 123], and voice [136, 137]. This indicates that the many advantages of the OMS including its contactless nature, high-spatial resolution, and feasibility of measurement of the very near field of an object, have not been utilized effectively. One reason is that the measurable targets are limited in terms of the amplitude and frequency of sound, the size of the measurement area, and requirement of the scanning process. A method with higher performance is desired, and one aspect of this problem is

discussed in the previous section. Another reason may be that most of the acoustic researchers and engineers are not aware of the advantages of using the OMS for addressing their issues. Therefore, it is necessary to verify the effectiveness of the OMS by applying it to the various existing acoustic problems.

Chapter 3

Physics of light and sound

3.1 Sound and refractive index

Acousto-optic interaction is characterized via refractive index. In wave optics, the speed of light is given by

$$c = \frac{c_0}{n}, \tag{3.1}$$

where c_0 is the speed of light in vacuum and n is the refractive index of a medium.

The relationship between refractive index and gas density can be written by the Gladstone-Dale relation:

$$n - 1 = G\rho, \tag{3.2}$$

where G is the Gladstone-Dale constant and ρ is the density of the medium. Thus, the change in density of the medium causes the change in the propagation speed of light. The relation of density and pressure of a gas is determined by the equation of state. The acoustic process can be assumed as an adiabatic process; therefore, the equation of state becomes

$$\frac{P}{\rho^\gamma} = \text{const.}, \tag{3.3}$$

where P is the pressure and γ is the specific heat ratio. By combining Eqs. (3.2) and (3.3), the refractive index and pressure becomes

$$\frac{n_1 - 1}{n_2 - 1} = \left(\frac{P_1}{P_2}\right)^{\frac{1}{\gamma}}, \tag{3.4}$$

where P_1, n_1 and P_2, n_2 are the pressure and refractive index of two states, respectively. Because the sound pressure is the deviation of instantaneous pressure from static pressure, the relation between refractive index and sound pressure becomes

$$n = (n_0 - 1)\left(1 + \frac{p}{P_0}\right)^{\frac{1}{\gamma}} + 1, \tag{3.5}$$

where n_0 and P_0 are the refractive index and pressure in the static state, respectively; n and p are the instantaneous refractive index and sound pressure, respectively. In linear acoustics, the sound pressure is much smaller than the atmospheric

pressure; Eq. (3.5) can be linearized to approximately p as follows:

$$n_{\text{linear}} = n_0 + \frac{n_0 - 1}{\gamma P_0} p. \tag{3.6}$$

The refractive index calculated by Eqs. (3.5) and (3.6) when $n_0 = 1.000279$, $P_0 = 101325$, and $\gamma = 1.4$ are plotted in Fig. 3.1, and the error imposed by the linear approximation is plotted in Fig. 3.2. The approximation error, ε_n, is calculated by

$$\varepsilon_n = \left| \frac{\Delta n - \Delta n_{\text{linear}}}{\Delta n} \right|, \tag{3.7}$$

where

$$\Delta n = n - n_0, \tag{3.8}$$

$$\Delta n_{\text{linear}} = n_{\text{linear}} - n_0. \tag{3.9}$$

The terms Δn and Δn_{linear} represent variations in the refractive index caused by sound. As shown in Fig. 3.1, the refractive index is almost linear when the sound pressure is less than 1000 Pa. The sound pressure of 1000 Pa in air only appears for special situations such as shock wave generation and a focused high-intensity ultrasonic transducer. The linear relationship between the refractive index and sound pressure thus applies in most the practical situations. The relative error imposed by the linear approximation is approximately 0.1 % when the sound pressure is 700 Pa. The non-linear effect should be considered only when the sound pressure exceeds 1000 Pa. In other words, as long as the linear acoustic theory holds, the linear approximation of the refractive index is valid. For the remainder of this thesis, Eq. (3.6) is used for the relation between the refractive index and sound pressure, and the subscript *linear* will be omitted.

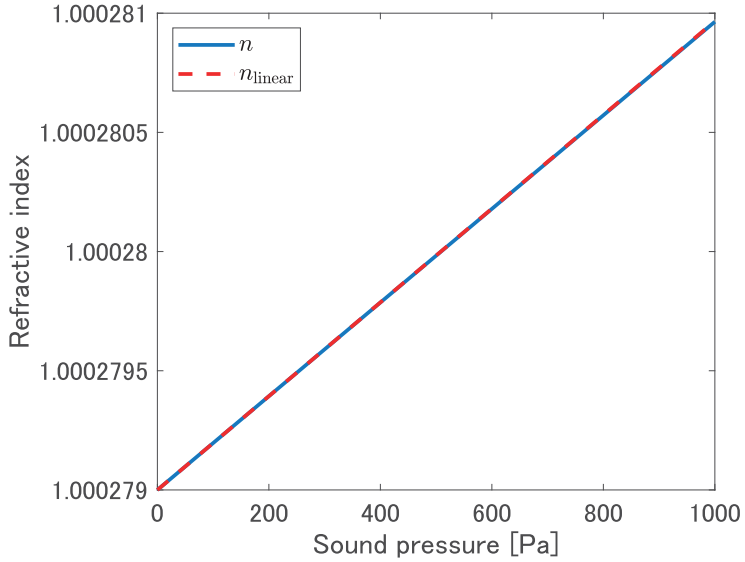

Figure 3.1: Refractive index calculated by Eqs. (3.5) and (3.6).

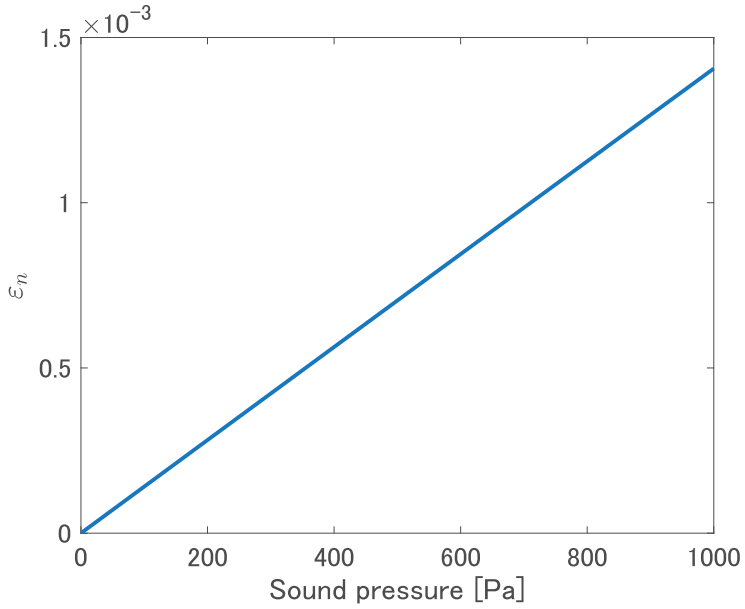

Figure 3.2: Error in the refractive index imposed by linear approximation of sound pressure.

3.2 Electro-magnetic wave in inhomogeneous media

As described in the previous section, sound causes fluctuations in the refractive index. Therefore, light propagation in a sound field can be formulated by using the optical theory in inhomogeneous media. This section describes the optical theory for the OMS, starting with the Maxwell equation and applying several approximations, which is valid for a sound field in air.

3.2.1 Maxwell equation

An electromagnetic field satisfies the following Maxwell equation defined by the Gaussian unit system:

$$\nabla \times \boldsymbol{H} - \frac{1}{c_0}\frac{\partial \boldsymbol{D}}{\partial t} = \frac{4\pi}{c_0}\boldsymbol{J}, \tag{3.10}$$

$$\nabla \times \boldsymbol{E} + \frac{1}{c_0}\frac{\partial \boldsymbol{B}}{\partial t} = 0, \tag{3.11}$$

$$\nabla \cdot \boldsymbol{D} = 4\pi\rho, \tag{3.12}$$

$$\nabla \cdot \boldsymbol{B} = 0, \tag{3.13}$$

where $\boldsymbol{E}$ is the electric vector, $\boldsymbol{D}$ is the electric displacement, $\boldsymbol{H}$ is the magnetic vector, $\boldsymbol{B}$ is the magnetic flux density, $\boldsymbol{J}$ is the current density, ρ is the charge density, and c_0 is the speed of light in a vacuum. These sets of partial differential equations hold when physical properties are continuous.

In a vacuum, the following relations hold:

$$\boldsymbol{J} = \sigma\boldsymbol{E}, \tag{3.14}$$

$$\boldsymbol{D} = \varepsilon\boldsymbol{E}, \tag{3.15}$$

$$\boldsymbol{B} = \mu\boldsymbol{H}, \tag{3.16}$$

where σ is the electrical conductivity, ε is the dielectric constant, and μ is the permeability. These equations are called material equations, and are introduced to reduce unknowns in the Maxwell equation for solving them under a given set of the charge density and current density. Although the material equations only hold in a vacuum in a rigorous manner, it is sufficiently valid in a transparent medium.

The electrical conductivity of air is the order of 10^{-15}. Assuming that no electric charge and current exists in the air, subsequently, $\sigma = 0$, $\boldsymbol{J} = 0, \rho = 0$. Substituting the material equations into the Maxwell equation under these conditions, the following equations are derived:

$$\nabla \times \boldsymbol{H} - \frac{1}{c}\frac{\partial(\varepsilon\boldsymbol{E})}{\partial t} = 0, \tag{3.17}$$

$$\nabla \times \boldsymbol{E} + \frac{1}{c}\frac{\partial(\mu\boldsymbol{H})}{\partial t} = 0, \tag{3.18}$$

$$\nabla \cdot \varepsilon\boldsymbol{E} = 0, \tag{3.19}$$

$$\nabla \cdot \mu\boldsymbol{H} = 0. \tag{3.20}$$

This set of equation shows the fundamental relations by which electro-magnetic waves in air are governed. The refractive index is defined by the dielectric constant and permeability as

$$n = \sqrt{\varepsilon\mu}. \tag{3.21}$$

As the permeability can be assumed as unity in air, the refractive index becomes

$$n^2 = \varepsilon. \tag{3.22}$$

By applying formulas of vector calculus to Eqs. (3.17) to (3.20) and deleting the magnetic terms from the equations, the equation of an electric vector can be derived as

$$\nabla^2 \boldsymbol{E} - \frac{1}{c^2}\frac{\partial^2(\varepsilon \boldsymbol{E})}{\partial t^2} + \nabla(\boldsymbol{E}\cdot\nabla(\ln\varepsilon)) = 0. \tag{3.23}$$

Here, the electric vector and dielectric constant are the functions of position and time. Eqs. (3.6), (3.22), and (3.23) are the fundamental equations of light propagation in a sound field.

3.2.2 Wave equation

The fundamental equations provide an exact solution of an electric vector to a non-magnetic medium with no electric current and electric charge in terms of the Maxwell equation. Solving the equations analytically, however, is quite difficult. Considering situations where the dielectric constant is affected only by sound, approximations can be introduced based on the fact that the temporal and spatial variations of the dielectric constant is much slower than those of the electric vector. Assuming the solution of the fundamental equations is harmonically time dependent as

$$\boldsymbol{E} = \boldsymbol{E_0}\,(\boldsymbol{r},\omega)\,\mathrm{e}^{-i\omega t}, \tag{3.24}$$

and substituting it into (3.23),

$$\nabla^2 \boldsymbol{E_0} - \frac{1}{c^2}\left(-n^2\omega^2 + i2\omega\frac{\partial n^2}{\partial t} + \frac{\partial^2 n^2}{\partial t^2}\right)\boldsymbol{E_0} + \nabla(\boldsymbol{E_0}\cdot\nabla(\ln n^2)) = 0, \tag{3.25}$$

where $\boldsymbol{E_0}$ is the complex amplitude of the electric vector and ω is the angular frequency of light. From Eq. (3.6), the time-derivatives related to the refractive index is given by

$$\frac{\partial n^2}{\partial t} = 2n_1 n\frac{\partial p}{\partial t}, \tag{3.26}$$

$$\frac{\partial^2 n^2}{\partial t^2} = 2n_1 n\frac{\partial^2 p}{\partial t^2} + 2n_1^2\left(\frac{\partial p}{\partial t}\right)^2, \tag{3.27}$$

where

$$n_1 = \frac{n_0 - 1}{\gamma p_0}. \tag{3.28}$$

Here, by considering only visible light, the angular frequency, ω is in the order of 10^{15}. Thus, the second and third terms in the bracket of the second term of Eq. (3.25) can be ignored:

$$-n^2\omega^2 + i2\omega\frac{\partial n^2}{\partial t} + \frac{\partial^2 n^2}{\partial t^2} \simeq -n^2\omega^2. \tag{3.29}$$

Thus, Eq. (3.25) becomes

$$\left(\nabla^2 + k_0^2 n^2\right)\boldsymbol{E_0} + \nabla(\boldsymbol{E_0}\cdot\nabla(\ln n^2)) = 0, \tag{3.30}$$

where k_0 is the wavenumber of light in a vacuum:

$$k_0 = \frac{\omega}{c_0}. \tag{3.31}$$

subsequently, the term related to the spatial derivative of the refractive index is given by

$$\nabla(\ln n^2) = \frac{2n_1\nabla p}{n_0 + n_1 p}. \tag{3.32}$$

Equation (3.30) is converted as

$$\nabla(\nabla\cdot\boldsymbol{E_0} + \boldsymbol{E_0}\cdot\nabla(\ln n^2)) + k_0^2 n^2\boldsymbol{E_0} = 0. \tag{3.33}$$

By substituting Eq. (3.32) into Eq. (3.33), the equation becomes

$$\nabla\left(\left(\nabla + \frac{2n_1\nabla p}{n_0 + n_1 p}\right)\cdot\boldsymbol{E_0}\right) + k_0^2 n^2\boldsymbol{E_0} = 0. \tag{3.34}$$

As the wavenumber of light is in the order of 10^7, Eq. (3.34) can be approximated by

$$\left(\nabla^2 + k_0^2 n^2\right)\boldsymbol{E_0} = 0. \tag{3.35}$$

This is the Helmholtz equation in an inhomogeneous media for a monochromatic wave field. By transforming Eq. (3.35) into the time domain, the wave equation for an electric vector in an inhomogeneous media can be derived as

$$\nabla^2\boldsymbol{E} - \frac{n^2}{c_0^2}\frac{\partial^2\boldsymbol{E}}{\partial t^2} = 0. \tag{3.36}$$

It is noteworthy that $\boldsymbol{E}$ and n are functions of space and time, and c_0 is constant.

3.2.3 Geometrical optics

Consider the following Helmholtz equation:

$$\left(\nabla^2 + k_0^2 n^2\right)U = 0. \tag{3.37}$$

For simplicity, a scalar quantity U is used instead of the vector field $\boldsymbol{E}$. By assuming the solution of Eq. (3.37) as the form

$$U(\boldsymbol{r}) = A(\boldsymbol{r})\mathrm{e}^{ik_0 L(\boldsymbol{r})}, \tag{3.38}$$

where $A(\boldsymbol{r})$ and $L(\boldsymbol{r})$ are real functions representing amplitude and phase, respectively. By substituting Eq. (3.38) into (3.37),

$$k_0^2(n^2 - |\nabla L|^2)A + \nabla^2 A + ik_0\left(A\nabla^2 L + 2(\nabla A)\cdot(\nabla L)\right) = 0. \tag{3.39}$$

The real part and imaginary part of the equation above must be zero, such that the following equations hold:

$$k_0^2(n^2 - |\nabla L|^2)A + \nabla^2 A = 0, \tag{3.40}$$

$$A\nabla^2 L + 2(\nabla A)\cdot(\nabla L) = 0. \tag{3.41}$$

As the period of the amplitude of light modulated by sound is almost the same as the period of the sound,

$$\left|\frac{\nabla^2 A}{k_0^2 A}\right| \simeq \left|\frac{K^2}{k_0^2}\right| \simeq 0, \tag{3.42}$$

where K is the wavenumber of sound. Thus, Eq. (3.40) becomes

$$|\nabla L|^2 = n^2. \tag{3.43}$$

This equation is known as an eikonal equation, and L is called the eikonal that represents the equiphase surface of light. Transforming Eq. (3.43) into integral form yields

$$L = \int |\nabla L| ds = \int n ds, \tag{3.44}$$

where s is the line element, and the integral is performed along an optical path. The solution of the inhomogeneous Helmholtz equation is given by

$$U(\boldsymbol{r}) = A(\boldsymbol{r})\mathrm{e}^{ik\int n ds} = A(\boldsymbol{r})\mathrm{e}^{ikn_0\int ds}\mathrm{e}^{i\phi_s} \tag{3.45}$$

where

$$\phi_s = k\frac{n_0 - 1}{\gamma P_0}\int p ds. \tag{3.46}$$

Thus, the phase of light propagating through a sound field is advanced proportionally to the line integral of the sound pressure along the optical path. It seems that the optical wavefront is immediately obtained by integrating the refractive index calculated under a given sound field. In practice, it is difficult because it is necessary to know the optical path within the medium having an arbitrary refractive index profile. For the sound field in air, as the modulation of light imposed by sound is extremely weak, the optical path can be assumed as a straight line. The phase modulation term of light, subsequently, becomes

$$\phi_s = k\frac{n_0 - 1}{\gamma P_0}\int_{x_1}^{x_2} p dx, \tag{3.47}$$

where the propagation direction of light is regarded as the x axis. From this approximation, one can easily calculate the wavefront of light from a given sound field.

3.3 Light as acoustic sensor

3.3.1 Sensitivity

The relation between light and sound is described in the previous sections. The phase of light is given by sound pressure and environmental factors. The ratio of optical-phase to line-integral-of-sound-pressure, S_{os}, is

$$S_{\mathrm{os}} = \frac{\phi_s}{\int_{x_1}^{x_2} p dx} = k_0 \frac{n_0 - 1}{\gamma P_0} [\mathrm{rad}/\left(\mathrm{Pa} \cdot \mathrm{m}\right)]. \tag{3.48}$$

For a standard atmospheric condition, $n_0 = 1.000279$, $P_0 = 101325$, and $\gamma = 1.4$; subsequently, the ratio becomes

$$S_{\mathrm{os}} = 1.97 \times 10^{-9} k_0. \tag{3.49}$$

The value S_{os} increases as the wavenumber of light increases. When the wavelength of light is 532 nm, $S_{\mathrm{os}} = 0.0232$. This indicates that when light travels 1 m through a field consisting of a plane sound wave of the amplitude of 1 Pa, the phase of light is changed by 0.0232 rad. Therefore, S_{OS} can be regarded as the sensitivity of the OMS.

3.3.2 Contactless nature of light

An important property of the OMS is its possibility in contactless measurement. As light can probe sound, no instruments and zig need to be inserted into a sound field to be measured. This feature realizes a non-invasive measurement of a field as well as the line integral nature of sound pressure.

Because the previous theoretical description assumes light as a wave, the photoelastic effect and absorption of energy by molecules are not explained; thus, sound is not influenced by light. From the viewpoint of quantum optics, however, photons may interact with molecules; thus, light influences to a sound field. In this context, light is no longer noninvasive to a sound field. In fact, several papers have reported that sound can be generated by inducing a strong laser light in air [153–157]. In these reports, a high-power pulsed laser is used. Torras-Rosell had considered this influence for the OMS in his thesis [158]. He calculated the light pressure imposed by a 1-mW laser source as 3.3 pN and concluded that *the influence of the momentum of the photons on the measurement of sound can also be disregarded* [158]. Thus, in the remainder of this thesis, the OMS is regarded as an ideal contactless measurement method.

Chapter 4

High-speed polarization interferometry

4.1 Optical interferometry

As discussed in the previous chapter, sound pressure changes the phase of light that passes through a sound field. Thus, to measure the sound field based on the AOE, the phase of light has to be observed. Because the frequency of light is several hundreds of terahertz and light exhibits the wave-particle duality, a direct observation of the temporal variation of light as a wave is currently impossible. An optical property that can be observed directly is its intensity. Hence, numerous optical methods to measure the phase of light have been studied for a long time. An accurate method to quantitatively observe the phase is interferometry. Interferometry detects the phase difference of multiple (generally two) lights.

4.1.1 Principles

Consider the interference of two lights defined by following:

$$\begin{aligned} \boldsymbol{E}_{\mathrm{obj}}(\boldsymbol{r}, t) &= \boldsymbol{E}_{0\mathrm{obj}}(\boldsymbol{r}, t)\mathrm{e}^{i(\omega t + \Delta\phi(\boldsymbol{r}, t))}, \\ \boldsymbol{E}_{\mathrm{ref}}(\boldsymbol{r}, t) &= \boldsymbol{E}_{0\mathrm{ref}}(\boldsymbol{r}, t)\mathrm{e}^{i\omega t}, \end{aligned} \tag{4.1}$$

where $\boldsymbol{E}_{0\mathrm{obj}}$ and $\boldsymbol{E}_{0\mathrm{ref}}$ are the complex amplitude vectors, and $\Delta\phi$ is the phase difference between the object and reference light. The object light represents the light that propagates through the region of interest, while the reference light assumes another path. The intensity of the interfered light is given by

$$\begin{aligned} I &= \left\langle \left| \boldsymbol{E}_{\mathrm{obj}} + \boldsymbol{E}_{\mathrm{ref}} \right|^2 \right\rangle \\ &= I_0 + I_1 \cos\Delta\phi, \end{aligned} \tag{4.2}$$

where $\langle\cdot\rangle$ denotes time averaging owing to a photodetector, $I_0 = |\boldsymbol{E}_{0\mathrm{obj}}|^2 + |\boldsymbol{E}_{0\mathrm{ref}}|^2$, and $I_1 = 2\boldsymbol{E}_{0\mathrm{obj}} \cdot \boldsymbol{E}_{0\mathrm{ref}}$. The phase difference, $\Delta\phi$, is included in the trigonometric function of the intensity of the interfered light. When the two lights are in phase, constructive interference occurs and the intensity of the interfered light becomes the

maximum, that is, $I_{\max} = I_0 + I_1$. In contrast, when the two lights have completely opposite phases, destructive interference occurs and the intensity becomes the minimum, which corresponds to $I_{\max} = I_0 - I_1$ The visibility of the interferogram, which characterizes the contrast of the interferometer, is defined as

$$v = \frac{I_{\max} - I_{\min}}{I_{\max} + I_{\min}} = \frac{I_1}{I_0}, \tag{4.3}$$

As $I_0 \geq I_1$, $0 \leq v \leq 1$. The contrast of the interferogram becomes maximal when the amplitudes of the object and reference lights are the same.

4.1.2 Phase-shifting interferometry

Although the interferogram includes the information related to the object phase, extracting $\Delta\phi$ from the intensity is difficult task. A typical scheme is the phase-shifting technique [159]. The principle is to introduce artificial phase retardations into the reference light and to perform several measurements with multiple phase retardation angles. The reference light with the phase retardation θ is rewritten as

$$\boldsymbol{E}_{\mathrm{ref}}(\boldsymbol{r}, t) = \boldsymbol{E}_{0\mathrm{ref}}(\boldsymbol{r}, t)\mathrm{e}^{i(\omega t - \theta)}. \tag{4.4}$$

Subsequently, the intensity of the interfered light becomes

$$I(\theta) = I_0 + I_1 \cos\left(\Delta\phi + \theta\right). \tag{4.5}$$

Many phase-shifting algorithms exist that estimate $\Delta\phi$ from multiple phase-shifted interferograms $\{I(\theta_1), \cdots, I(\theta_n)\}$ [159–164]. When the phase retardation angles, θ_n, are known, the phase can be calculated by

$$\Delta\phi_{\mathrm{wrap}} = \mathrm{Arg}\left[\sum_{n=1}^{N} I\left(\theta_n\right)\mathrm{e}^{-i\theta_n}\right], \tag{4.6}$$

where $\mathrm{Arg}[z]$ denotes the principal value of the complex argument of z, $i = \sqrt{-1}$, θ_n is the nth phase retardation, and N is the total number of phase retardation angles. Further, the calculated phase by Eq. (4.6) is wrapped within $[-\pi, \pi)$, as indicated by the subscript *wrap*; therefore, unwrapping should be performed:

$$\Delta\phi = U[\Delta\phi_{\mathrm{wrap}}], \tag{4.7}$$

where $U : [-\pi, \pi) \to \mathbb{R}$ denotes the phase unwrapping function. For applying this algorithm, at least three interferograms are required. Herein, a hyper ellipse fitting in a subspace method (HEFS) is employed for the phase retrieval from interferograms because the HEFS method is more robust to random noise and phase-shifting errors than the ordinary methods [163, 164].

4.2 Measurement system

4.2.1 Optical configuration

To achieve the simultaneous and quantitative measurement of a sound field, high-speed polarization interferometry is proposed. The configuration of the proposed

measurement system is depicted in Fig. 4.1. The optical components consist of a Fizeau-type polarization interferometer [165] and a high-speed polarization camera [166], thus resulting in the simultaneous acquisition of four phase-shifted interferograms known as parallel phase-shifting interferometry (PPSI) [167, 168]. The laser emits monochromatic light and it is divided into orthogonal linearly polarized components by the Wollaston prism. One is used for object beam, and another for the reference beam. The reference light is reflected by the reference plane called an optical flat. The optical flat is a polished flat surface that maintains the optical wavefront undisturbed and is frequently used for the Fizeau-type interferometer. The object light passes through both the reference plane and measurement area, reflected by the mirror, passes through the measurement area again, and turns back to the reference plane. The phase of the object light is modulated owing to the AOE. The object and reference lights are combined and reflected by the beam splitter. The aperture eliminates undesired components of the combined light and extracts only p-polarized or s-polarized light from the object light and another from the reference light. Subsequently, the quarter wave plate changes the polarization state into the superposition of the contra-rotating circular polarized light. Finally, the contra-rotating circular polarized light is detected by the high-speed polarization camera (CRYSTA, PI-1P, developed by Photron limited) [166]. The schematics of the high-speed polarization camera is shown in Fig. 4.2. The high-speed polarization camera consists of the phase-shifting array device and the image sensor. Four types of linear polarizers are mounted on each pixel of the image sensor. The azimuths of the linear polarizers are 0, $\pi/4$, $\pi/2$, and $3\pi/4$. Owing to the pixelated phase-shifting array device, the four-step phase-shifting algorithm can be applied to a single image, and a single-shot measurement of the quantitative phase map can be achieved.

The principle of the high-speed polarization interferometer can be described by using Jone's representation [169]. The incident light is divided into two orthogonal linearly polarized beams by the Wollaston prism. The p-polarized component of the object light is modulated by the sound within the measurement arm, and the s-polarized component of the reference light is given by the following, respectively:

$$\boldsymbol{E}_{\mathrm{obj}}(\boldsymbol{r},t) = E_{0\mathrm{obj}}(\boldsymbol{r},t)\begin{bmatrix}1\\0\end{bmatrix}\mathrm{e}^{i\Delta\phi(\boldsymbol{r},t)}, \tag{4.8}$$

$$\boldsymbol{E}_{\mathrm{ref}}(\boldsymbol{r},t) = E_{0\mathrm{ref}}(\boldsymbol{r},t)\begin{bmatrix}0\\1\end{bmatrix}, \tag{4.9}$$

where $E_{0\mathrm{obj}}$ and $E_{0\mathrm{ref}}$ are the amplitudes. The time-harmonic terms are omitted for simplicity. Subsequently, the two beams are combined and the polarization states of these are altered by the quarter wave plate. Consequently, the light that enters to the high-speed polarization camera becomes the superposition of the contra-rotating circular polarized light, which can be expressed by

$$\boldsymbol{E}_{\mathrm{circ}} = \frac{E_{0\mathrm{obj}}(\boldsymbol{r},t)}{\sqrt{2}}\begin{bmatrix}1\\i\end{bmatrix}\mathrm{e}^{i\Delta\phi} + \frac{E_{0\mathrm{ref}}(\boldsymbol{r},t)}{\sqrt{2}}\begin{bmatrix}1\\-i\end{bmatrix}. \tag{4.10}$$

The first term is the left-hand circular polarization and the second is the right-hand

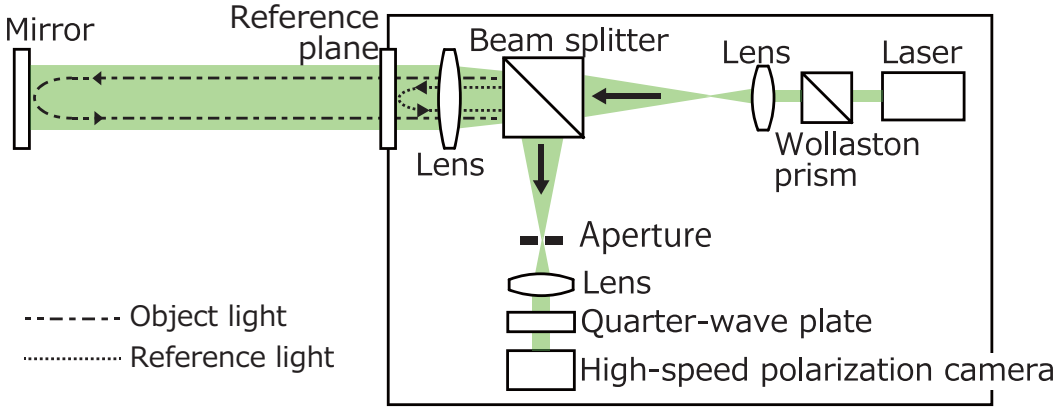

Figure 4.1: Schematic illustration of the high-speed polarization interferometer.

circular polarization. Subsequently, the light $\boldsymbol{E}_{\mathrm{circ}}$ passes through the phase-shifting array device. Because the Jones matrix representation of a linear polarizer at the azimuth θ is given by

$$\boldsymbol{P}_\theta = \begin{bmatrix} \cos^2\theta & \sin\theta\cos\theta \\ \sin\theta\cos\theta & \sin^2\theta \end{bmatrix}, \tag{4.11}$$

the intensity of the detected light becomes

$$I_{\mathrm{system}}(\theta) = \left\langle |\boldsymbol{P}_\theta \cdot \boldsymbol{E}_{\mathrm{circ}}|^2 \right\rangle = I_0 + I_1 \cos(\Delta\phi + 2\theta) = I(2\theta). \tag{4.12}$$

As the azimuths of the linear polarizers mounted on the polarization high-speed camera are 0, $\pi/4$, $\pi/2$, and $3\pi/4$, the four interferograms, $I(0)$, $I(\pi/2)$, $I(\pi)$, and $I(3\pi/2)$, are obtained simultaneously. Therefore, $\Delta\phi$ can be calculated by using Eqs. (4.6) and (4.7); additionally, $\Delta\phi$ can also be calculated by

$$\Delta\phi_{\mathrm{wrap}} = \arctan\frac{I(3\pi/2) - I(\pi/2)}{I(0) - I(\pi)}, \tag{4.13}$$

and Eq. (4.7) where $\Delta\phi_{\mathrm{wrap}}$ is the wrapped phase, $\arctan : \mathbb{R} \to [-\pi, \pi)$ is the four-quadrant inverse tangent.

4.2.2 Measurement parameters

The sampling frequency of the system is equal to the frame rate of the high-speed camera. The number of sensors, which is defined as the dimension of the image, is equal to the number of active pixels, i.e., the pixels that can record data. Typically, as the frame rate of a high-speed camera increases, the number of the active pixels decreases. The relations between frame rate and number of active pixel of the polarization high-speed camera, PI-1P, are shown in Table. 4.1. The full image (1024 pixel $\times$ 1024 pixel) is available when the frame rate is less than 7000 fps. Note that, as 2×2 pixels are used for calculating a single-phase value, the image dimension of an obtained phase map becomes half. For satisfying the temporal sampling theorem of sound, the image size becomes smaller as the frequency of

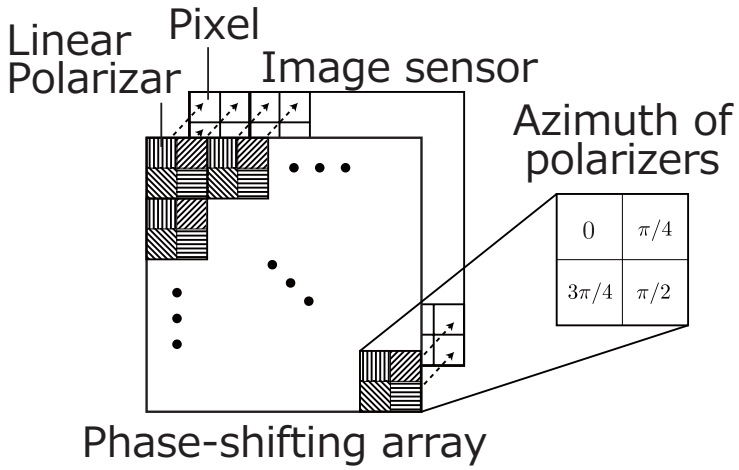

Figure 4.2: Schematic illustration of the phase-shifting array and the image sensor of the high-speed polarization camera.

Table 4.1: Relation between frame rate and number of pixels of the high-speed polarization camera.

Frame rate	Active pixels
7000	1024 × 1024
25000	512 × 512
50000	512 × 272
100000	320 × 192

sound increases. However, it is not necessary for satisfying the temporal sampling theorem; as the high-speed polarization camera does not contain an anti-alias filter, the sound wave of which the frequency is higher than the Nyquist frequency is measured as its alias frequency. The frame rate and image size should be determined by considering the required image dimension and temporal resolution.

The spatial resolution of the high-speed polarization camera is defined as the number of measurement points within a unit length. The interval of a calculated phase map is given by

$$\delta = M_L \left(2\delta_{\mathrm{sen}}\right) = \frac{D_{\mathrm{obj}}}{D_{\mathrm{sen}}} \left(2\delta_{\mathrm{sen}}\right), \tag{4.14}$$

where M_L is the magnification of lenses in the system, D_{obj} is the beam diameter of the object light, D_{sen} is the beam diameter on the image sensor, and δ_{sen} is the pixel pitch of the image sensor. The beam diameter of the object light determines the size of the measurement area. Therefore, when the number of the pixels is constant, the size of the measurement area decreases as the spatial resolution increases. This implies a tradeoff between the spatial resolution and the size of the measurement area. In our typical configuration, $D_{\mathrm{obj}} = 0.1$ m, $D_{\mathrm{sen}} = 0.018$ m, and $\delta_{\mathrm{sen}} = 20$ μm. Consequently, $\delta = 0.22$ mm, and the spatial resolution is 4500 samples per meter. By considering the fact that the wavelength of a 20-kHz sound wave as

approximately 1.7 mm, this spatial resolution is sufficient for the imaging of an audible sound field.

4.2.3 Signal processing

The calculated phase by the HEFS method contains the geometry of optical components and environmental perturbations as well as random noise. As the amplitude of the optical phase modulation caused by sound is typically much smaller than 2π, filtering is necessary to visualize the sound wave in most situations addressed herein. Choices for the dimension of filters are as follows; temporal, spatial, and spatio-temporal. Chitanont *et al.* applied a spatio-temporal filter bank to extract sound information from Schlieren videos [57]. Yatabe *et al.* proposed time-directional filters that can be applied directly to a wrapped phase [12]. In this study, time-direction filters were employed for the analysis of the measured data. Initially, the HEFS method was used to calculate the wrapped phase from the recorded interferograms. Subsequently, one-dimensional unwrapping was performed to each pixel of the wrapped phase video. Finally, a temporal filter that was designed based on the prior knowledge of a measured sound field, was applied to each pixel of the unwrapped phase video. A spatial filter was not used to preserve the spatial properties of the sound fields.

4.3 Evaluation of measurement system

4.3.1 Background noise analysis

To evaluate the measurement method, the comprehension of noise characteristics is necessary. This subsection describes the background noise of the high-speed polarization interferometer under the following conditions: the framerate of 50,000 fps, the exposure time of 1/50,000 s, the number of the recorded frames of 10,000 and the length between the lens of the interferometer and the reflective lens of 300 mm.

First, the temporal characteristics of the background noise are analyzed. The power spectrum density estimations by the Welch method of the obtained phase are plotted in Fig. 4.3(a). The averaged values of $k \times k$ pixels are plotted, where $k = 1, 2, 4, 8, 16$. As shown in the figure, the noise can be interpreted as the summation of the white noise, 1/f noise, and harmonic noises. The white noise is due to the shot noise that is the fluctuations in the number of detected photons. As theoretically expected, the level of shot noise decreases by the square root of the number of averaged points. The 1/f noise is originated from many sources including the electric circuits. The harmonic noises, which are appeared at 130 Hz, 520 Hz, and 3300 Hz, are caused by a cooling fan attached on the camera. Although the frequencies depend on the implementation of a system, such noise should occur because the cooling fans are often necessary for the high-speed imaging. If the fans cannot be stopped for camera safety, it should be eliminated by post-processing. For the imaging of a sound field, low frequency noises should be eliminated because

those primarily disturb the resultant images. For the frequencies higher than 1,000 Hz, the dominant noise source is the white noise. Several methods can be used to reduce the white noise such as by increasing the laser power and cooling optical components.

The spatial characteristics of the noise are investigated. Figure 4.3(b) shows the noise level at each pixel as the image of 128 pixels by 128 pixels. The temporal high-pass filter whose cutoff frequency is 1,000 Hz is applied to the temporal data at each pixel. The noise levels are increased around $(i, j) = (100, 50)$, where i is the horizontal pixel index and j is the vertical pixel index. This is because the unintended light reflected in the optical system yields another interference pattern, called stray light. A stray light causes the increase in the noise level by approximately 20 dB. In addition, the small non-uniformity of the noise level appears within the entire image. This is caused by non-ideal characteristics of the optical components such as the non-uniformity of lens thickness and variation in the pixel sensitivity of the image sensor. Because such spatial noises do not move during measurement, it is easily distinguished from the sound wave. However, it sometimes appears as a multiplicative noise; it is important to recognize the position and characteristics of the spatial noise before measurement. If the noises contaminate the measurement results, the optical system should be adjusted.

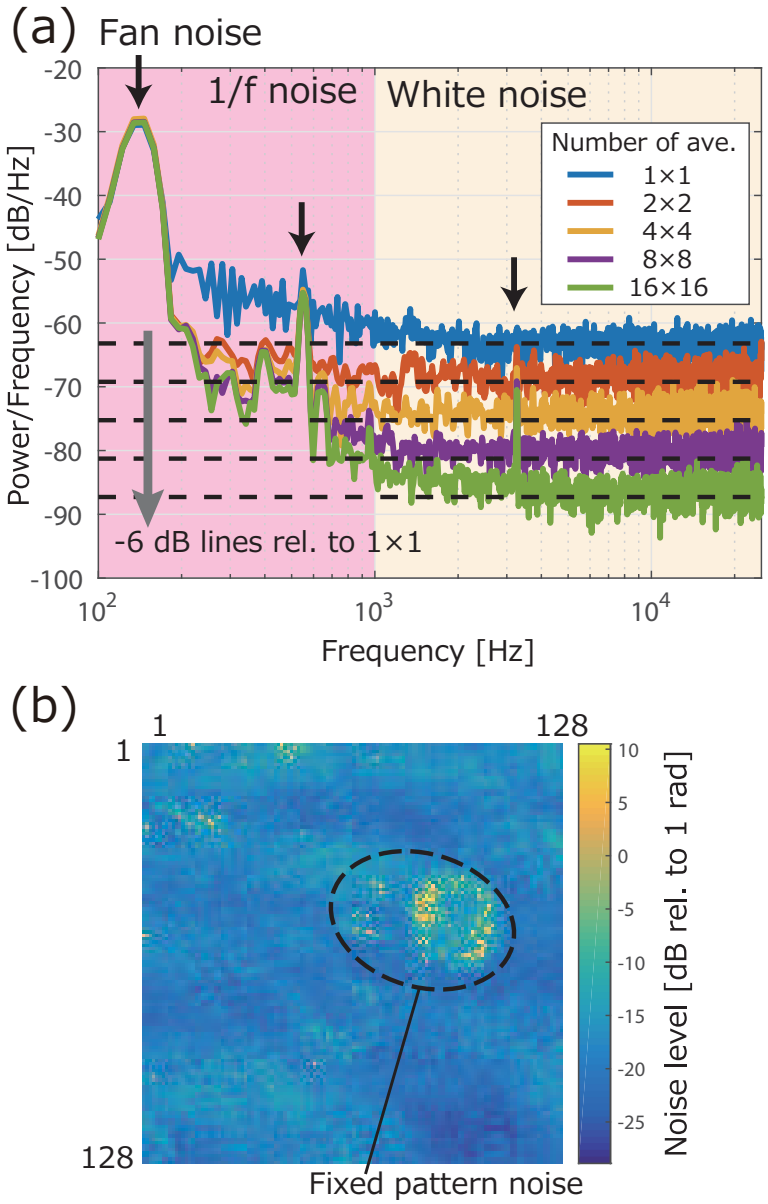

Figure 4.3: Characteristics of the background noise. (a) Power spectrum density estimations of the obtained phase. The legends denote the number of pixels for the pixel-averaging. The plots indicate the background noise characteristics. The horizontal black lines indicate the theoretical decrease in shot noise relative to the noise level of no averaging data. (b) Spatial domain representation of the background noise. The color shows the noise level of each pixel after high-pass filtering.

4.3.2 Imaging of sinusoidal sound field

To demonstrate that the high-speed polarization interferometer can image a sound field in air, the sound radiated by a transducer was measured, and it was compared with numerical simulations.

An ultrasonic transducer (MURATA MA40S4S) was used and driven by a 40-kHz sinusoidal signal with an amplitude of 7.0 V in root mean square. The frame rate of the camera was 100,000 fps and the image resolution was 96 × 160; the actual size of the measurement area was 18.8 mm × 31.3 mm. The wrapped phase was calculated using Eq. (4.7) and the Goldstein's branch-cut algorithm was used to unwrap the two-dimensional phase map. The time-averaging of 60 sequential images were calculated and subtracted from each image to remove static components in the phase maps.

For verifying the validity of the measured sound fields by the high-speed polarization interferometer, numerical simulations were conducted. Although the transducer has a disk-shaped diaphragm, it was modeled by a vibrating circular piston for simplicity. Using the Rayleigh integral of the first kind, the radiated sound field by the piston can be expressed by

$$p(\boldsymbol{r}, t) = C \int\int_S \frac{\mathrm{e}^{ik|\boldsymbol{r}-\boldsymbol{r'}|}}{|\boldsymbol{r}-\boldsymbol{r'}|} \mathrm{e}^{i\omega t} dy' dz', \tag{4.15}$$

where $\boldsymbol{r} = (x, y, z)$ is the observation position, $\boldsymbol{r'} = (x', y', z')$ is the source position on S, S is the surface of the piston, and C is the coefficient. The diameter of the piston was 6 mm. For the calculation, the integral over S was approximated by the summation of point sources lying of the piston as

$$p(\boldsymbol{r}, t) = C \sum_{m=1}^{M} \frac{\mathrm{e}^{ik|\boldsymbol{r}-\boldsymbol{r'_m}|}}{|\boldsymbol{r}-\boldsymbol{r'_m}|} \mathrm{e}^{i\omega t}, \tag{4.16}$$

where M is the number of the point sources. To simulate the line integral effect of the high-speed polarization interferometer, the integral was calculated by

$$\phi_{\mathrm{sim}}(x, y, t) = 2k \frac{n_0 - 1}{\gamma p_0} \int_0^Z p(\boldsymbol{r}, t) dz, \tag{4.17}$$

where Z is the integral distance. The multiplication by two implies the forward and backward path of light. The following values were used for the constants: $\gamma = 1.41$, $n_0 = 1.000279$, $p_0 = 101325$, $Z = 0.3$, and $M = 313$. The point sources were distributed at 0.3-mm intervals on the surface S.

To simulate the sound field quantitatively, the constant C should be determined. In this study, it was determined experimentally such that the amplitude of the reference microphone and the simulation at the corresponding position become identical. This implies that the simulated field is calibrated by the actual sound pressure value obtained from the reference microphone. The reference microphone was affixed at the 1 cm from the center of the transducer. The peak sound pressure value was 424 Pa. To achive a simulated sound pressure of 424 Pa at 1 cm from the center of point sources, C was determined as 3.94.

Figure 4.4 shows the experimental (left side) and simulated (right side) results when one transducer generates a sound field of 40 kHz. As shown in the figure, all of the experimental data were in agreement with the simulation results. These results suggest that the proposed system can measure a quantitative sound field. The phases of the sound fields agreed well, as shown in Fig. 4.4(c), while their amplitudes differed, as shown in Fig. 4.4(b). The slight differences in the pattern of the sound field can be considered as the modeling error of the transducer in the simulation because the actual transducer is a vibrating cone with a cylindrical enclosure. It can also be considered within the slight systematic bias of the measurement system.

Figure 4.5 shows the three time-sequential images of the instantaneous phase. The time step of each image was 10 μs. The blue lines in the figures indicate the position of the corresponding wavefront. Because the sound propagation distance within 10 μs is 3.4 mm when the speed of sound is 340 m/s, the experimental result agrees with the theoretical value.

Figure 4.6 shows the experimental and simulated results when two transducers were driven by the same 40-kHz signal. The interference pattern of the two sound waves appears in Fig. 4.6(a). Although noise exists in the experimental result, the interference pattern is consistent with that of the simulated result. From these experimental results, it can be concluded that the proposed system can image an instantaneous two-dimensional sound field.

4.3.3 Verification by microphone measurement

To confirm that the proposed method measured the line integral of sound pressure quantitatively, a comparison with microphone measurements was conducted. The integral was approximated by moving a microphone along the optical path. The conditions of the measurement are shown in Table 4.2. The amplitude is at the center position of the microphone; the static refractive index was calculated from the measured static pressure, temperature, and relative humidity by using Ciddor's equations [170]. The moving step of the microphone should be sufficiently small to approximate the integration with sufficient precision because that will yield a theoretical error. By calculating the error under the experimental condition, the maximum theoretical relative error is approximately 0.1%. The precision is sufficient by considering the uncertainty of the high-speed polarization interferometer.

Figure 4.7(a) shows the photograph of the experimental environment. The high-speed polarization interferometer and microphone measurements were performed separately, but the timing of both measurements to the input signal of the loudspeaker was synchronized. The microphone was affixed on the linear positioning unit and the position of the microphone was changed automatically. Figure 4.7(b) is the image of the background phase, which is the obtained phase without filtering, to highlight the position of the microphone. The microphone and the positioning unit were aligned to move parallel to the optical path. For the optical data, the averaged value within the white square, 10 pixels $\times$ 30 pixels, was used. The averaged area was chosen so as to be close to the microphone diaphragm and to avoid the fixed pattern noise. The microphone was removed from the measurement area

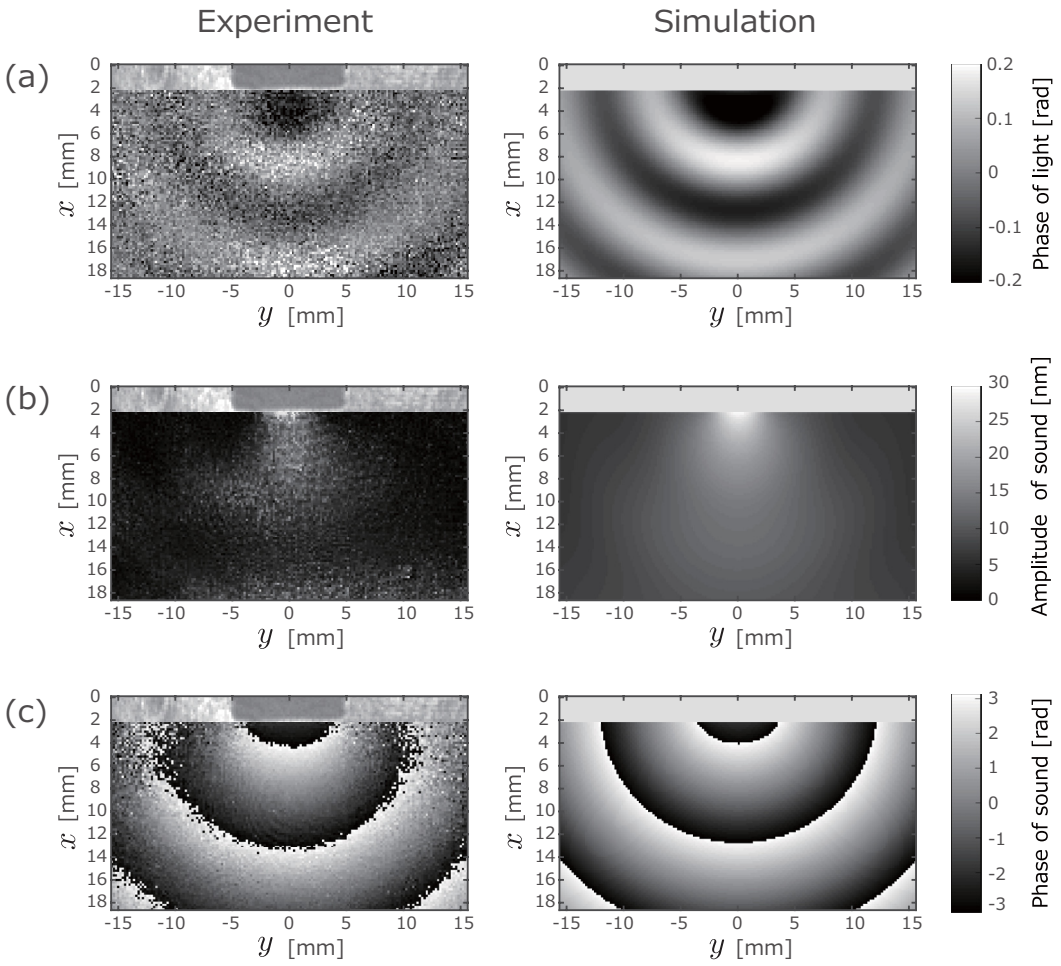

Figure 4.4: Imaging results of (a) the instantaneous phase, (b) the amplitude, and (c) the phase of the sound field generated by the transducer driven by 40 kHz.

during the optical measurement. The obtained values of the microphone were compensated by the value of the free field response of the 90° incidence of the 5-kHz sound wave. The obtained phase, whose units is radians, is converted to the line integral of the sound pressure, whose units is Pascal times meter, by multiplying $(\gamma p_0)/(k(n_0 - 1))$, where the value of p_0 and n_0 are shown in Table 4.2; $\gamma = 1.40$, $k = 2\pi/\lambda$, and $\lambda = 532 \times 10^{-9}$. Figure 4.7(c) shows the instantaneous image of the sound field obtained by the proposed method. The loudspeaker was located below the measured area. Because the wavelength of the sound wave is approximately 69 mm and the length of the horizontal axis is 30 mm, less than half the period of the sound wave appears in the image. Figure 4.7(d) shows the power of 5 kHz at each pixel. The distance decay of the sound field emitted by the loudspeaker is shown. The fixed pattern noise appeared in the power image, although it is unclear in the instantaneous image, as shown in Fig 4.7(c). This suggests that the fixed pattern noise appears as the multiplicative noise of the sound pressure. Figures. 4.7(e) and (f) show the waveform and power spectrum of the microphone and optical data, re-

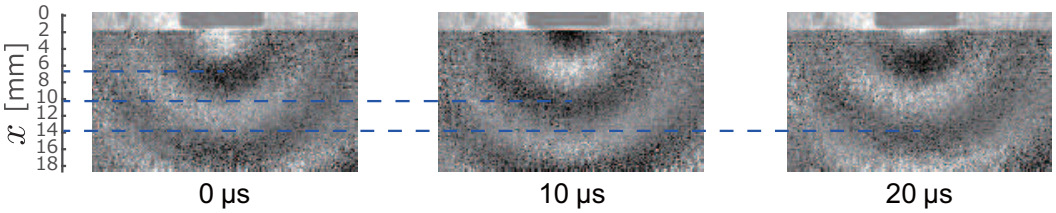

Figure 4.5: The phase images of the three obtained sequential frames.

spectively. As shown in the figures, the amplitude, phase and frequency of both data are agreed excellently. The difference in the power is 0.60 dB. Those results verified that the proposed method measured the quantitative value of the line integral of the sound pressure.

Subsequently, the input signal power was changed and measured by the proposed method and the microphone. The microphone was fixed at the center position of the positioning unit. The data of the proposed method was the averaged value of 10 pixels $\times$ 30 pixels. Figure 4.8 shows the relationship between the powers of the 5-kHz component of the proposed method and microphone. The least-mean-square line is calculated from the data above the noise level. The graph indicates that the lowest detectable range is approximately 90 dB SPL in the experimental condition. It is noteworthy that the noise level and PPSI values depend on the number of frames and their average, the conditions of the camera and light source, and the spatial characteristics of a sound source. In contrast, the maximum detectable sound pressure of the proposed method is limited by processing rather than the properties of the system. As sound pressure increases, the amount of the phase modulation increases. Because the power of the incident light is not changed, the detected value was not saturated owing to the increment in the acoustic power. Therefore, the optical system might be capable of measuring arbitrary large sound pressures. However, in such a situation, the theories described in Chapter 3 may not hold because the assumption of the geometrical optics cannot be applied. The other formulation is necessary for the measurement of large amplitude sound waves.

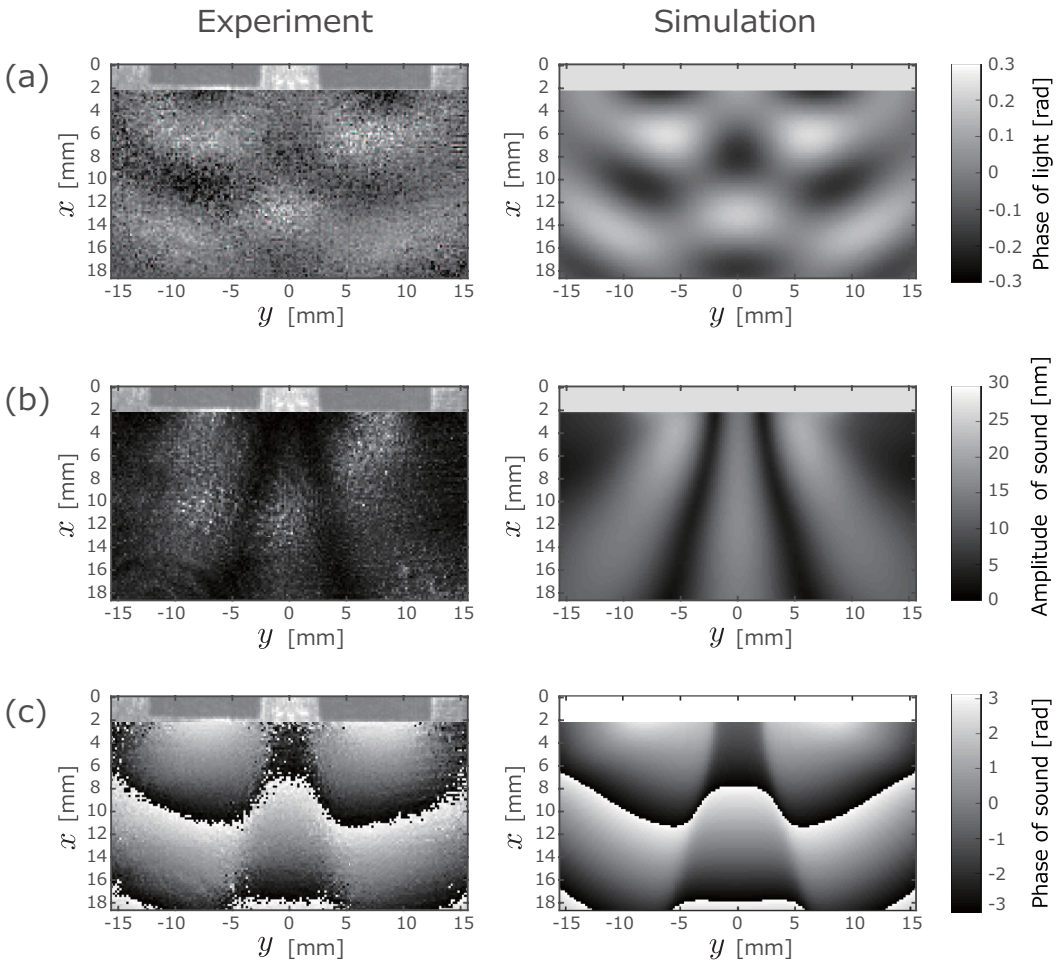

Figure 4.6: Imaging results of (a) the instantaneous phase, (b) the amplitude, and (c) the phase of the sound field generated by the two transducers driven by 40 kHz.

Table 4.2: Measurement conditions

PPSI	Framerate	50,000 fps
	Exposure time	1/50,000 s
	Image dimension	256 × 136
	Number of image	2,000
Sound	Loudspeaker	Fostex FT48D
	Waveform	Sinusoidal
	Amplitude	22.3 Pa
	Frequency	5,000 Hz
Microphone	Type	BK 4939
	Size	1/4 inch
	Dynamic range	28 - 164 dB
	Moving step	2 mm
	Moving range	300 mm
Environment	Static pressure	99,450 Pa
	Temperature	28.1 °C
	Relative humidity	41.0 %
	Static refractive index	1.000261

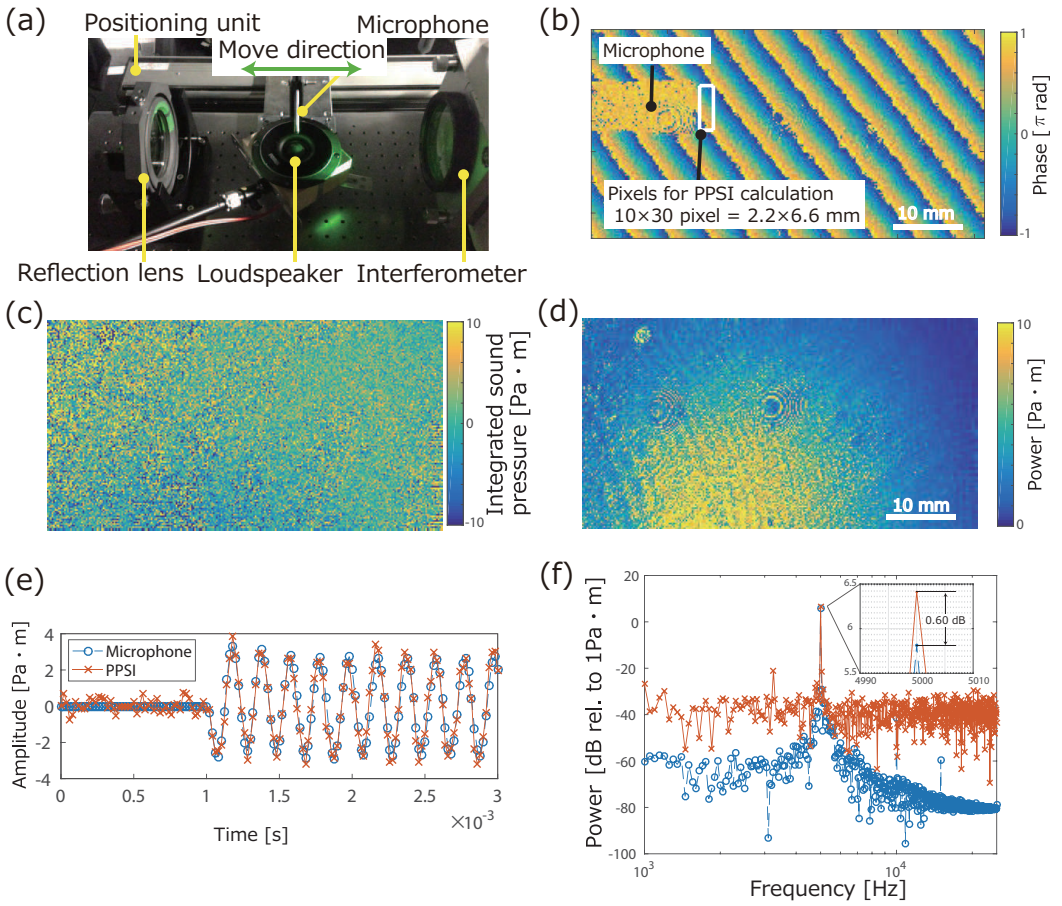

Figure 4.7: Experiment for the comparison of the proposed method and microphone measurements. (a) Photograph of the experimental instruments. The microphone, which was affixed on the linear positioning unit, was moved automatically along the direction indicated in the photograph. The microphone and loudspeaker were isolated from the optical table. (b) Image of the measured phase at a single frame before high-pass filtering. The slanting periodical discontinuity is due to the wrap of the phase. The shadow of the microphone is shown in the region where the discontinuity disappears. The white box near the microphone shadow indicates the pixels used for the optical data. (c) The instantaneous image of the sound field at a single frame after high-pass filtering. The loudspeaker was located below the measured area and the sound wave propagates from the bottom to the top of the image. (d) Image of the power of 5 kHz at each pixel of the data obtained by the proposed method. (e) Plots of the temporal waveform measured by the proposed method and microphone, and (f) that of the power spectrum. The optical data is the average of 10 pixels × 30 pixels within the white box in (b). The microphone data are the approximation of the integral by the 151 point measurement.

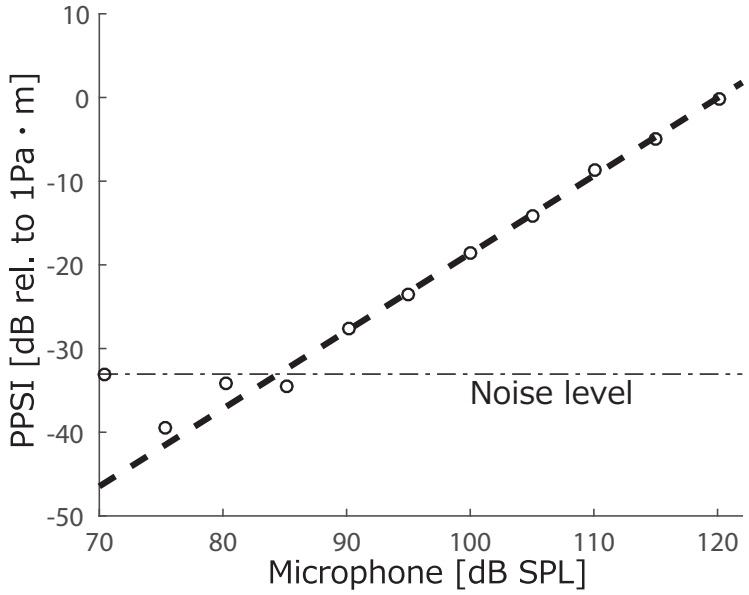

Figure 4.8: Relation between the measured values by the microphone and the proposed method. The circles are the measured data and the dashed line is the least-mean-square line. The dash-dotted line represents the noise level at the frequency of the signal.

Chapter 5

Imaging of sound generated by transducers

5.1 Loudspeakers

Evaluating the sound radiation from a loudspeaker is an important subject for improving sound quality in our daily lives. Generally, the measurement should be conducted in a special experimental room such as an anechoic chamber or a reverberation room. However, it is sometimes difficult to satisfy the requirement thereof; therefore, in such a case, accurate results are difficult to measure using microphones owing to the non-ideal characteristics of the measurement room. A strategy to overcome the severe requirement is to measure the very near field of transducers because the near-field contains less influence from the environments. Optical methods can achieve the measurement of the near field. Because the high-speed polarization interferometer can be used for a single-shot measurement, it can reduce the time for measurement compared with the scanning methods such as the LDV. This section describes the fundamental experiments for evaluating the feasibility of the transducer testing by the high-speed polarization interferometer.

A loudspeaker (DIATONE TW-G500) was mounted on a baffle plate of the radius of 15 cm. The speaker was driven by the sinusoidal signals of frequencies from 5 kHz to 20 kHz. The frame rate of the camera was 100,000 fps, and the exposure time was 10 μs. The size of the measurement area was a circle of diameter 100 mm. The time-directional band-pass filter, whose center frequency was identical to that of the signal and bandwidth of 200 Hz, was applied to each pixel of the measured data.

Figures 5.1 and 5.2 show the measurement results. The left column shows the instantaneous sound fields at a single frame, the center column is the power at the frequency of the signal, and the right column shows the phase at the frequency of the signal. The center of the loudspeaker was at the upper-left in the measurement circles, and a linear shadow at the upper-right in the circle was due to a reference microphone. The sound pressure level at the position of the microphone was approximately 110 dB. The sound waves radiated from the loudspeaker appear in all frequencies. The two-dimensional power and phase maps are obtained successfully

by the method including the very near field of the loudspeaker.

5.2 Ultrasonic transducer

Ultrasonic transducers are the key devices for many applications such as non-destructive testing, sonar, levitation, tactile sensors, and parametric speakers. Several types of electric-acoustic transducers have been developed for ultrasonic radiation in air. An important mission in ultrasonic transducer design is to improve the power of the radiated sound and radiation efficiency. In this regard, numerous designing methods such as [171] have been researched. The evaluation of the designed transducers is often conducted by calculating the sound radiation using, for example, finite element analysis, and by measuring sound pressure level and directivity using microphones. The near-field measurement of the transducers is difficult using a microphone because inserting a microphone near the transducer disturbs the sound field and also influences the radiation characteristics of the transducer. Thus, the optical observation of the sound field near an ultrasonic transducer can be contributed to a better evaluation of it.

The ultrasonic transducers whose resonance frequency of 40 kHz were measured and the near-field of those were analyzed. The frame rate of the camera was 7000 fps, and the exposure time was 1/101,000 s. The size of the measurement area was a circle of diameter 100 mm. The transducers were driven by a sinusoidal signal of 40 kHz. It is noteworthy that as the high-speed polarization interferometer does not contain an anti-alias filter, the measurement of a sinusoidal sound field whose frequency is higher than the frame rate of the camera is possible. When a sound field of 40 kHz is observed at 7000 fps, the signal appears at 2 kHz due to the aliasing. Thus, the band-pass filter of the center frequency of 2 kHz and bandwidth of 100 Hz was applied to each pixel of the recorded optical-phase video. The measurement results are shown in Fig. 5.3. The white painted parts represent the positions of the transducers and supports. The transducer in Fig. 5.3(a) contains a black tube around the cone, and that in Fig. 5.3(b) has no tube. The role of the tube is to improve the radiation power to the front direction of the transducer. The radiated sound waves can be seen in both images. The wavefront of Fig. 5.3(a) is almost spherical, and the radiation to the backward direction is small. Meanwhile, the wavefront of Fig. 5.3(b) is more complicated, and the backward radiation is shown in the image. The amplitude decreases at two angles. As the phase of sound in front of the cone and both sides of the cone differ, it can be estimated that the decreases in amplitude at the diagonal directions are caused by the superposition of the radiated sound to the front direction and those to the side directions. Thus, it is confirmed that the tube around cone operates as expected. A more detailed investigation can be conducted by changing the parameters of the cone such as the size, shape, and materials.

A metal plate of the thickness of 2 mm was set inside the measurement area, and the reflection and diffraction of the sound wave were observed. The measurement condition was the same as that of Fig. 5.3(a). The results are shown in Fig. 5.4. Characteristic patterns formed by the superposition of the incident and reflected

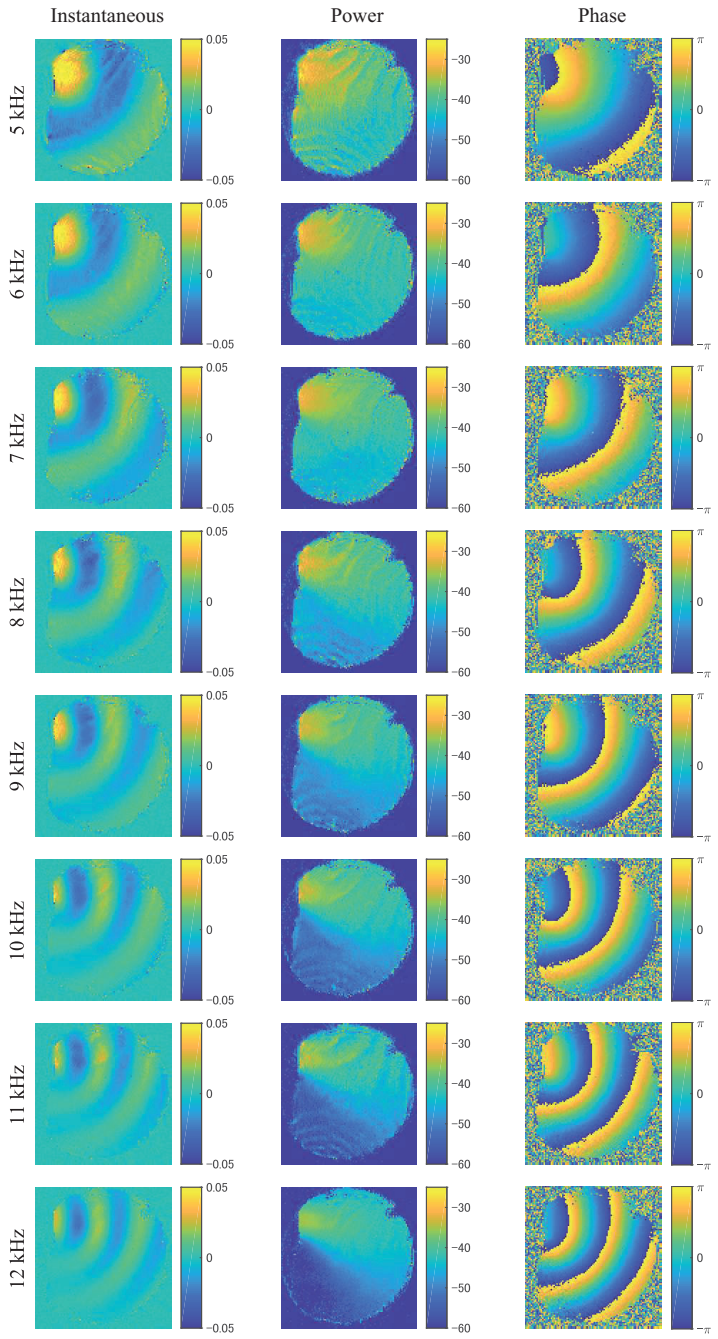

Figure 5.1: Visualization of the sound fields radiated from the baffled speaker (5 kHz to 12 kHz).

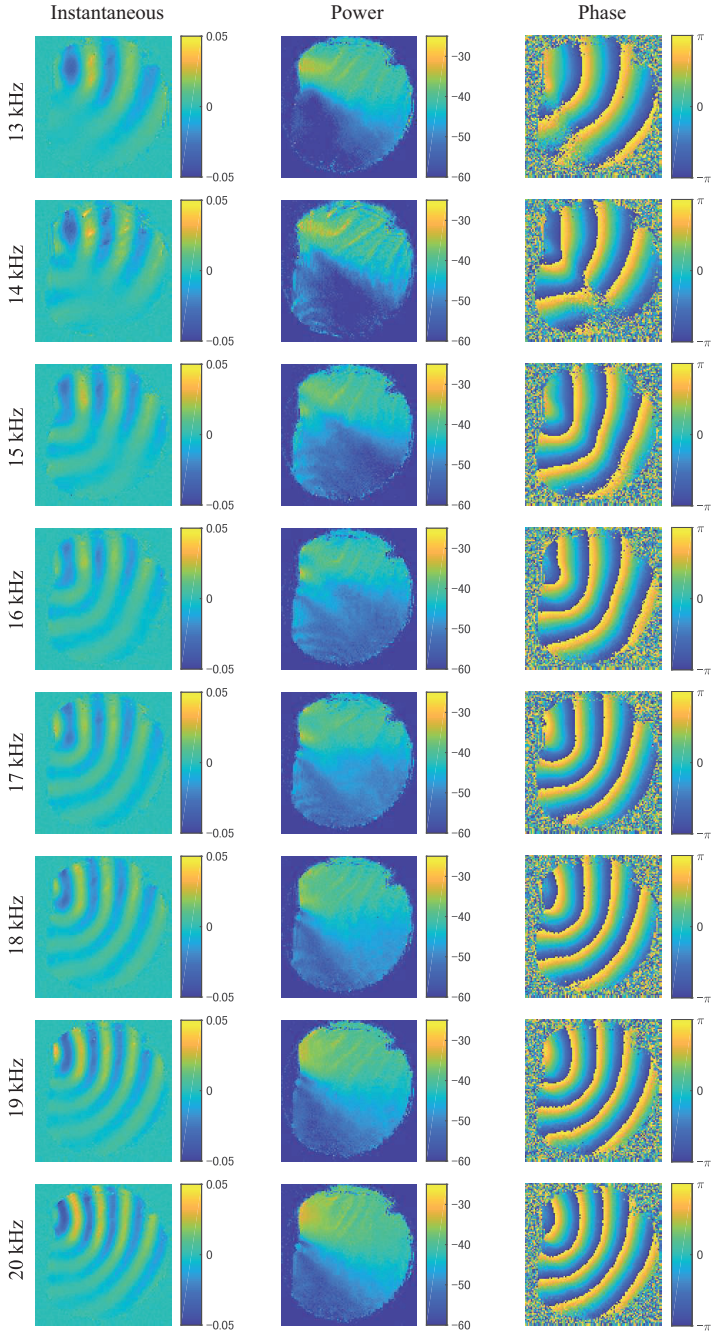

Figure 5.2: Visualization of the sound fields radiated from the baffled speaker (13 kHz to 20 kHz).

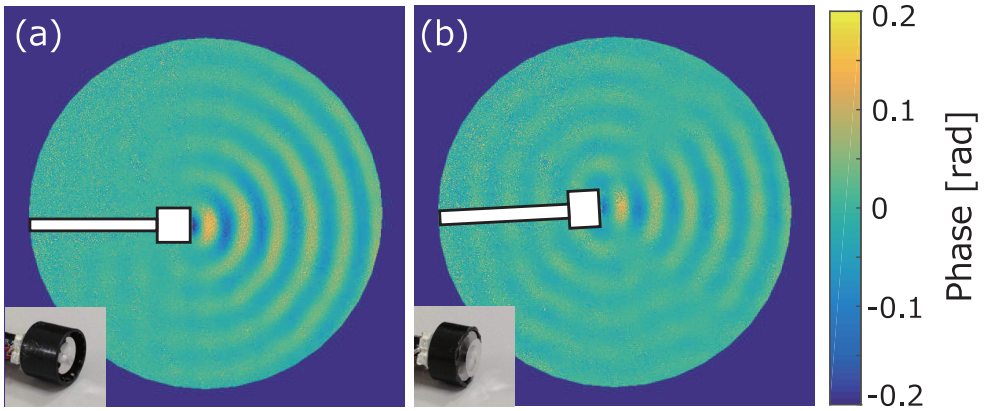

Figure 5.3: Measurement results of 40-kHz sound fields radiated by ultrasonic transducers.

sounds were observed. These measurement results agreed well with the phenomena that one can expect from fundamental principles in acoustics. Although these measurements are fundamental, it can be expected that this type of observation will be a useful tool for evaluating the performance of acoustic materials and noise barriers.

5.3 Imaging of sound field inside cavity

Many situations occur where a sound field inside a cavity or surrounded by objects is under investigation such as duct acoustics, a design of a cavity for a loudspeaker, acoustic resonance inside a body of musical instruments, and noise propagation inside a vehicle cabin. Measurements in those situations are typically conducted by inserting a microphone inside the cavity despite the undesired scattering caused by the microphone that contaminates the sound field. In addition, the microphone cannot well measure the sound pressure near the wall and in the narrow gap between the walls. To overcome such difficulties arising from the contact nature of a microphone, optical methods are a suitable alternative. The optical measurements of sound inside transparent cavities in the air have been achieved by ESPI [147] and LDV [96, 98, 101, 103, 114]. Because high-speed polarization interferometry utilizes the polarization of light that was not used in the previous methods, an appropriate material was examined and the feasibility of the imaging inside a transparent cavity was confirmed experimentally.

A necessary and sufficient condition for the measurement is that interference occurs. Because the high-speed polarization interferometer utilizes the polarization of light, the requirements for the materials of a cavity include high transparency, low birefringence, and low surface irregularity. In other words, the measurement can be performed even though the object is inserted within the measurement area if the following conditions are satisfied: an object is transparent; it has a smooth surface

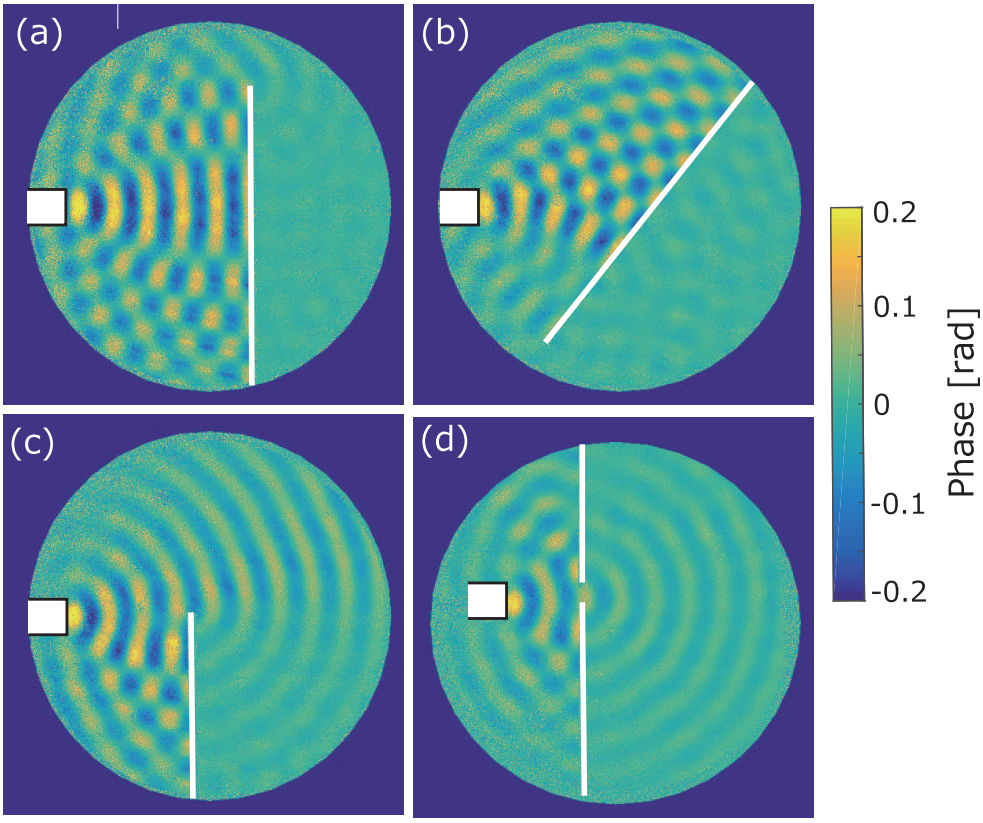

Figure 5.4: Visualization of the reflection and diffraction of the sound wave by a metal plate.

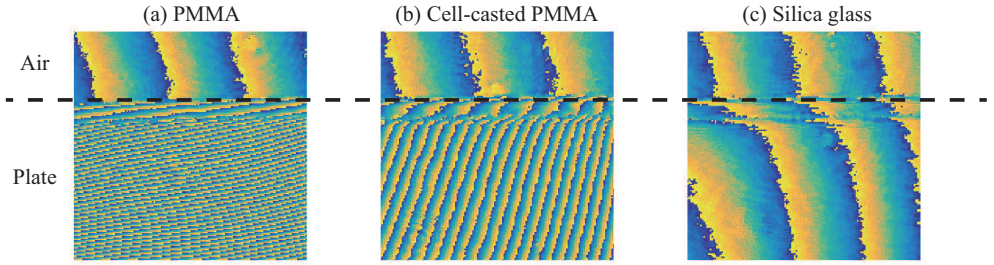

Figure 5.5: Visualization test of three transparent plates, (a) PMMA plates, (b) cell-casting PMMA plates, and (c) silica glass. The plates were inserted below the dashed black lines.

that does not disturb the wavefront; and it does not change the polarization state of transmitted light. Three transparent plates, namely, (a) an ordinary polymethyl methacrylate (PMMA) plate, (b) a cell-casted PMMA plate, and (c) a silica glass plate, were tested and the results are shown in Fig. 5.5. The black dashed lines indicate the air-plate interfaces. The fringes were formed in all plates. As the change in fringe patterns between the air and silica glass plate is the smallest, the silica glass demonstrates the best performance. The cell-casting PMMA plate performs better than the ordinary PPMA plate; this may be due to the low-birefringence nature of the cell-casting method. Although silica glass performs the best, the workability of the glass plate is not good, and the cost is the highest. Thus, for the following experiments, cell-casting PMMA plates were used.

Experiments were conducted to verify the feasibility of the imaging of a sound field inside a cavity. Rectangular ducts were created for the visualization of sound propagation inside the ducts. The schematics of the ducts are shown in the top of Fig. 5.6. Two transducers, whose resonance frequencies are approximately 40 kHz, were mounted on the top and bottom near the right edge of the ducts. The left side of the ducts was open such that sound can be propagated outward. The heights of the ducts correspond to the once and twice of the wavelength of the 40-kHz sound wave. Two measurements were conducted for each duct; the two transducers were driven by 40-kHz sinusoidal signals whose phase differences were 0° and 180°, respectively. The measurement parameters were as follows: the frame rate was 7000 fps, the exposure time was 1/101,000 s, and the pixel dimension was 352×260. The results are shown in the middle and bottom of Fig. 5.6. Specific patterns are formed inside the ducts and propagating spherical waves are observed outside the ducts. Noisy pixels appeared near both sides of the ducts. They were caused by glues adhering during the assembling process. The patterns inside the ducts depend on the phase difference of the transducers. When the transducers were driven by in-phase signals, the center horizontal line of the ducts became an anti-node of the sound pressure; meanwhile, when the transducers were driven by anti-phase signals, the center horizontal line became a node. As shown from the

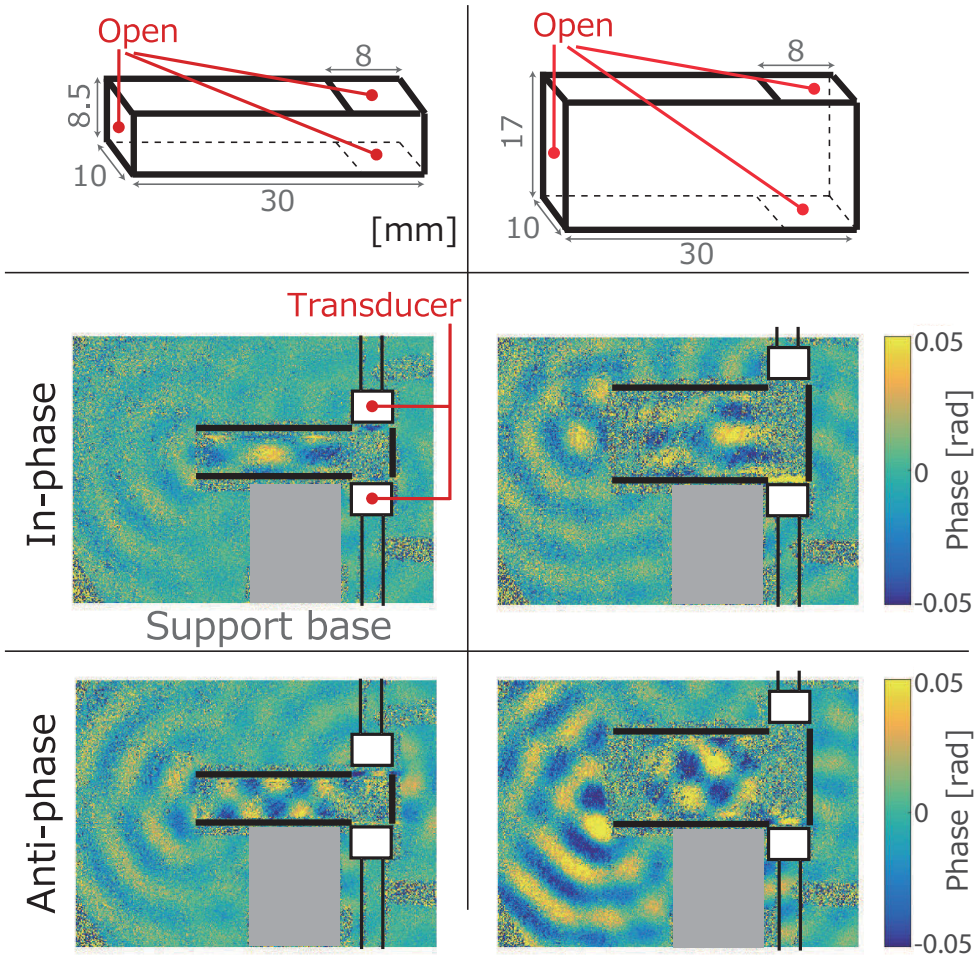

Figure 5.6: Results of imaging of the sound fields inside the rectangular ducts.

results at the left sides of Fig. 5.6, the radiated sound wave of the in-phase condition exhibits a monopole-like wavefront, and that of the anti-phase condition exhibits a dipole-like wavefront because the sound pressure at the upper and lower sides of the duct have opposite phase. For the duct on the right-hand side, the radiated sound fields are more complicated. This is attributed to errors imposed during the assembling and configuration processes. From the results shown in the figure, it is confirmed that the proposed method can visualize sound fields inside the cavities.

To investigate the proposed method using a more complicated example, a ported speaker box was created using the PMMA plates and a full-range speaker unit was mounted. The photograph of the speaker is shown in Fig. 5.7(a). A full-range speaker unit of the diameter 40 mm was mounted, and the port of height 10 mm was arranged. The dimension of the cavity was designed based on the size of the measurement area of the high-speed polarization camera. The power spectrum measured by a quarter-inch microphone is plotted in Fig. 5.7(b). The microphone

was arranged at 20 mm from the speaker unit and port. Several peaks and dips appear at the spectrum measured at the front of the port. Sinusoidal waves of frequencies ranging from 1 kHz to 20 kHz with 1 kHz steps were used for the input signals. The measurement parameters were as follows: the frame rate was 7000 fps, the exposure time was 1/40,000 s, and the pixel dimension was 512 $\times$ 512. At the frame rate of 7000 fps, the 7-kHz and 14-kHz sound fields were difficult to measure because the sound fields were in the same phase at every frame. Thus, those frequencies were not included in the results. A band-pass filter of bandwidth 100 Hz was applied to each pixel of the videos.

Figures 5.8, 5.9, and 5.10 show the measurement results for 1 kHz to 6 kHz, 8 kHz to 13 kHz, and 15 kHz to 20 kHz, respectively. The instantaneous sound field, power, and phase maps at the signal frequency are shown in each frequency. Note that the color ranges of the instantaneous fields and the power maps of the images were adjusted separately to increase the visibilities of the results. The color ranges of the phase map is $-\pi$ to π. As the frequency of sound increases, the spatial patterns of the fields becomes complicated. At 1 kHz, the signs of the sound inside and outside of the speaker are opposite, and the value is zero near the exit of the port. The spherical sound wave radiated from the speaker unit is observed in the 2-kHz image. The sign of the sound at the back of the speaker diaphragm is opposite of that at the front of the diaphragm. The sound field at 3 kHz contains the sound-pressure node at the center inside the speaker. Consequently, the radiated sound from the speaker unit and duct interfered destructively. The node of the radiated sound pressure becomes clearer in the 4 kHz field, even though the node in the speaker box is unclear. The wavefronts of the radiated waves of the frequencies between 5 kHz to 11 kHz are almost spherical, whereas those of frequencies higher than 12 kHz become planer gradually. The power maps indicate that the radiated power concentrates near the acoustic axis of the speaker unit for the higher frequencies, although the acoustic modes in the box became more complicated. These results suggest that the acoustic modes in the box are less important for the radiated sound waves when the frequency of the sound is higher than a certain value determined by the box geometry. In other words, a critical frequency band appears where the interior acoustic resonance largely affects the radiated sound field, and the proposed visualization method will be a powerful tool for investigating the effect and design of a speaker box system that exhibits the desired radiated sound field pattern.

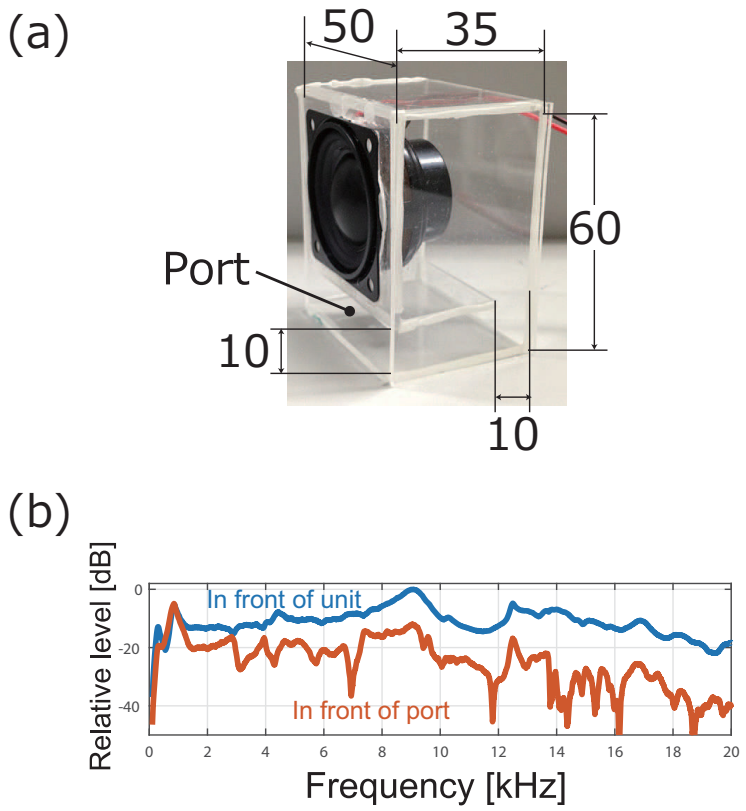

Figure 5.7: (a) Photograph of the ported speaker. (b) Power spectrum measured by a microphone.

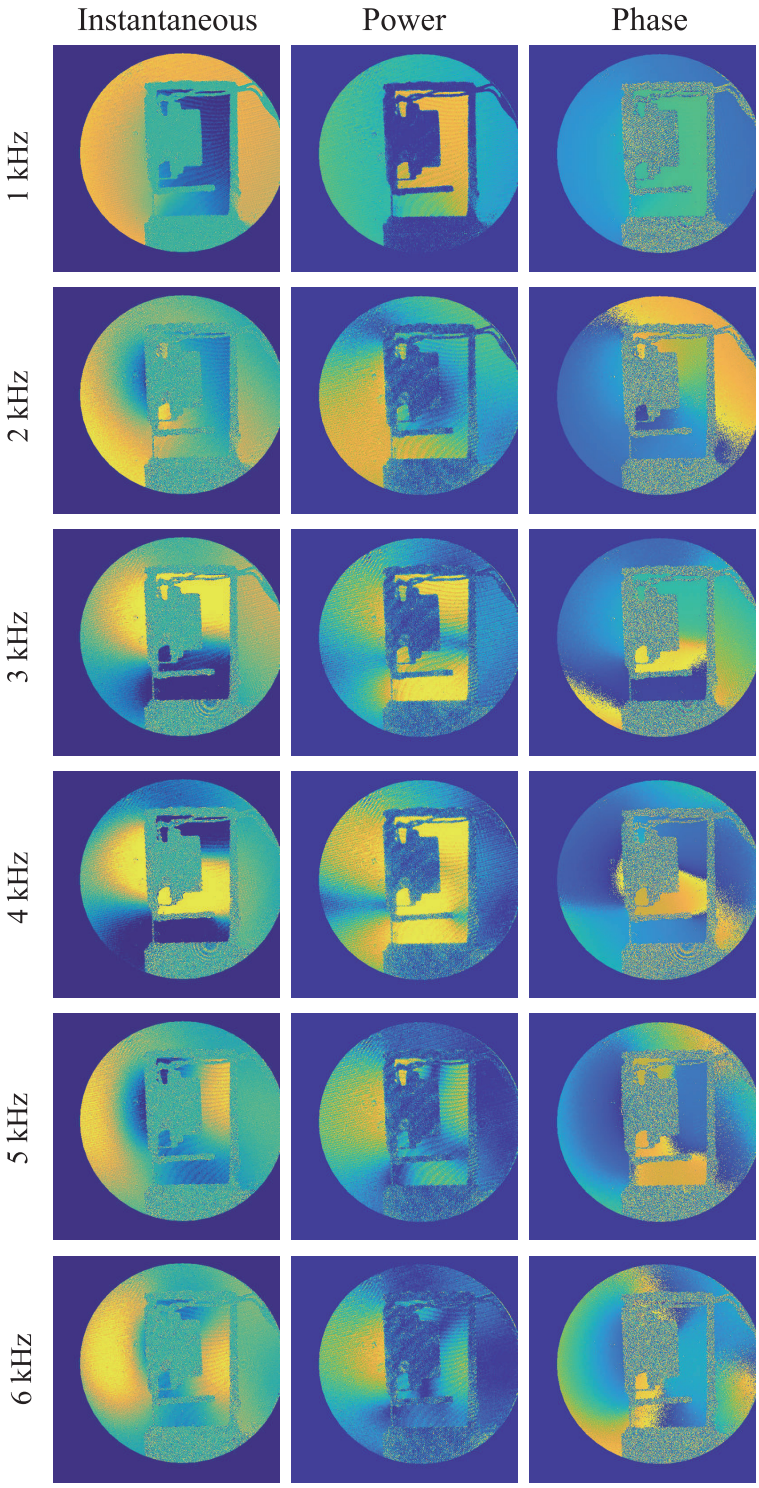

Figure 5.8: Visualization of the sound fields inside the ported speaker (1 kHz to 6 kHz).

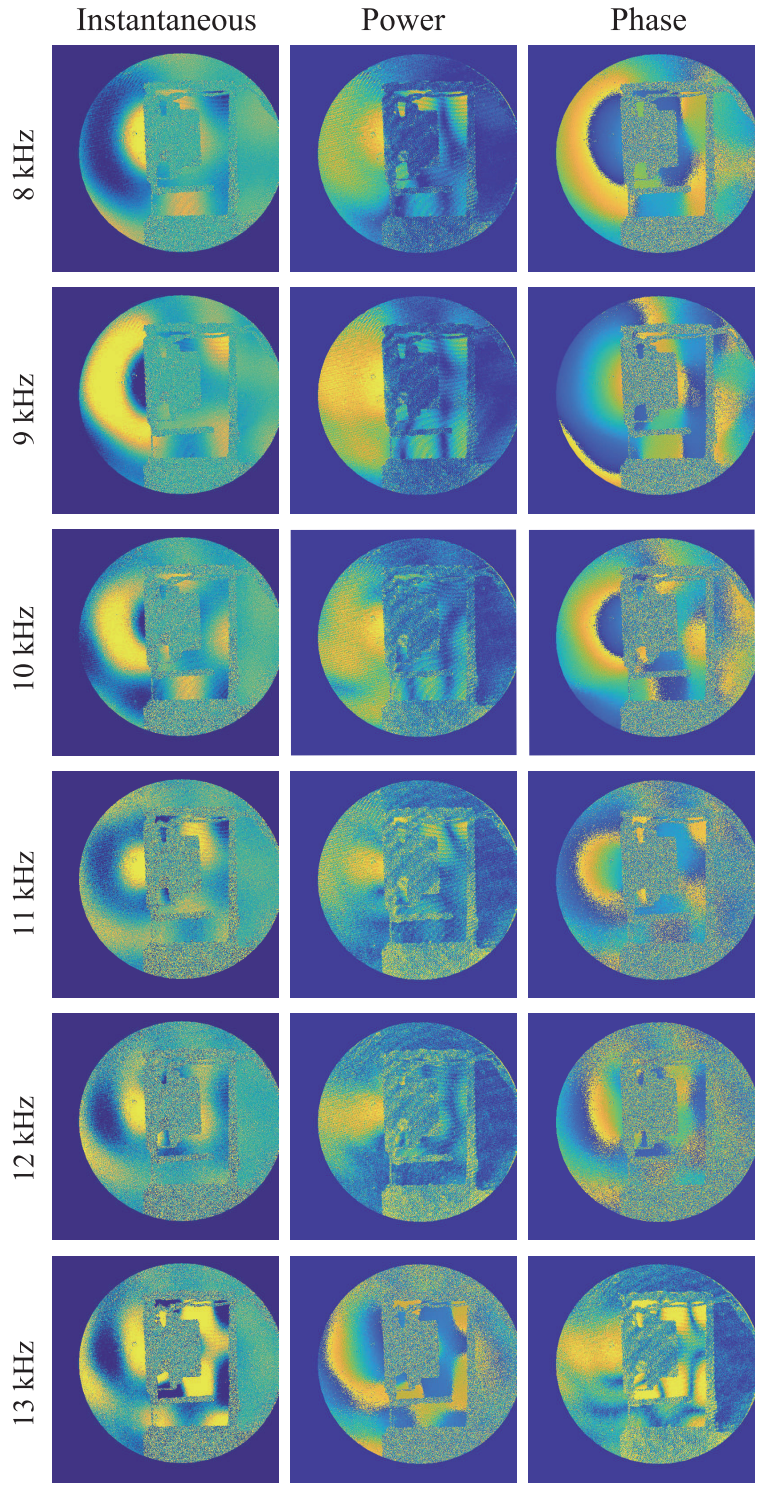

Figure 5.9: Visualization of the sound fields inside the ported speaker (8 kHz to 13 kHz).

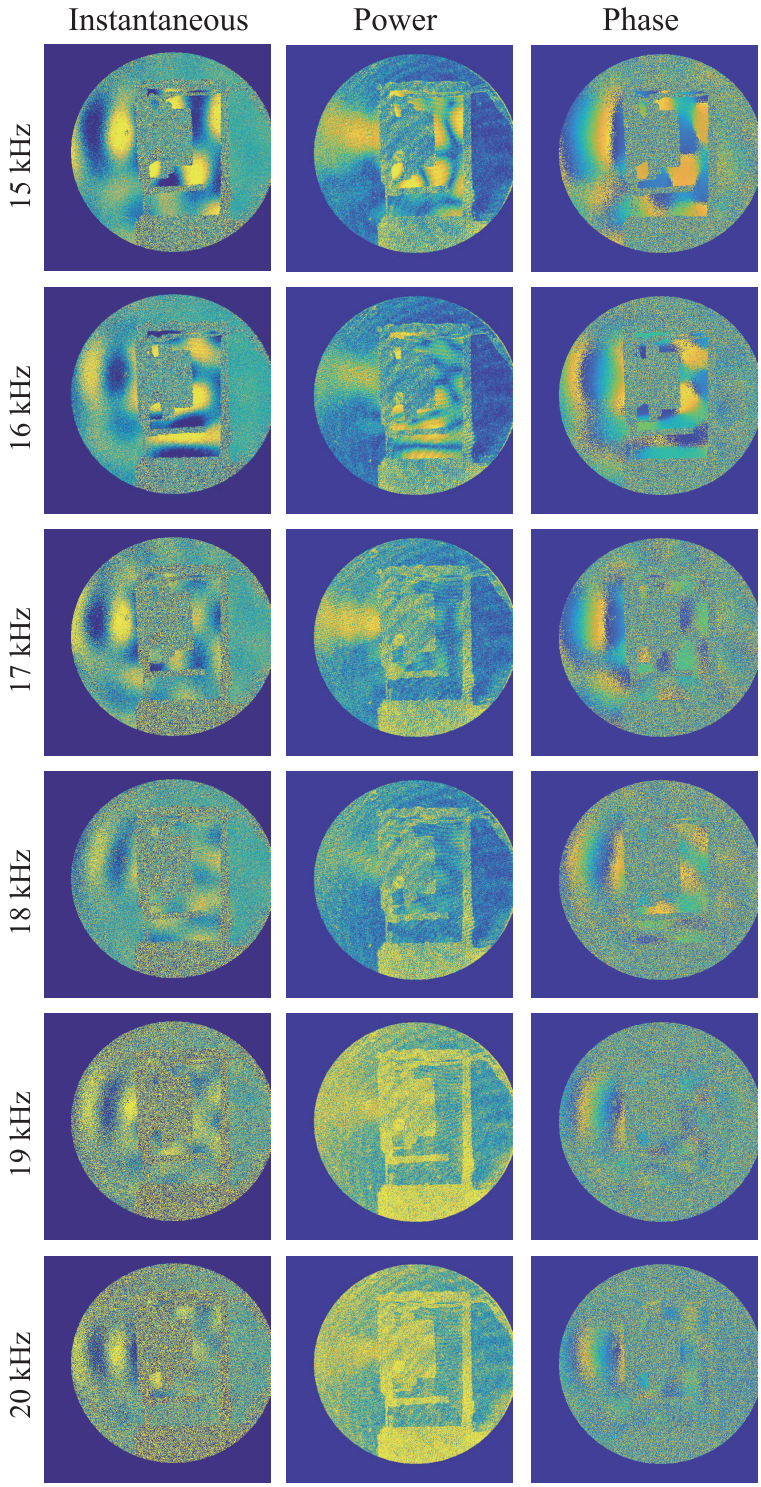

Figure 5.10: Visualization of the sound fields inside the ported speaker (15 kHz to 20 kHz).

Chapter 6

Imaging of sound radiation from castanets

6.1 Sound measurement in musical acoustics

Musical acoustics is a branch of acoustics concerning the science of music including musical instruments. Musical instruments have been influenced by cultural and technological contexts worldwide, and these structures and principles differ widely. Many musical instruments exist whose principles are still not disclosed hitherto. The understanding of the physical mechanism underlying sound radiation from musical instruments is important for their design and fabrication; and thus, it has been studied actively. The measurement of sound from the musical instruments is typically performed using a microphone or microphone array, and acoustic properties such as sound pressure, frequency spectrum, and radiation directivity are often obtained. Although information regarding the spatio-temporal evolution of sound field aids the understanding of the phenomenon, obtaining such information by using microphones is difficult.

Several studies used the OMS for research on musical instruments. A scanning LDV was applied to the measurement of vibration modes and radiated sound fields from a violin [105, 106]. As the measurable sound field by the scanning LDV was limited to reproducible fields, the violin was performed by a mechanically driven bow. The Schlieren method was used to visualize shock waves radiating from a trombone [59] and trumpet [60, 61]. Hitherto, it is difficult to assert that the OMS has been used effectively in musical acoustics.

This chapter describes the measurement of sound radiation from castanets and demonstrates the effectiveness of the high-speed polarization interferometry for investigating musical instruments. By analyzing the imaging results, the radiation mechanisms of three frequency bands consisting of the castanets' sound were identified.

6.2 Background of castanets

Castanets are a percussive instrument consisting a pair of shallow shells, where two shells are tied by a cord through holes near an edge. The castanets are important cultural instruments, especially in Spain.

Although they are common and has a simple structure, the physics of the castanets has not yet been disclosed. One can easily expect that the sound from the castanets is attributed to the geometry, mechanical properties, and forces acting on the shells. However, the physical process is not trivial because of the nonlinearity of their deformation. In addition, the shells are not thin enough such that thin thickness approximations can be applied. Consequently, a physical model of the shells becomes much complicated compared to other thin percussive instruments consisting of membranes and plates. Thus far, the radiation of sound from castanets has not been described scientifically. This section discusses the acoustics of the castanets based on the experimental observations using the high-speed polarization interferometer and microphones.

6.3 Experimental Setup

To investigate the sound radiation characteristics of castanets, measurements using the high-speed polarization interferometer and microphones were conducted. Figure 6.1 shows the photograph of the five castanets used for the experiments. Their sizes and shapes were different, and three types of materials were used: ebony, rosewood, and fiberglass. The castanets were played by the author, who has no experience in playing castanets.

A quarter inch microphone (GRAS 46BE) was used to measure the sound produced at a distance. The imaging of sound fields around the castanets was conducted by using the high-speed polarization interferometer. The frame rate of the camera was 100,000 fps, and the exposure time was 10 μs. The size of the measurement area was the circle of 100 mm diameter. For synchronizing both instruments, the output signal from the microphone was monitored and a reference trigger was sent to the high-speed camera.

6.4 Results

6.4.1 Microphone measurement

Figures 6.2 to 6.6 show the plots of the waveforms, power spectrum, and spectrograms of each castanet obtained from the microphone. The waveforms and power spectrum show the data obtained from the repeated five measurements, and a typical one was used to calculate the spectrogram for each castanets. The common characteristics among the castanets can be observed. The temporal waveforms are dumped oscillations, as expected. At least two peaks were observed in the power spectrums and spectrograms. The frequencies of the peaks and their ratios are listed in Table 6.1. The frequency ratio of the first and second peaks are neither a

Figure 6.1: Photograph of five castanets used for the experiments. From left to right: (A) Playwood CA-12 M made from ebony, (B) Playwood CA-13PRO made from ebony, (C) Playwood CA-23 made from rosewood, (D) Jale Pollpas made from fiberglass, and (E) Firigrana Bolero made from fiberglass.

constant nor an integer. The causes of those peaks were investigated using optical measurements.

As shown in the spectrograms, the frequencies of the first peaks increased with time during the first 5 ms after impact. To emphasize this effect, a band-pass filter that passes the frequencies between 1000 Hz to 2000 Hz was applied to the microphone signals, and the original and filtered waveforms of castanets A are plotted in Fig. 6.7. The intervals of the peaks were calculated by obtaining peaks of the filtered waveforms; those of the five castanets are plotted in Fig. 6.8. The common trend of increasing the intervals with time is captured. The start and end frequencies, and the slopes depend on the castanets. This is attributable to the nonlinearity of the system or the time-varying nature of the system.

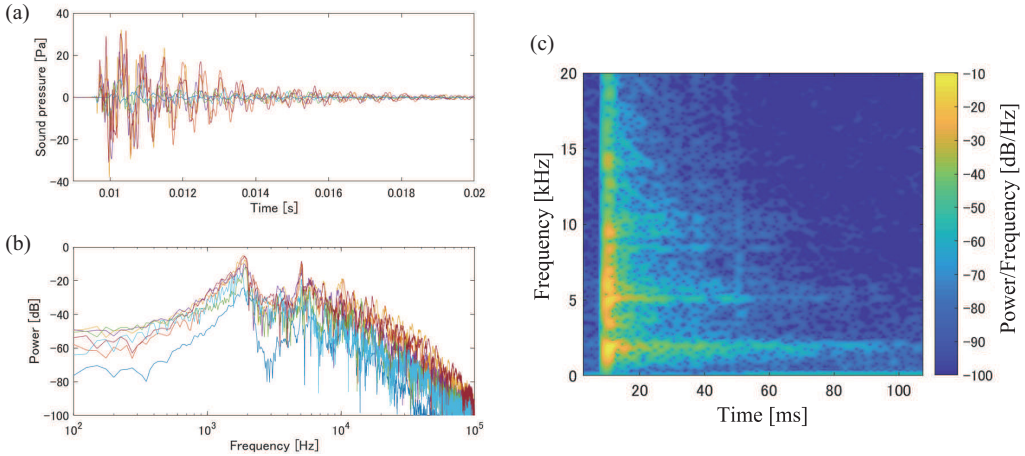

Figure 6.2: Waveforms, power spectrum, and a spectrogram of the castanets A (Playwood CA-12 M made from ebony) measured by the microphone.

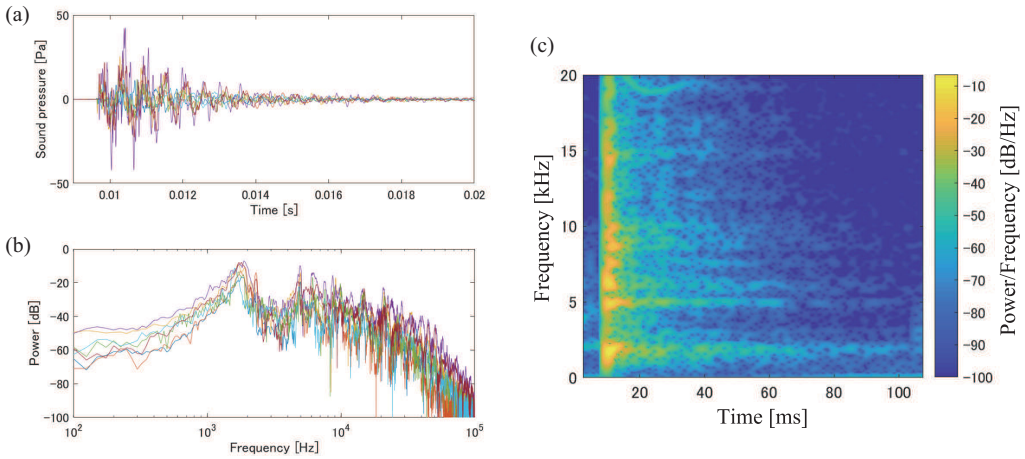

Figure 6.3: Waveforms, power spectrum, and a spectrogram of the castanets B (Playwood CA-13PRO made from ebony) measured by the microphone.

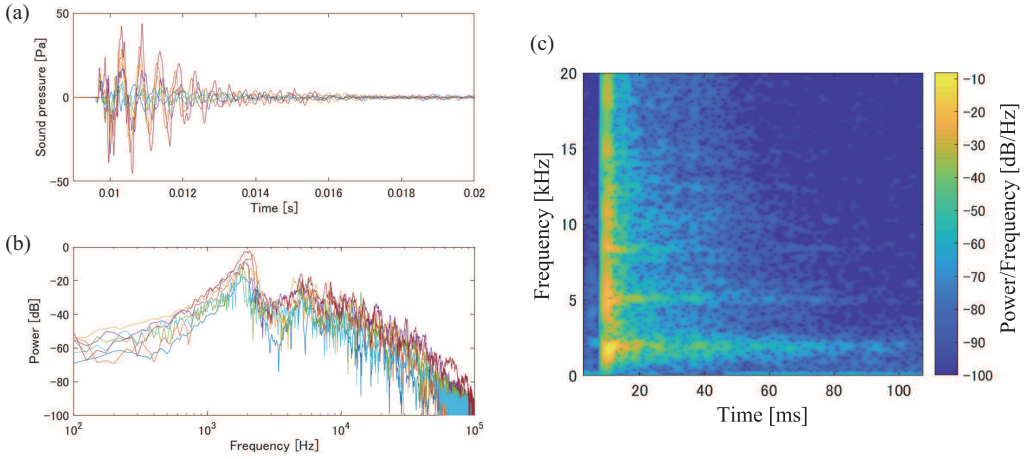

Figure 6.4: Waveforms, power spectrum, and a spectrogram of the castanets C (Playwood CA-23 made from rosewood) measured by the microphone.

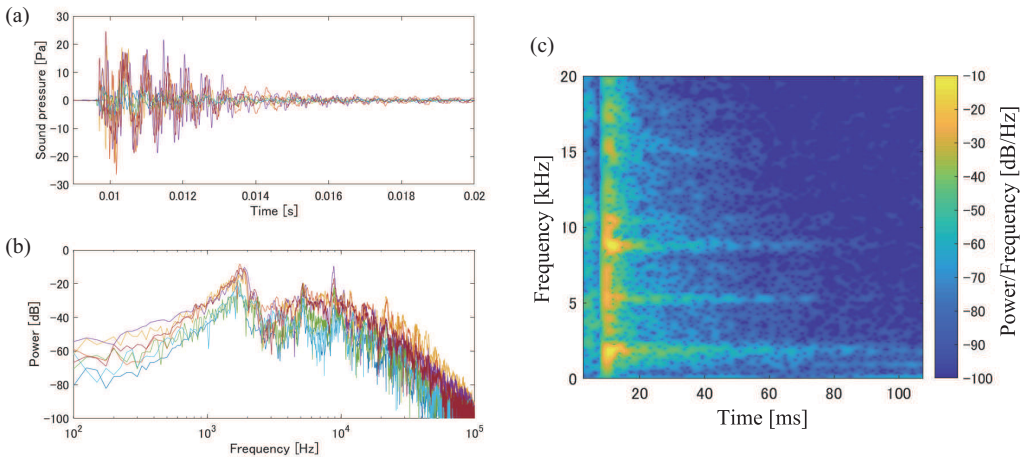

Figure 6.5: Waveforms, power spectrum, and a spectrogram of the castanets D (Jale Pollpas made from fiberglass) measured by the microphone.

Table 6.1: Frequencies of the peaks of the five castanets

	A	B	C	D	E
First peak [Hz]	1900	1800	2000	1775	1650
Second peak [Hz]	5100	5000	5100	5200	4200
Ratio	2.68	2.78	2.55	2.93	2.55

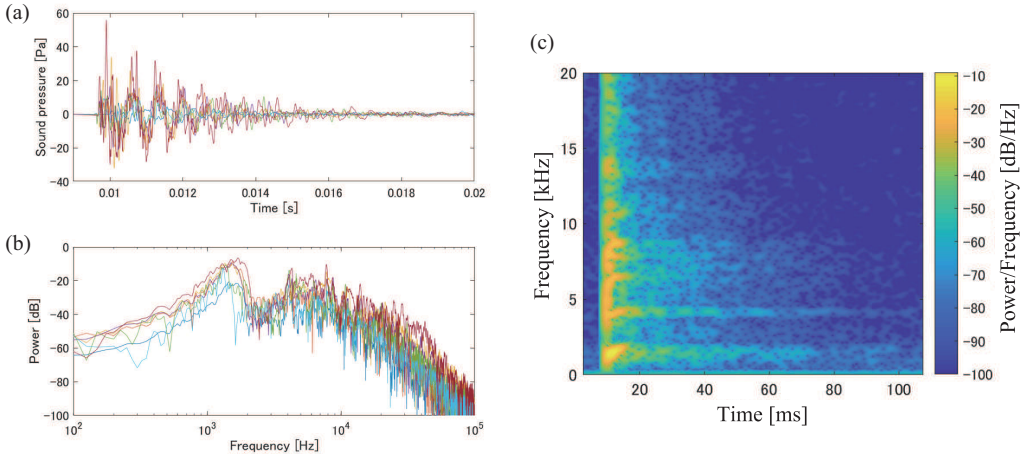

Figure 6.6: Waveforms, power spectrum, and a spectrogram of the castanets E (Firigrana Bolero made from fiberglass) measured by the microphone.

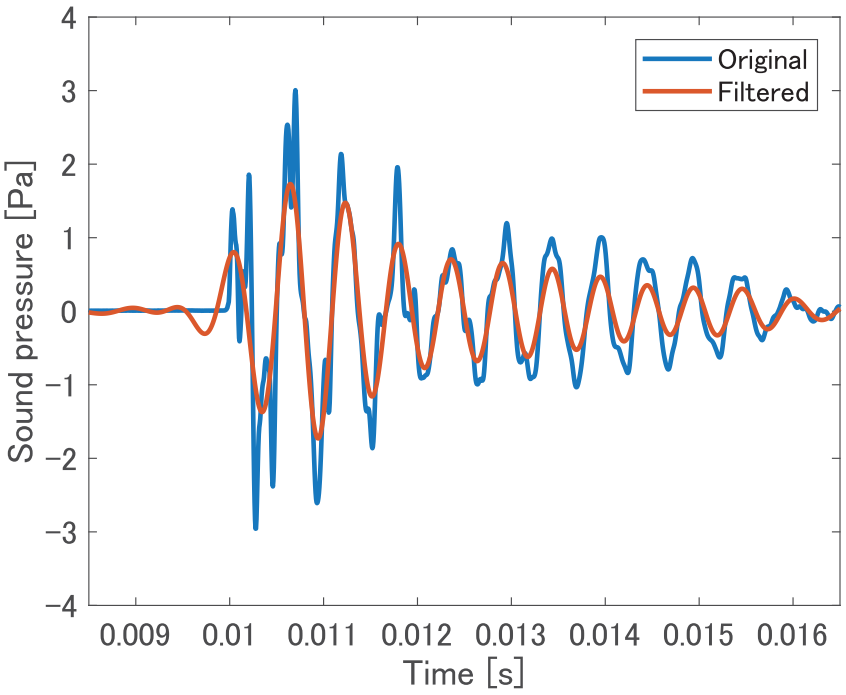

Figure 6.7: Original waveform and the filtered waveform to extract the first mode of the castanets A.

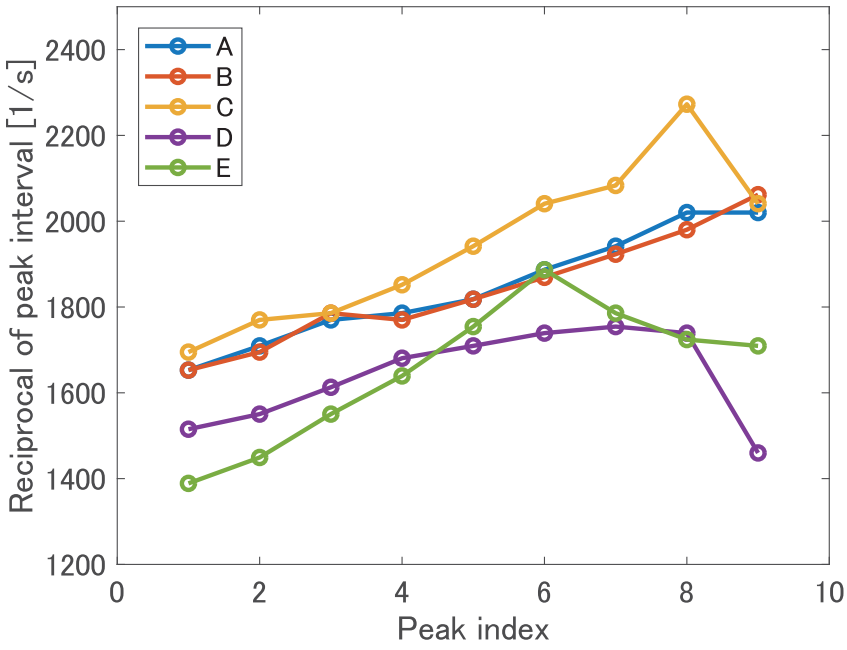

Figure 6.8: Change in the intervals of successive peaks of the first modes. The intervals are calculated by obtaining the peaks from the filtered waveforms.

6.4.2 Optical measurement

The sound radiations from the castanets B and E were measured by using the high-speed polarization interferometry. Figures 6.9 and 6.10 show the sound fields at the moment of the impact of the castanets B and E, respectively. At the center of each image, the shadows of the castanets and player finger are shown. The tips of the castanets are on the left. Because slowly varying components such as the environmental vibration significantly decrease the visibility of the sound fields, processing to eliminate such components is necessary. In this study, to maintain the instantaneous behavior of the sound fields at the moment of impacts, the temporal differences between two successive frames that operate as a high-pass filter, are shown. The initial sound waves are clearly captured, i.e., those occurring near the tips and propagates to the tails. The initial change in the pressure is negative, and a positive pressure appears at the leading part of the initial wave after 40 μs. The initial sound radiation occurs in an almost symmetric manner against the two shells. The general features of the initial sound radiation are typical in the castanets B and E. By focusing on the differences between the castanets B and E, it can be observed that the initial sound field of castanets B contains wavefronts of different propagation directions, while that of the castanets E contains wavefronts of the same propagation direction and spatial width. Consequently, the initial pressure wave from the castanets E is more radiative than that of the castanets B. Interestingly, not only the radiated sound wave but also the sound between the shells are captured. This is due to the non-intrusiveness and single-shot nature of the high-speed polarization interferometer. Particularly, at the beginning of castanets E, a positive pressure appeared between the shells near the tip and it moves slower than the surface waves. Note that, the sound field between the shells of the castanets B was not clearly captured due to the edge diffraction of the probing light.

To investigate the sound fields generated by each frequency band, three filters were applied to the measurement results: a band-pass filter that passes the first mode, a band-pass filter that passes the second mode, and a high-pass filter that passes frequencies above 6 kHz. The filtered images using the band-pass filter extracting the first mode are shown in Figs. 6.11 and 6.12. As the wavelength of the sound in the frequency range is longer than the diameter of the measurement area, the radiated sound around the castanets appear to be blinking. By representing the results as a movie, however, the sound wave propagating outward from the castanets can be observed. The images of the amplitude and phase at the frequency of each first mode are shown in Figs. 6.13 and 6.14. The amplitude of the sound between the shells is higher than that of the radiated sound, and their phases are different. As can be expected from the instantaneous images, the radiation due to the first modes is independent of direction; the first modes have monopole-like directivity and those origins coincide with the center of the castanets. The temporal variations at the points between the shells and outside the shells were extracted from the filtered images and are plotted in Figs. 6.15 and 6.16. The damped oscillations at the frequency of each first mode are observed. The amplitudes at the points inside

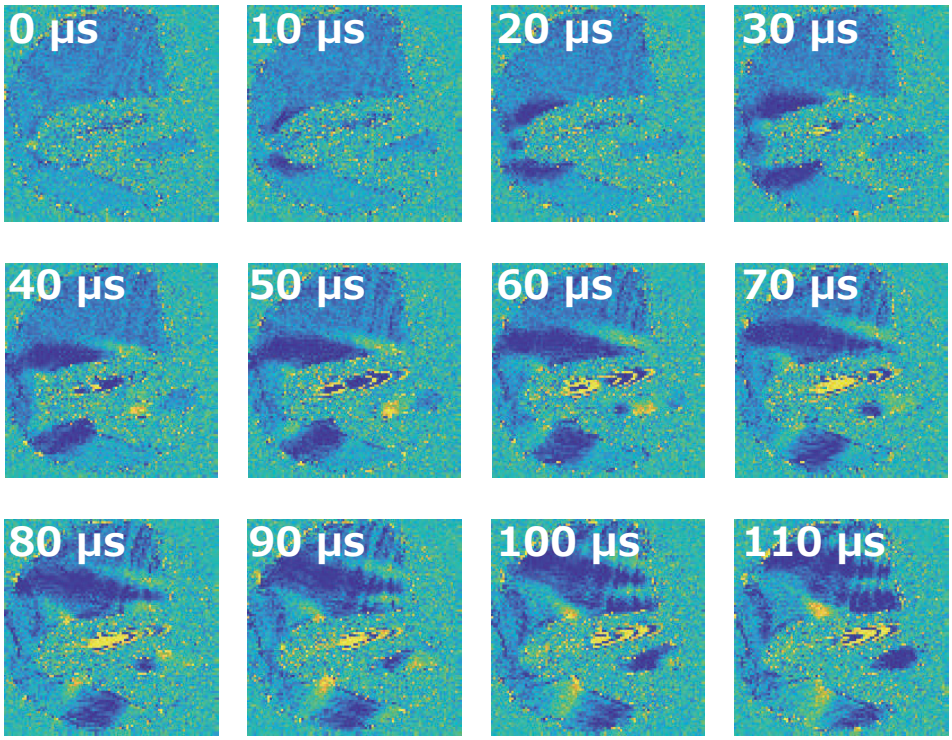

Figure 6.9: Sound fields at the moment of the impact of the castanets B. The images are the temporal differences between the two successive frames. The intervals between each image is 10 μs.

the shells are approximately 10 times larger than those outside the shells. The phase of both waves differs by approximately 90°. These features are similar to the resonance of the damped system. Considering that the castanets have a small cavity between the shells and a slight gap (generally several millimeters) connects the inner cavity and the exterior, the first mode of the castanets would be modeled by the Helmholtz resonance.

The band-pass filters extracting second peaks were applied to the measured data. The center frequencies of the filters for castanets B and E were 5000 Hz and 4200 Hz, respectively. The examples of the filtered images are shown in Figs. 6.17 and 6.18. The interval of the images is 40 μs. The sound is radiated from the tips of the castanets and spreads spherically. The acoustic resonances are observed between the shells. A node appears at the center of the shells, and the periods of the inner acoustic resonance are identical to those of the radiated sound. The amplitude and phase maps at the peak frequencies are shown in Figs. 6.19 and 6.20. The radiated sound is large at the tips of the castanets. According to the phase maps, the acoustic center of the second mode is at the tip of the castanets. From the amplitude maps, it is shown that the amplitudes between the shells are larger than those of the radiated sound except for the nodes. The phase of sound between the shells becomes opposite by the node. Their results clearly indicate that the second mode is owing to the acoustic resonance such that the wavelength of sound and the length of the shells

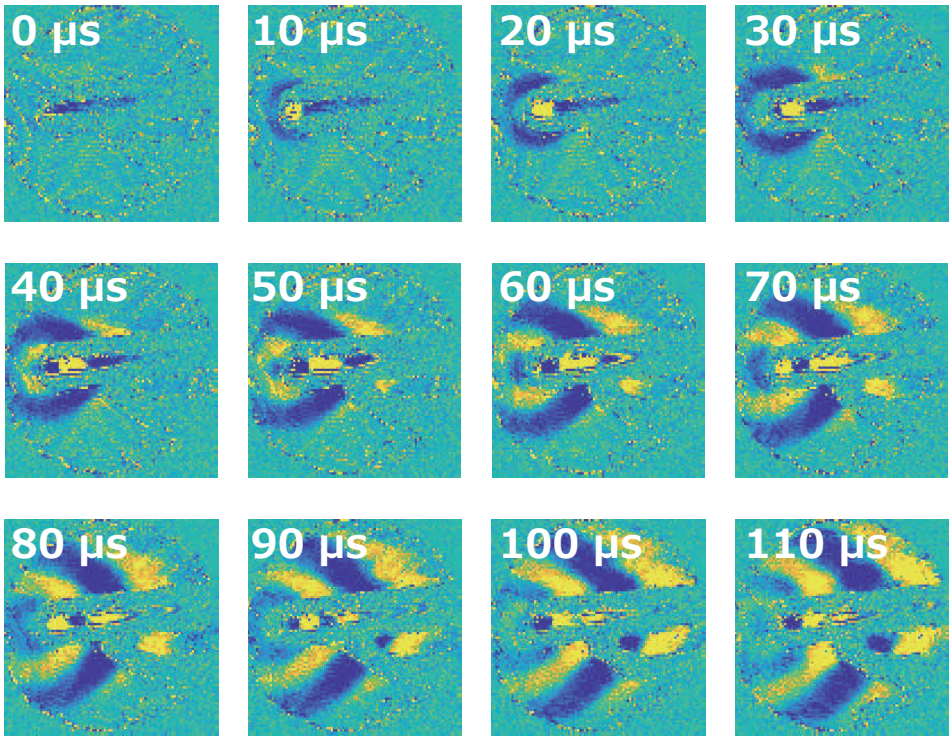

Figure 6.10: Sound fields at the moment of the impact of the castanets E. The images are the temporal differences between the two successive frames. The intervals between each image is 10 μs.

coincide. Table 6.2 lists the length of the shells, calculated resonance frequencies, and the measured frequencies of the second modes. The calculated frequencies were the frequencies of sound whose wavelengths are identical to the length of the shells and the speed of sound was 343 m/s. Although the calculated values are lower than the measured values, the values would be reasonable. A detailed model for calculating the frequency of the second mode should be considered for future work.

To observe higher frequencies than those of the second mode, the high-pass filter that eliminates frequencies of less than 6000 Hz was applied. The results are shown in Figs. 6.21 and 6.22. The instantaneous fields are more complicated than those generated by the first and second modes. The radiating sound fields are the superposition of many frequency components exhibiting different propagation speeds and spatial profiles. Although no large peak appears in the frequency spectrum, some

Table 6.2: Calculated frequencies of the one wavelength duct modes and measured frequencies of the five castanets.

	A	B	C	D	E
Length of shells [mm]	75	73	75	72	85
Calculated frequency [Hz]	4570	4700	4570	4760	4040
Measured frequency [Hz]	5100	5000	5100	5200	4200

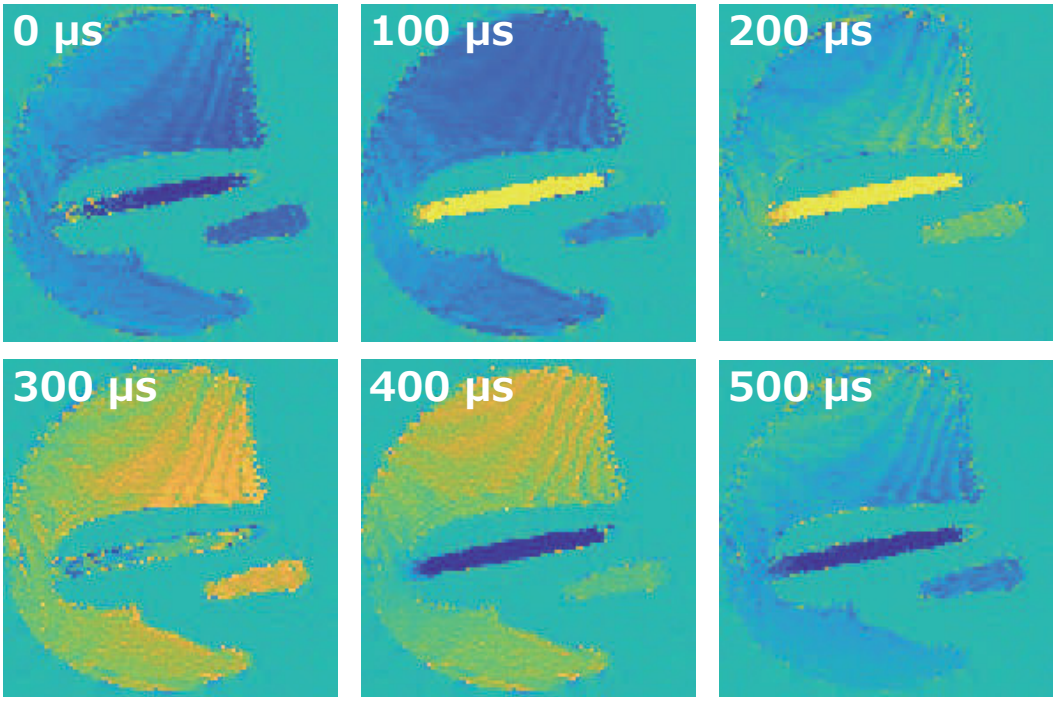

Figure 6.11: Filtered images by using the band-pass filter extracting the first mode of the castanets B. The intervals between each image is 100 μs.

characteristic frequencies exist. The sound fields of four representative frequencies are shown in Figs. 6.21(b) and 6.22(b). The spatial profiles of the amplitudes and phases differ widely with frequency. At 10 kHz of castanets B, a strong radiation of sound to an oblique angle occured. This type of radiation is caused by flexural waves on the surface of the shells. The radiation from castanets B at 21 kHz and that from castanets E at 18 kHz exhibit the complicated phase maps. These appear to be chains of multiple spherical wavefronts. This would be caused by complex vibration profiles on the shell surfaces, rather than the acoustic resonance of the cavity. It can be assumed that the sound radiation from frequencies higher than the second mode is caused by the multiple sources, including the flexural wave on the surface of the shells and vibration mode of the shells, both of which depends on the frequency of sound, geometry and material of shells, and the method of playing the castanets.

6.5 Conclusions

The mechanism of sound radiation from castanets was investigated using a microphone and a high-speed polarization interferometer. According to the single-shot and non-intrusive nature of the high-speed polarization interferometry, the sound fields around the instruments performed by a human were visualized successfully. It was found that the sound radiation from the castanets consisted of three frequency components: (i) omnidirectional sound radiation around 2 kHz that should be mod-

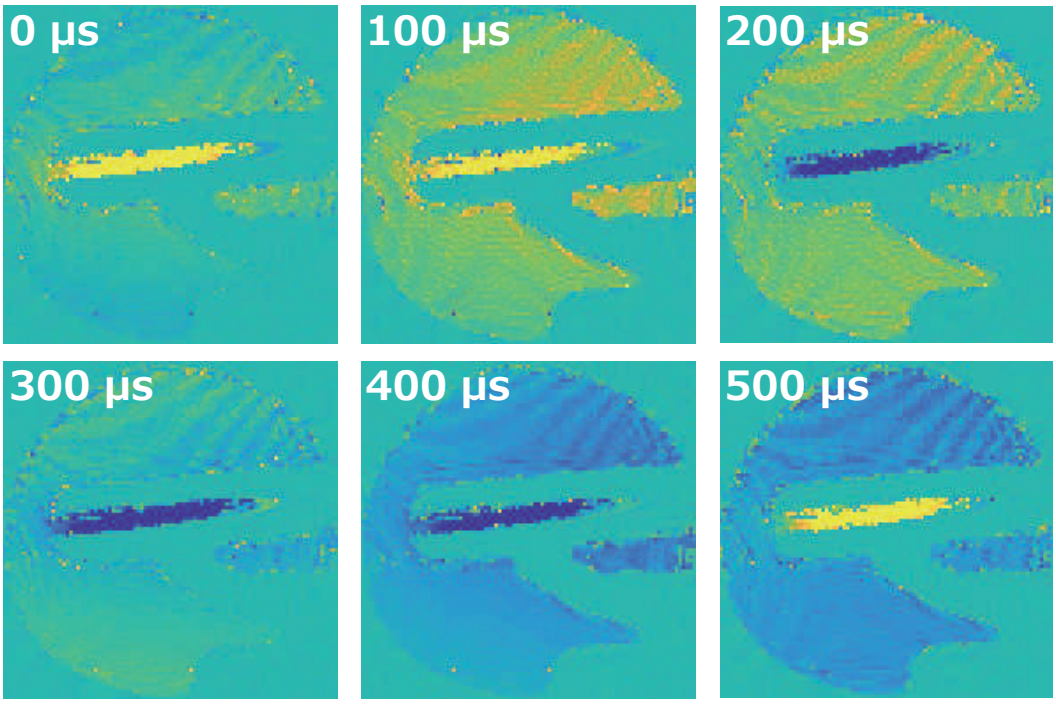

Figure 6.12: Filtered images by using the band-pass filter extracting the first mode of the castanets E. The intervals between each image is 100 μs.

eled by the Helmholtz resonance of the cavity inside the shells, (ii) sound radiation around 5 kHz from the acoustic resonance associated with the shell length, and (iii) sound radiation of frequencies higher than the second mode caused by shells deformation. Future works should establish a theoretical model based on the presented observations and apply it to the design of the instruments and the numerical computation of the castanets' sound.

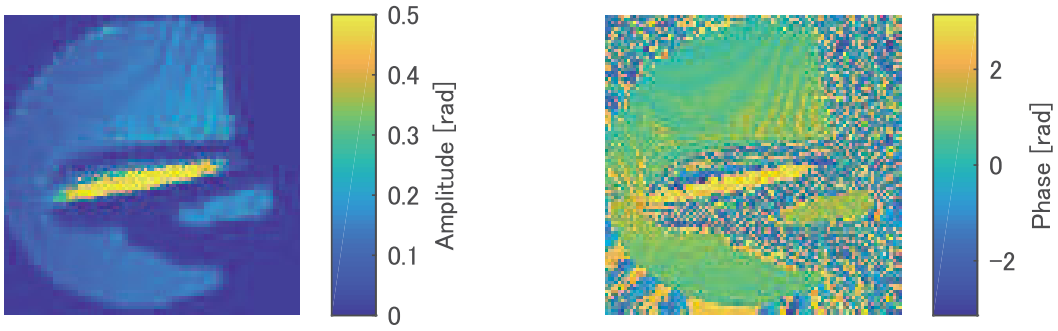

Figure 6.13: Amplitude and phase maps of the filtered images by using the band-pass filter extracting the first mode of castanets B.

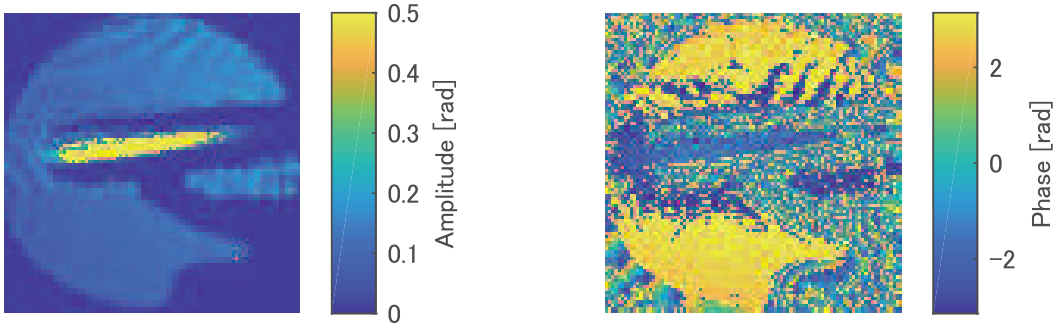

Figure 6.14: Amplitude and phase maps of the filtered images by using the band-pass filter extracting the first mode of castanets E.

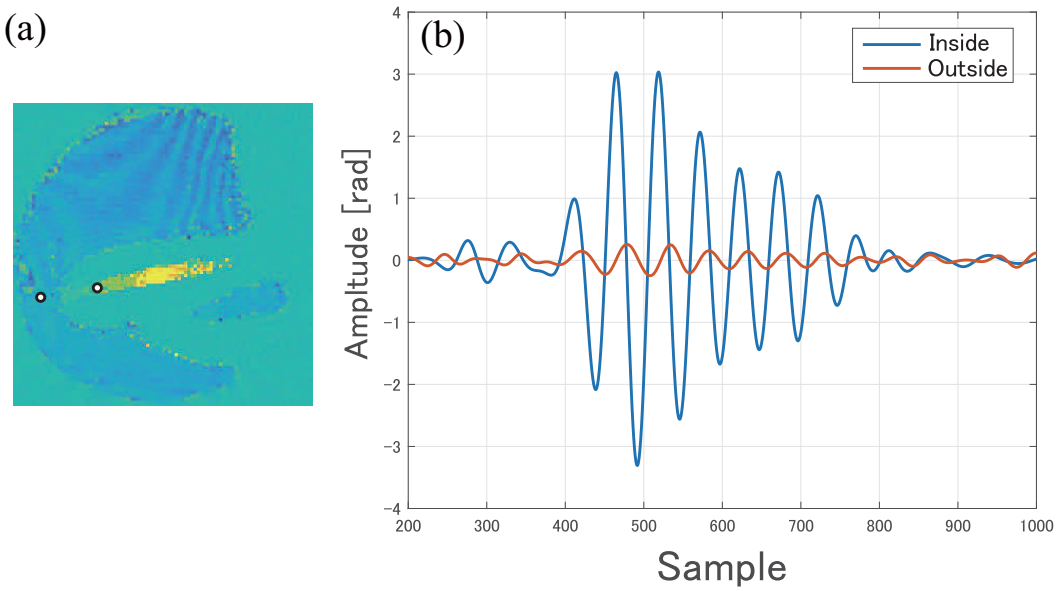

Figure 6.15: Waveforms extracted from the points inside and outside of the shells of castanets B.

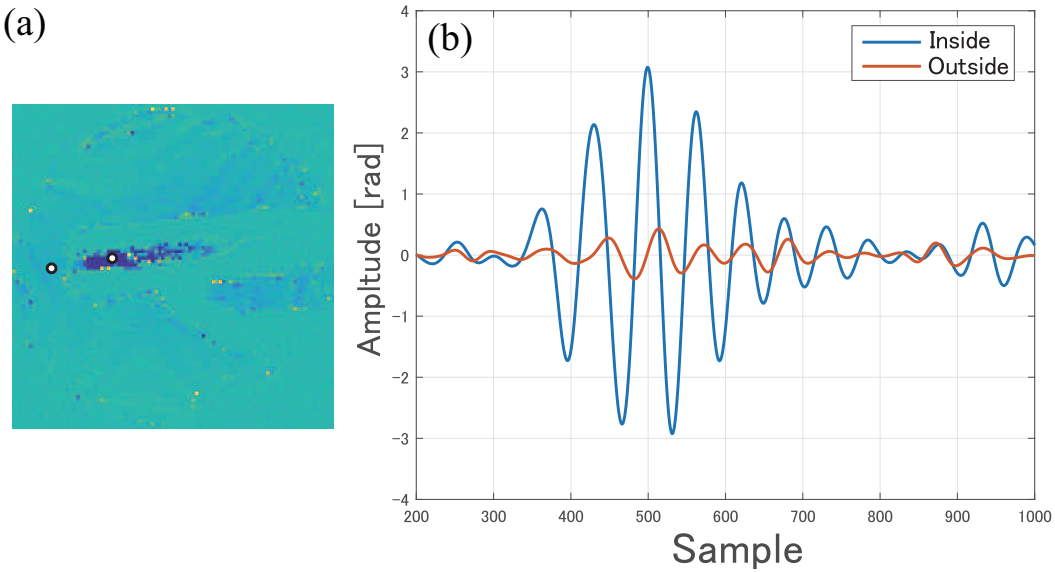

Figure 6.16: Waveforms extracted from the points inside and outside of the shells of castanets E.

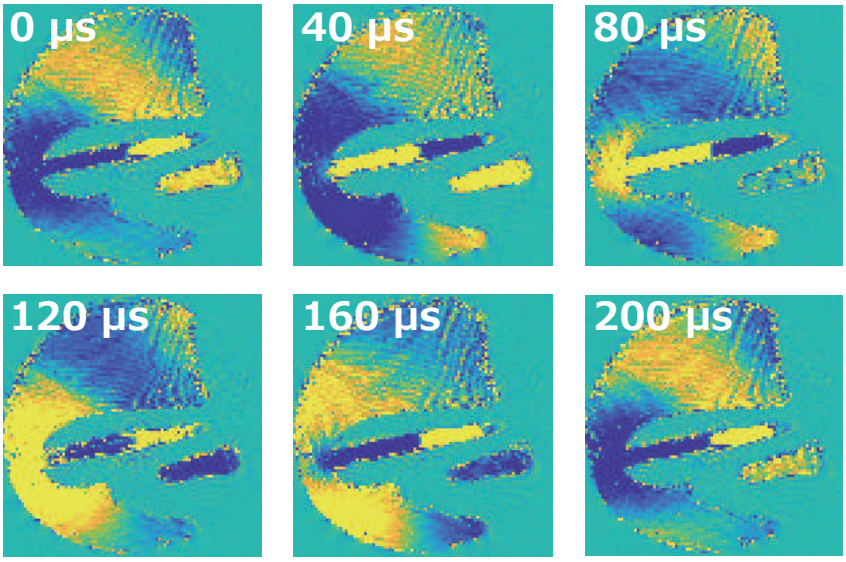

Figure 6.17: Filtered images by using the band-pass filter extracting the second mode of castanets B. The intervals between each image is 40 μs.

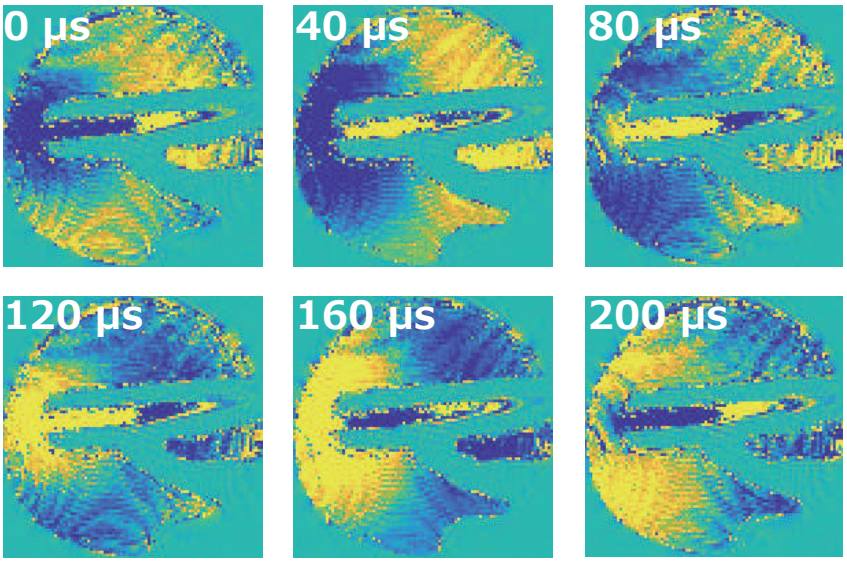

Figure 6.18: Filtered images by using the band-pass filter extracting the second mode of castanets E. The intervals between each image is 40 μs.

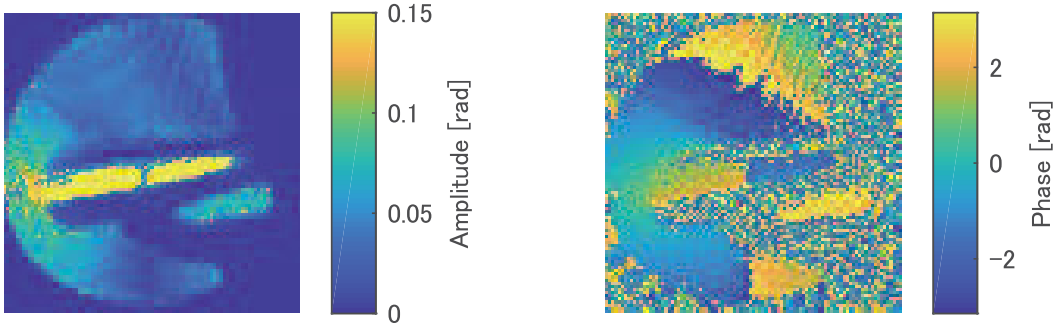

Figure 6.19: Amplitude and phase maps of the filtered images by using the band-pass filter extracting the first mode of castanets B.

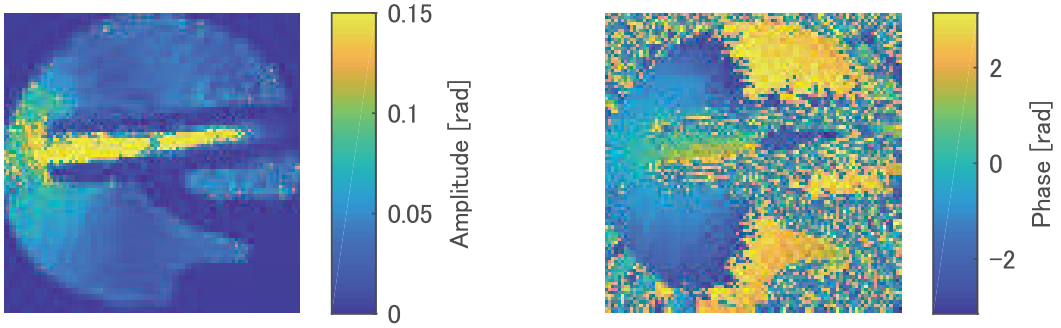

Figure 6.20: Amplitude and phase maps of the filtered images by using the band-pass filter extracting the first mode of castanets E.

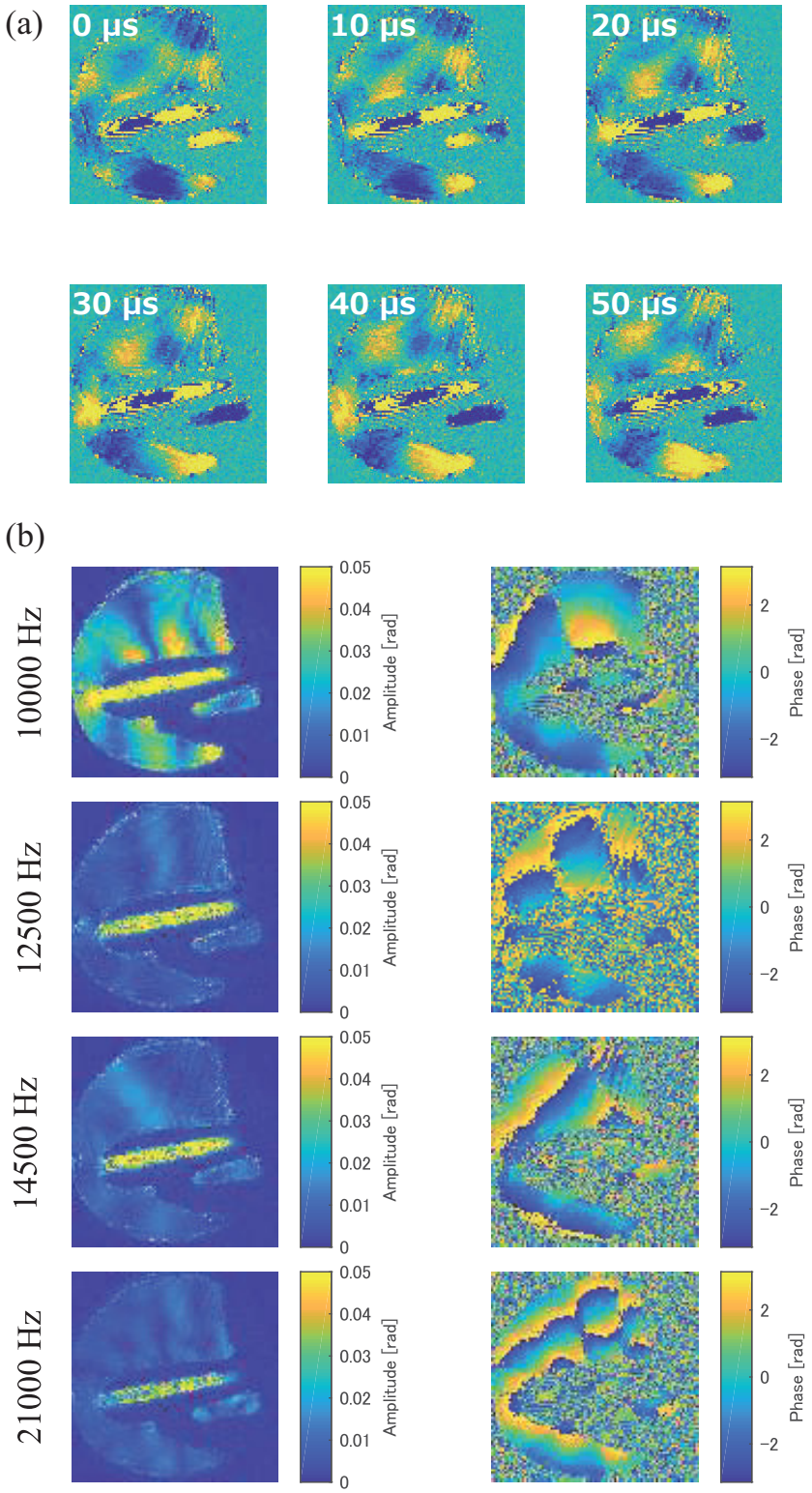

Figure 6.21: Results of castanets B filtered by the high-pass frequency of the cutoff frequency of 6 kHz. (a) Instantaneous fields. The intervals between each image is 10 μs. (b) Amplitude and phase maps of representative frequencies.

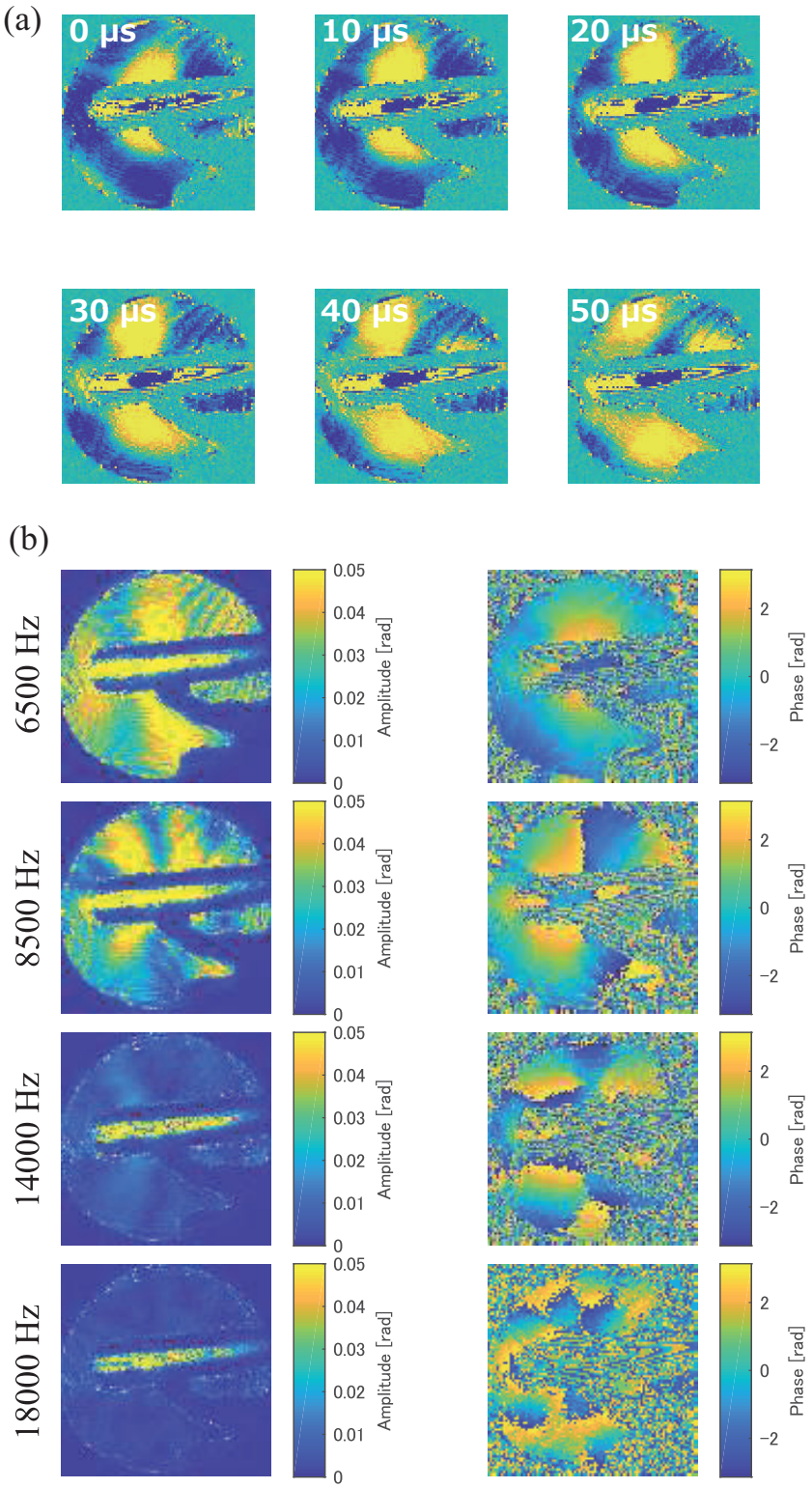

Figure 6.22: Results of castanets E filtered by the high-pass frequency of the cutoff frequency of 6 kHz. (a) Instantaneous fields,. The intervals between each image is 10 μs. (b) Amplitude and phase maps of representative frequencies.

Chapter 7

Simultaneous imaging of flow and sound

7.1 Background

Previous chapters demonstrated the feasibility and effectiveness of the imaging of sound fields using high-speed polarization interferometry. The application of PPSI includes not only sound but also the quantitative observation of other dynamic phenomena such as vibration [172–174], gas flow [175, 176], electric discharge [177], and microscopic phenomena [178–180]. Because PPSI enables the measurement of various phenomena, it is reasonable to consider measuring acoustical phenomena that involve the interaction of sound and other physical quantities. The simultaneous measurement of those would be useful for understanding the physics involved in these complex phenomena. As properties of these processes differ considerably, special attention should be given to the measurement.

By considering sound generation induced by flow, understanding the process of interaction between flow and sound is crucial in aeroacoustics. Modern aeroacoustics started with Lighthill's study [181]. Since then, a number of studies have been conducted to establish the physics of flow and sound [182] and reduce the noise caused by, for example, high-speed trains [183] and wind turbines [184]. Flow measurement is typically performed using optical methods such as particle image velocimetry [185–187] and the Schlieren method [23, 188, 189]; further, sound is measured by a traversing microphone [190] or a microphone array [191, 192] placed outside the flow field to avoid the contamination of the flow field by inserting the microphones into the field. Thus, measuring the sound field inside of the flow by microphones is quite difficult. On the contrary, the OMS can achieve the direct imaging of a sound field around flow owing to its contactless nature. Nakazono *et al.* measured the intensity map of acoustic standing waves exhausting from a nozzle near a screeching jet using a scanning optical laser microphone [193]. The Schlieren method has been used for the simultaneous imaging of flow and pressure waves such as jet screech [194, 195]. So far, the high-speed and simultaneous imaging of flow and sound in the audible range has not been achieved. The development of a simultaneous imaging method for the aeroacoustic phenomena in the human hearing

range, which includes aeroacoustic noise and aerophone sounds, is strongly desired. High-speed polarization interferometry was applied to aeroacoustic measurements and the simultaneous imaging of flow and sound was achieved, as will be detailed in this chapter.

7.2 Gas injection method and time-directional filtering

As the gas flow that causes the audible sound is typically incompressible, the airflow is invisible to the interferometer. Herein, I propose a gas injection method with time-directional processing for the simultaneous measurement of flow and sound. To observe the flow by the high-speed polarization interferometry, the gas, whose density is different from the surrounding air, is injected in the flow in place of the air. The relation between the density of the injected gas and the refractive index of the medium is given by Eq. (3.2) (the Gladstone-Dale relation), and the gas flow is visible to interferometry. The relation is given by

$$n = n_0 + \frac{n_0 - 1}{\rho_0} \Delta\rho, \tag{7.1}$$

where n_0 and ρ_0 are the refractive index and density of the static air, respectively; $\Delta\rho$ is the change in density. This equation indicates that the visibilities of gas flow can be controlled by adjusting the density of the injected gas.

To recognize sound waves in the phase image, the background phase orientation must be removed. As the background phase orientation exceeds 2π in most cases, the phase is must be unwrapped. In this measurement, time-directional processing is effective not only for sound extraction but also for flow attenuation. By applying the two proposals, both flow and audible sound can be captured, thus the simultaneous imaging is achieved for aeroacoustic problems in which sound is critical in the human hearing range. The following experiment was conducted to verify the feasibility of the proposed method.

7.3 Experiments

For the experiment, a whistle was used as a sound source, which was classified as an air-reed instrument. The sound was generated by the vibration of airflow and amplified by the acoustic resonance inside the cavity. The mechanism of air-reed instruments has long been studied [196,197]; however, the physics of the underlying phenomena has not been completely understood. Thus, the experimental observations of the dynamics of flow and sound are important.

Molar mass is an important property of the induced gas as it determines the visibility of flow. As the difference between the molar mass of the gas and that of the surrounding air increases, the change in optical phase increases; thus, flow visibility can be adjusted by changing the molar mass. In this experiment, 1,1-difluoroethane, with a molar mass of 66.05 g/mol, was used because its molar mass is sufficient to visualize the gas flow in the present situation. The frame rate of the camera was set to 42,000 fps, which was determined with respect to the frequency of the generated

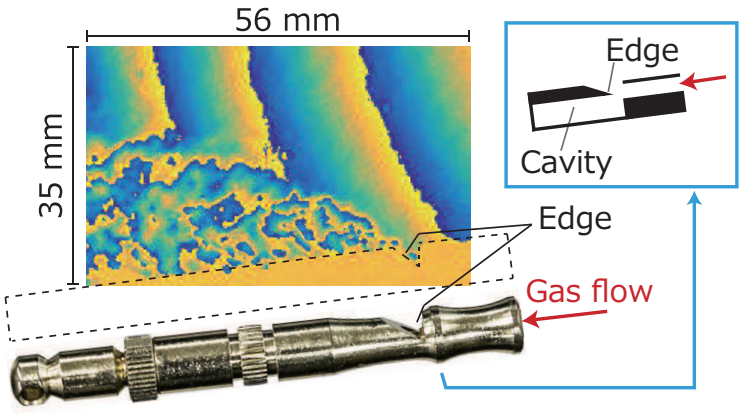

Figure 7.1: Example of the measured image and the photograph of the whistle.

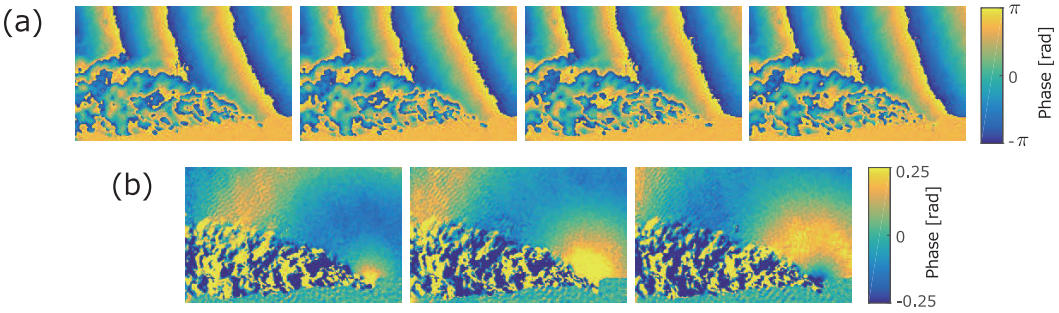

Figure 7.2: Imaging results. (a) Phase images of four successive frames. (b) Differential images of the images in (a). The color range was chosen with respect to the amplitude of the sound wave.

sound. The size of the measurement area was 56 mm × 35 mm, and the image resolution was 256 × 160. Figure 7.1 shows an example of the result to indicate the position and the structure of the whistle. The whistle was positioned at the bottom of the imaging area, and its input port was on the right side. As interference fringes did not appear when the whistle intercepted the light, the position of the whistle could be distinguished from the other parts in the image. The length of the cavity was approximately 7 mm, and its cross section was a circle. The sound was also recorded by a microphone for reference.

Figure 7.2(a) shows the measured phase maps without filtering. The fine patterns near the edge of the whistle are caused by the gas flow, and the periodical slanging lines are the phase discontinuities due to the wrap of phase. No sound wave was captured in the images because the phase variation caused by the sound was much smaller than 2π.

In Fig. 7.2(b), the differential images of two successive phase maps are shown. The periodic slanging lines due to the background phase orientation disappeared, and the spherical pattern, whose origin is near the slit of the whistle, is shown clearly. The spherical wave propagates outward from the origin, and the flow exists along the whistle. The power spectra calculated from the optical phase and micro-

phone data are plotted in Fig. 7.3. The spectrum obtained from the optical data is calculated from the averaged values of 10 pixels × 10 pixels in the upper-right part of the images. Both spectra exhibit two peaks at 8.7 kHz and 17.4 kHz. As the noise properties of the two instruments differ, the spectrum in the lower frequency region differ as well. The small peak at 15.9 kHz in the spectrum of the optical phase is caused by the aliasing of the third-harmonic components of the fundamental peak at 8.7 kHz. As the frequency of the third harmonics is 26.1 kHz and the sampling frequency of the camera was 42 kHz, the aliased component appears at 15.9 kHz. This is because the high-speed camera has no anti-aliasing filter. These discussions indicate that the spherical patterns in the images are the sound waves emitted from the whistle. Thus, the proposed method successively achieved the simultaneous imaging of flow and sound.

In both Figs. 7.2(a) and (b), the flow is visualized as the translation and deformation of the specific patterns. For a further analysis of the flow field obtained in Fig. 7.2(a), a similar analysis that was employed for the ordinal interferometric observation of the flow field such as velocity and vortex [198–200], can be used. For the flow in Fig. 7.2(b), the visualized patterns are related to the motion of the fluid particles due to the temporal differential operation. The trajectories of those might be determined via image processing schemes based on the correlation of two frames. In both cases, pointwise quantitative values would be reconstructed from the projections by applying a holographic reconstruction technique [199] or a tomographic reconstruction technique [201].

Finally, differential images with an interval of 200 frames are shown in Fig. 7.4 for observing the long-term trend. The origin of the time was chosen to coincide with the beginning of the flow emission. The temporal evolution of the gas flow is visualized clearly. Initially, the flow moved toward the upper-left; subsequently, it falls and propagates along the whistle. The gas fell because 1,1-difluoroethane is heavier than the surrounding air. After 30 ms from the gas emission, the sound appears gradually. These transient characteristics represent the acoustic resonance in the whistle cavity induced by the gas flow.

7.4 Conclusions

This chapter described the application of the high-speed polarization interferometry for the aeroacoustic problems. As the PPSI is sensitive to multiple physical phenomena including flow and sound, a simultaneous imaging of those were conducted. By injecting a gas whose density was different from the surrounding air, the gas flow was visualized; further, the sound wave became visible by applying time-directional filtering. Because the proposed method could visualize a sound field inside the flow, it would be an effective tool for the investigation of sound generation processes including aeroacoustic noise and aerophone sound. Furthermore, as the idea of using high-speed optical interferometry and time-directional processing can be applied to measure other complex physical phenomena, it can be applied to various fields including acoustics, fluid dynamics, thermodynamics, and applied mechanics.

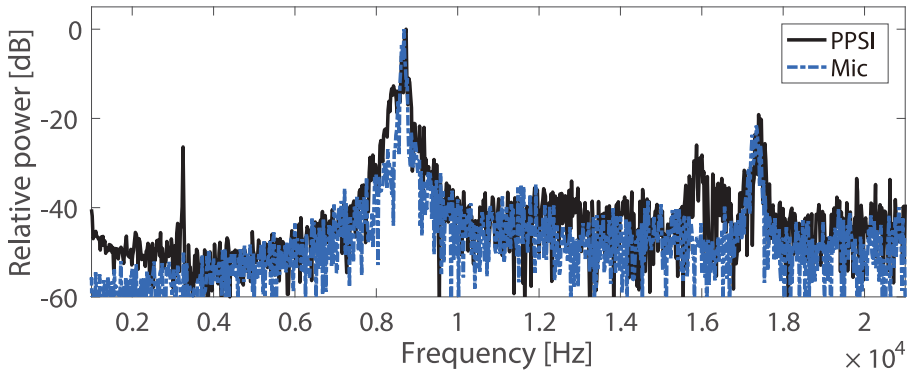

Figure 7.3: Power spectrum of the optical and microphone data. The spectrum obtained by the optical data was calculated from the averaged waveform of 10 pixels × 10 pixels in the upper-right area in the images.

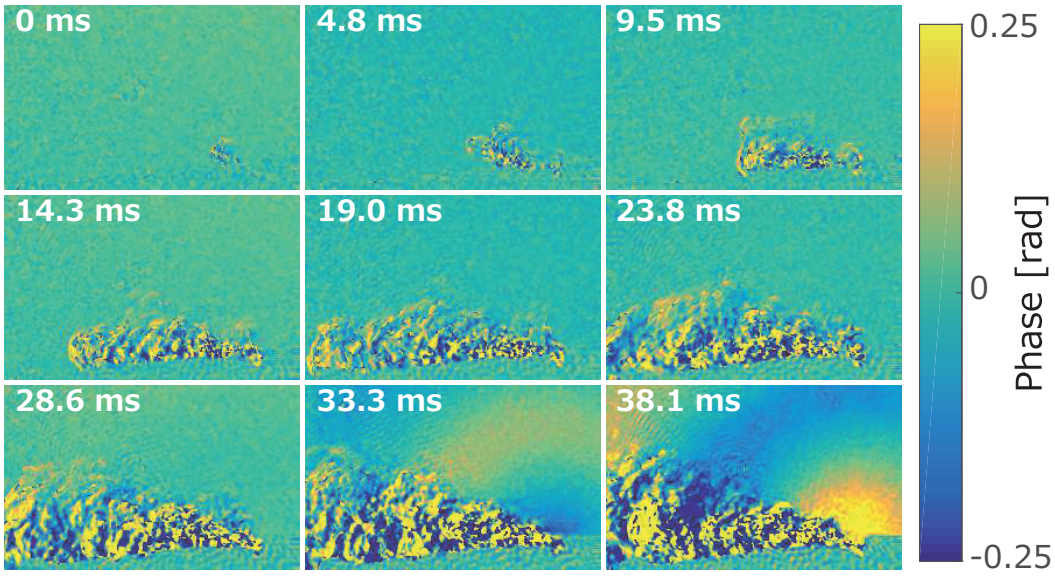

Figure 7.4: Differential images with an interval of 4.76 ms, corresponding to 200 frames. The emission of the flow began at 0 ms.

Chapter 8

Single-shot reconstruction of axisymmetric sound field

8.1 Introduction

To obtain a quantitative sound pressure using a microphone, the sensitivity of the microphone must be determined [2–4]. The pressure reciprocity technique is the most accurate calibration method for condenser microphones. The technique requires three microphones even though the sensitivity is a specific value for an individual microphone. The sensitivity is calculated by the acoustic transfer impedances of three pairs of microphones. Hence, the realization of sound pressure by the microphone is indirect.

On the contrary to the microphone calibration, the OMS has the potential to achieve the direct realization of sound pressure without any calibration. Koukoulas and Piper reported the absolute realization of sound pressure by the measurement of acoustic particle velocity by using gated photon correlation spectroscopy (GPCS) [202, 203]. They achieved the quantitative measurement of sound pressure in an anechoic chamber with less than 11 % deviation from the microphone measurement, from 500 Hz to 20 kHz in terms of sensitivity. However, because GPCS requires artificial seeding to increase the intensity of scattered light, additional measures must be performed such as ensuring trackability of the seeding particle to the air, and density uniformity of the seeding particles [204].

Another method to obtain an absolute sound pressure from the optical measurement is by reconstructing an original sound pressure field from the observation of projection of the field. Optical interferometry can measure quantitative values of the optical phase difference precisely, and the LDV has been used for this purpose [100, 119, 130, 133]. These methods, however, are time consuming for measurement because both the scanning of laser light and rotation of a sound field are necessary for the reconstruction.

In this chapter, the reconstruction of a three-dimensional quantitative sound field using the high-speed polarization interferometry is proposed. To realize the reconstruction from an instantaneous measurement, a sound field is assumed to be axisymmetric that is valid in many situations such as a microphone as an emitter,

a piston sound radiator, and an ultrasonic transducer. For the reconstruction, the axisymmetric sound field is modeled by the Helmholtz equation in the spherical coordinates, and the reconstruction problem is formulated as estimating the coefficients of the basis of the Helmholtz equation using the least-squares method. The experiments were conducted to verify the feasibility of the proposed method, and deviations between the microphone measurement and the proposed method were less than 1 dB for the frequencies between 5 kHz to 20 kHz.

8.2 Reconstruction of axisymmetric sound field

For the reconstruction of an axisymmetric three-dimensional sound field from the observation of two-dimensional line-integral sound pressure, a physical-model-based approach was employed. The reconstruction of an arbitrary three-dimensional sound field from optical measurements was proposed by Yatabe *et al.* [133]. The solution of the Helmholtz equation was approximated by the Herglotz wave function, and the coefficients of the model were estimated from the measured data by the least-squares method. Because observations from multiple angles (18 angles for their experiment) are necessary, a single-shot reconstruction cannot be realized. In this study, to achieve a single-shot reconstruction, an axisymmetric sound field is assumed and a reconstruction method for the axisymmetric field is proposed. By modeling the sound field using the Helmholtz equation in spherical coordinates, the azimuth dependence can be omitted. The problem is formulated as estimating the coefficients of the Helmholtz equation from the observed line-integral values.

8.2.1 Physical model of axisymmetric sound field

Consider the Helmholtz equation in the spherical coordinates (r, θ, ϕ),

$$\left(\Delta_s + k_s^2\right) p\left(r, \theta, \phi\right) = 0, \tag{8.1}$$

where

$$\begin{aligned} \Delta_s = \frac{1}{r^2}\frac{\partial}{\partial r}\left(r\frac{\partial}{\partial r}\right) &+ \frac{1}{r^2\sin\theta}\frac{\partial}{\partial\theta}\left(\sin\theta\frac{\partial}{\partial\theta}\right) + \frac{1}{r^2\sin^2\theta}\frac{\partial^2}{\partial\phi^2}, \\ \begin{bmatrix} r \\ \theta \\ \phi \end{bmatrix} &= \begin{bmatrix} \sqrt{x^2+y^2+z^2} \\ \tan^{-1}\frac{\sqrt{x^2+y^2}}{z} \\ \tan^{-1}\frac{y}{x} \end{bmatrix}, \end{aligned} \tag{8.2}$$

and k_s is the wavenumber of sound. When no sound source exists in the volume of interest, the solution of the spherical Helmholtz equation is given by

$$p\left(r, \theta, \phi\right) = \sum_{n=0}^{\infty}\sum_{m=-n}^{n} a_{mn} j_n\left(k_s r\right) Y_n^m(\theta, \phi), \tag{8.3}$$

where j_n is nth order Bessel function of the first kind,

$$Y_n^m\left(\theta, \phi\right) = \sqrt{\frac{2n+1}{4\pi}\frac{(n-m)!}{(n+m)!}} P_n^m\left(\cos\theta\right) \mathrm{e}^{im\phi} \tag{8.4}$$

is the spherical harmonics, and a_{mn} is the coefficient [205]. By regarding the z axis in the Cartesian coordinate (x, y, z) as the symmetric axis, the sound field is independent of ϕ; therefore, the solution becomes

$$p(r,\theta) = \sum_{n=0}^{\infty} a_n j_n(k_s r)\sqrt{\frac{2n+1}{4\pi}} P_n(\cos\theta), \tag{8.5}$$

where $P_n(x)$ is the nth order Legendre polynomial.

8.2.2 Reconstruction from optical observation

The data obtained by high-speed polarization interferometry is represented by

$$d_{i,j} = C\int_{\boldsymbol{L}_{i,j}} p(\boldsymbol{l},t)d\boldsymbol{l}, \tag{8.6}$$

where (i, j) is the index of the camera pixel, $C = k(n_0-1)/(\gamma p_0)$, $\boldsymbol{L}_{i,j}$ is the optical path corresponding to (i, j) pixel, and $d\boldsymbol{l}$ represents a line element. By substituting Eq. (8.5) into Eq. (8.6), the observed data are given by

$$d_{i,j} = \sum_{n=0}^{\infty} a_n \bar{\Upsilon}_{n,i,j}, \tag{8.7}$$

where

$$\bar{\Upsilon}_{n,i,j} = \int_{\boldsymbol{L}_{i,j}} j_n(k_s r)\sqrt{\frac{2n+1}{4\pi}} P_n(\cos\theta)\, d\boldsymbol{l}. \tag{8.8}$$

The term $\bar{\Upsilon}_{n,i,j}$ depends on the wavenumber of sound, the order of the basis function, and the optical path; it is independent of the measured data. Assuming that the resolution of a recorded image is I × J and the order of the solution is truncated by N, Eq. (8.7) can be written in the matrix form:

$$\boldsymbol{d} = \Upsilon\boldsymbol{a}, \tag{8.9}$$

where $\boldsymbol{d}$ is the data vector of I × J elements, Υ is the matrix of I × J rows and N columns, and $\boldsymbol{a} = \{a_1, ..., a_N\}^{\mathrm{T}}$. As $\boldsymbol{d}$ and Υ are obtained from measurement and its configuration, the coefficient $\boldsymbol{a}$ can be estimated by solving Eq. (8.9). For estimating coefficients $\boldsymbol{a}$, a least-squares method can be used. As the measured data by optical interferometry contains noise, the estimated values might be contaminated by it. Therefore, a truncated singular method was applied, similar to the previous method [133]. The coefficient matrix Υ can be factorized by

$$\Upsilon = U\Sigma V^H, \tag{8.10}$$

where U and V are the unitary matrices, Σ is the diagonal matrix, and V^H represents the Hermitian transpose of V. The ith diagonal entries of Σ, σ_i, correspond to the ith singular value, where $\sigma_1 \geq \sigma_2 \geq \cdots \geq \sigma_N$. The truncated singular value method performs the truncation to the singular values that are smaller than the threshold $\tau\sigma_1$. Then, the pseudo-inverse of the coefficient matrix Υ becomes

$$\Upsilon^{\dagger} = V\Sigma_{\tau}^{-1}U^H, \tag{8.11}$$

where Σ_τ^{-1} is the inverse matrix of the truncated diagonal matrix. Finally, the coefficient vector $\boldsymbol{a}$ is calculated by

$$\boldsymbol{a} = \Upsilon^\dagger \boldsymbol{d}. \tag{8.12}$$

By substituting $\boldsymbol{a}$ into Eq. (8.5), the three-dimensional sound field is reconstructed.

8.2.3 Calculation procedure

Here, the calculation procedure of the proposed method is summarized. Initially, the recording of an axisymmetric sound field by the optical system is performed. Then, from the obtained interferograms, optical phase maps are calculated by using the HEFS method [163, 164]. This calculation is performed in each frame, and the time sequence of the two-dimensional phase maps is obtained. As the reconstruction algorithm is defined in the wavenumber domain, the time-directional Fourier transform is performed for each pixel. When applying the proposed reconstruction algorithm, a single Fourier-transformed image that represents a two-dimensional map of a complex amplitude of a certain frequency, is extracted. The matrix of I rows and J columns is reshaped to the vector of $I \times J$ elements, which is data vector $\boldsymbol{d}$ in Eq.(8.9).

To calculate the coefficient matrix Υ, the optical path $\boldsymbol{L}_{i,j}$ must be identified. For a sound field in the air, the optical path can be assumed as a straight line. As pixels are equally distributed on an image sensor, the intervals between the optical paths are derived by d in Eq. (4.14). The optical path can be expressed

$$\boldsymbol{L}_{i,j} = \{\boldsymbol{P}_{i,j} + \alpha \boldsymbol{Q}_{i,j} | \alpha \in [0, 1]\}, \tag{8.13}$$

where $\boldsymbol{P}_{i,j} = (x_a, y_i, z_j)$; $\boldsymbol{Q}_{i,j} = (x_b, y_i, z_j)$; x_a and x_b are the start and end positions of the optical path, respectively; $y_i = \delta(i-1) + y_1$, and $z_j = \delta(j-1) + z_1$. The positions y_i and z_j are determined based on the measurement configuration. By substituting the optical path into Eq. (8.8) and determining the expansion order N, Υ is obtained.

The coefficient vector $\boldsymbol{a}$ is estimated by using the truncated singular value method as explained in the previous section. For the reconstruction, by substituting $\boldsymbol{a}$ in Eq. (8.5), a complex amplitude at an arbitrary position can be calculated. After performing the reconstruction for all frequencies, performing the inverse Fourier transform at each position recovers the time-domain waveform. By this procedure, the axisymmetric sound field can be reconstructed.

8.3 Experiments

8.3.1 Setup

To verify the proposed measurement and reconstruction method, comparisons of sound pressure levels measured by the proposed method and a calibrated quarter-inch microphone were conducted. For generating an axisymmetric sound field, a loudspeaker of rotationally symmetric shape (DIATONE TW-G500) was used.

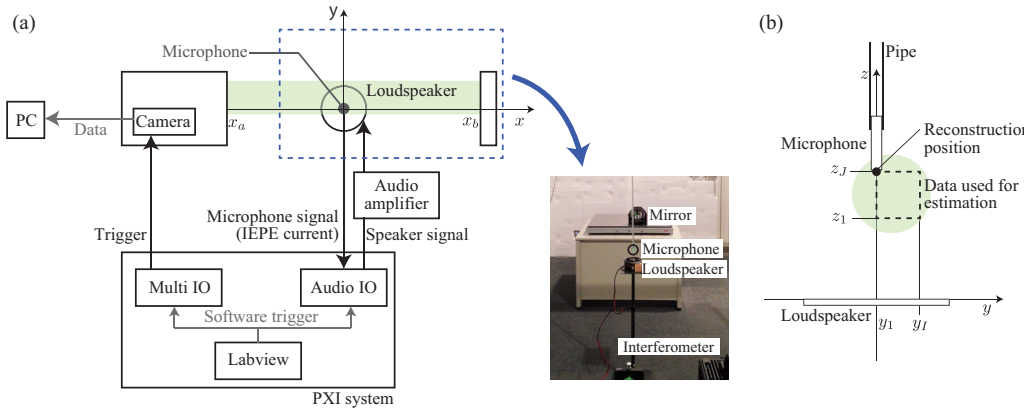

Figure 8.1: Experimental configuration.

The positional condition of the measurement is illustrated in Fig. 8.1(b). The loudspeaker was placed 10 cm below from a microphone diaphragm. A quarter-inch microphone (GRAS 46BE) was placed on the symmetric axis of the loudspeaker. As the proposed method assumes an axisymmetric sound field, a microphone was placed on the symmetric axis to avoid the non-axisymmetric scattering of the sound wave. Further, for reducing the scattering from fixtures, the microphone was affixed at the bottom of a circular pipe of 1 m length hung from an aluminum frame. As a free field microphone measures sound pressure without a microphone in a free field, the microphone was removed during the measurement by high-speed polarization interferometry.

The schematics of the measurement system are shown in Fig. 8.1(a). The input signals were sinusoidal waves of frequencies 1 kHz to 20 kHz with 1 kHz steps. The amplitude of the input signal was adjusted such that the sound pressure level was approximately 110 dB at the position of the microphone. The frame rate of the camera was 100,000 fps and the shutter speed was 10 μs. The original image resolution was 512 $\times$ 512, and only a suitable part for reconstruction was cut out from the recorded images. The number of recorded frames was 500 for each frequency. The sampling rate of the microphone measurement was 100,000 Hz. The starting times of the microphone data acquisition and the camera recording were controlled by an external trigger, but the sampling clocks were different.

The parameters of the reconstruction were as follows: $N = 5$, $\tau = 0.01$, $\delta = 3.46 \times 10^{-3}$, $z_1 = 0.1$, $y_1 = 0$, $x_a = -1.25$, $x_b = 1.25$. The size of the measurement area was 26.30 mm $\times$ 30.10 mm. The temperature and humidity of the experimental room were 28.8 C° and 58 %, respectively. Thus, the speed of sound, c, was 348.7 m/s, and it was used for calculating the wavenumber $k = \omega/c$, where ω is the angular frequency of sound.

8.3.2 Results

The measured sound pressure levels are plotted in Fig. 8.2. The plotted values are the deviation from the microphone values at each frequency. The error bars

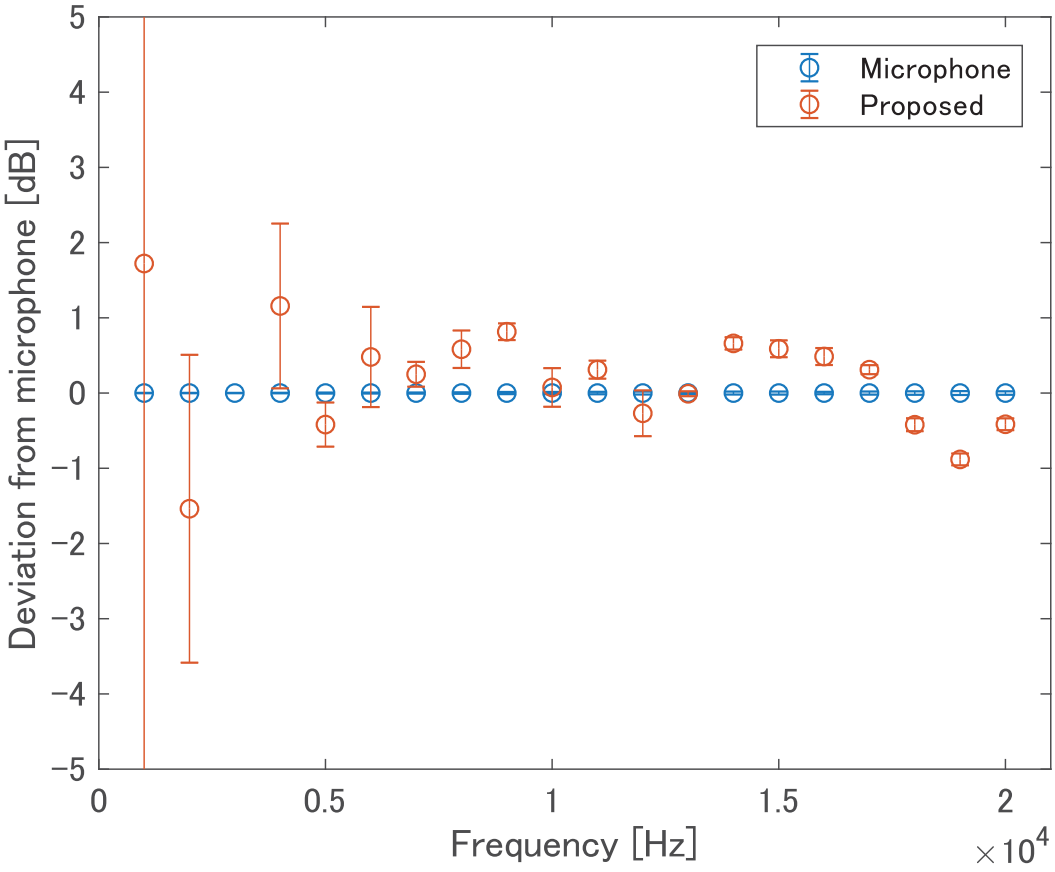

Figure 8.2: Obtained sound pressure levels of the microphone and proposed optical measurements. The values represent deviations from microphone values. Error bars indicate the standard deviation of the five repeated measurements.

show the standard deviation of the five repeated measurements. The graph shows that the standard deviation of the frequencies below 4 kHz is larger than that of other frequencies. This is because the background noise of the measurement system increases at that frequency range. The large error observed at 3 kHz, i.e., the deviation of 8.98 dB, is due to the camera fan noise. Further, the standard deviation at 6 kHz is larger than those of 5 kHz and 7 kHz due to the second harmonic of the fan noise. For the frequencies higher than 5 kHz, the deviations from the microphone values are less than 1 dB.

The reconstructed three dimensional sound fields of 10 kHz, 15 kHz, and 20 kHz are plotted in Fig. 8.3. The values of the proposed system plotted in Fig. 8.2 were extracted from $(x, y, z) = (0, 0, 0.1)$. The reconstructed fields are smooth and should be reasonable profiles as the sound field of each frequency.

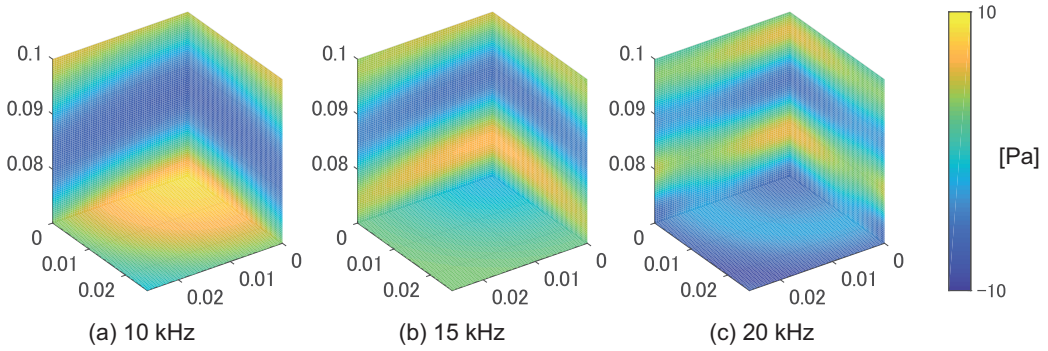

Figure 8.3: Examples of the reconstructed three-dimensional sound fields.

8.4 Discussions

8.4.1 Model error

For performing the reconstruction of a three-dimensional sound field from an instantaneous measurement, the sound field was assumed to be axisymmetric, and a loudspeaker with a spherically symmetric shape was chosen. Nevertheless, the spatial profiles of the generated sound fields may not be completely axisymmetric. Thus, the deviation from the symmetric profile was investigated using a microphone and a rotation motorized stage. A microphone was affixed at the position 10 mm from the symmetric axis. The loudspeaker was rotated with 10° steps and the sound pressure was measured at 36 positions. For evaluating the amounts of asymmetry, the deviation from the symmetric profile, μ, was calculated by

$$\mu = \frac{1}{N} \left| \Sigma_{i=1}^{N} L_i - L_{\text{mean}} \right|, \tag{8.14}$$

where N is the total number of measurements, L_i is the sound pressure level at the ith position, and L_{mean} is the mean sound pressure level. The calculated results at each frequency is plotted in Fig. 8.4. Large deviations are observed at the higher frequencies. The polar plots of the sound pressure level and phase of 19 kHz are shown in Fig. 8.5. The plots show that the sound field at 19 kHz does not satisfy the axisymmetric assumption. Although this would cause experimental deviations larger than 1 dB for the frequencies higher than 10 kHz, the experimental results show less deviation. As the infinite sum of the Bessel function and Spherical harmonics is truncated by 5, the rapid changes in the spatial profiles cannot be reconstructed. This would reduce the deviations in the reconstructed values compared to μ.

8.4.2 Phase-shifting error

The optical phase measurement using PSI is often violated by a periodic error caused by the misconfiguration of phase-shifting elements [206]. When the sound is measured by the PSI, it is found that the phase-shifting error affects the amplitude of optical phase map at the frequency of sound. Figure 8.6 shows a wrapped phase map of a certain frame and the acoustic power map at 10 kHz when a 10-kHz sound

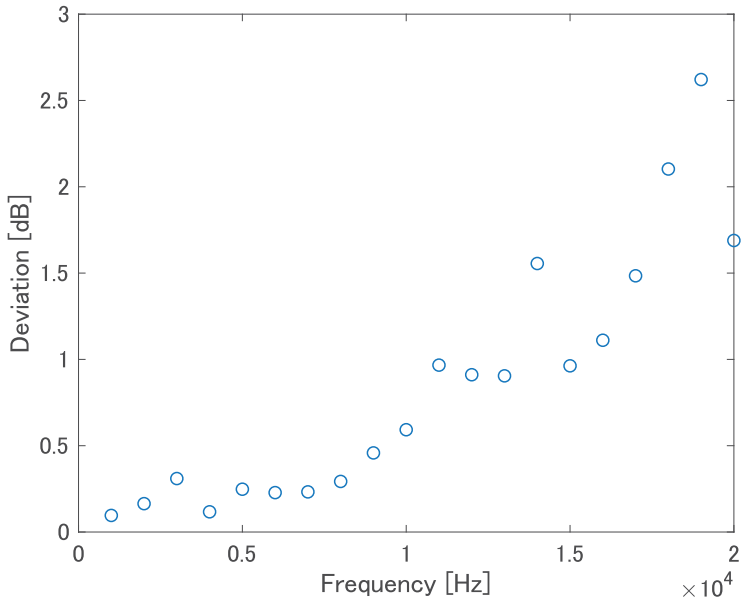

Figure 8.4: Deviation of the sound fields generated by the loudspeaker from the axisymmetric assumption. The deviations are calculated by Eq. (8.14) from microphone measurements.

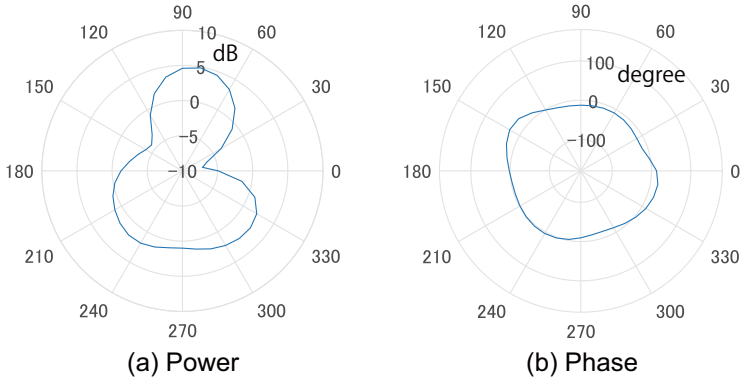

Figure 8.5: Polar plots of the power and phase of the sound field generated by the loudspeaker at 19 kHz.

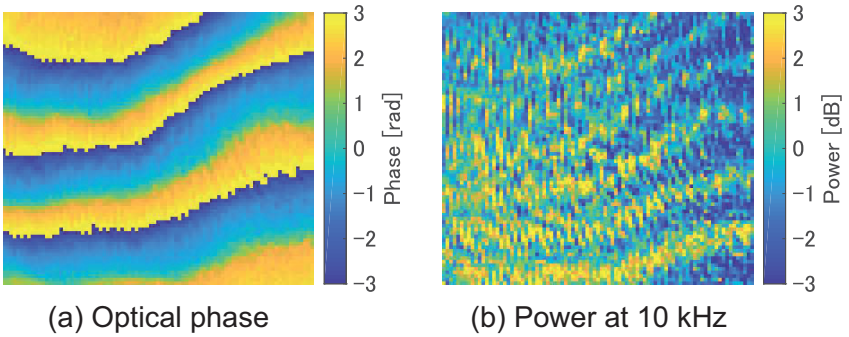

Figure 8.6: (a) Wrapped phase of a certain frame calculated by the HEFS method. (b) Acoustic power map at 10 kHz.

wave was recorded. The power map shows a periodic fluctuation that apparently depends on the wrapped phase. The period of the power map is half of that of the phase map. This characteristic is identical to Kimbrough's results [206], and this type of error can be reduced by using an ellipse fitting algorithm. The results reported herein were calculated by using the HEFS method [163, 164], which is an advanced algorithm based on the ellipse fitting. The remaining errors may be due to the spatial and temporal variations in the phase-shifting errors, and are likely to occur for the optical systems involving a phase-shifting array device such as a high-speed polarization camera.

Although the variation due to the phase-shifting error is approximately 3 dB at tje maximum, the reconstructed results contain smaller variations. As the spatial pattern of this noise is finer than that of the sound fields, as shown in Fig. 8.3(a), the reconstruction process might eliminate the fine pattern caused by the phase-shifting error.

8.4.3 Estimation error

The error involved in the reconstruction process described in Section 8.2.2 is investigated numerically. For the sound source, a monopole was set at the origin, and the integrated sound field was calculated to simulate the measured data of the experiments. The measurement and reconstruction parameters were identical to those used for the experiments. The original sound field and reconstructed sound field at the position corresponding to the microphone were compared. The results are plotted in Fig. 8.7. The vertical axis represents the differences between the original and reconstructed sound fields. The largest error appears at 2 kHz and the deviation is approximately 1 dB. The errors tend to increase as the frequency decreases, except for 1 kHz. This trend may be because, as the frequency of sound decreases, only a small part of the sound wave is observed in a single image. For example, the wavelength of a 2-kHz sound is approximately 174 mm. As the size of the measurement area is 26.30 mm $\times$ 30.10 mm, only one-sixth of the wavelength is captured in an image. This situation makes the reconstruction difficult.

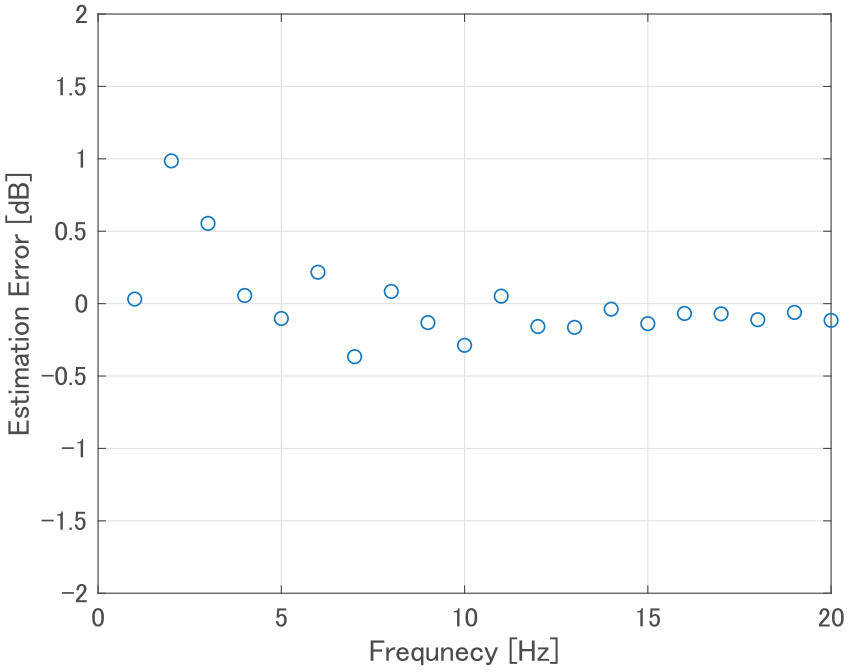

Figure 8.7: Estimation error of the reconstruction method obtained by numerical simulation.

Finally, the influence of the truncated value τ was investigated. Figure 8.8 plots the deviation from the microphones and the standard deviation of the experimental results when $\tau = 0.1, 0.01, 0.001$. As τ becomes large, the standard deviation decreases. This is because more truncations of singular values decreases the power of random noise. Thus, a smaller standard deviation does not imply a smaller uncertainty. According to Fig. 8.8, the case $\tau = 0.01$ indicates the best result among the three parameters. To obtaine a suitable parameter for the estimation, numerical methods such as the L-curve method should be used [207].

8.5 Conclusions

This chapter described the reconstruction method for obtaining a quantitative axisymmetric sound field from the projected data measured by the high-speed polarization interferometry. The experimental results indicated that the reconstructed values agreed with the reference microphone values with deviations of less than 1 dB within the frequency range of 5 kHz to 20 kHz. Future works should investigate suitable parameters for reconstruction and expand the applicable frequency range to the lower side.

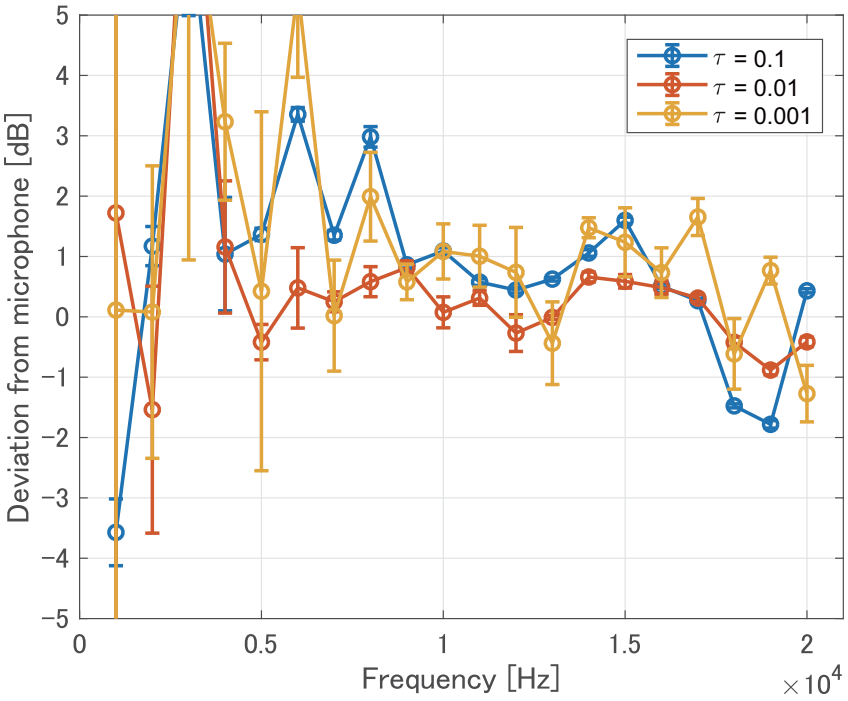

Figure 8.8: Experimental results for different τ.

Chapter 9

Conclusions

9.1 Summary

A microphone is essential in modern acoustics, and optical technologies have provided different choices for the acoustical measurement. Owing to its contactless nature, the OMS has enabled the measurement of various sound fields including the fields where microphones are difficult to use.

This thesis proposed the optical method, named high-speed polarization interferometry, for the contactless, instantaneous, and quantitative measurement of a two-dimensional sound field in air, in particular, the sound field in the human hearing range. By employing an optical system comprising a high-speed polarization camera and the Fizeau-type polarization interferometer, such a measurement was realized. The validity of the proposed method was confirmed by the fundamental experiments including a comparison with the microphone measurement and the numerical simulation as described in Chapter 4.

The contactless and instantaneous nature of the proposed method enabled the measurement of various sound fields in the audible range. In Chapters 5, 6, and 7, the applicability of the proposed method to engineering acoustics, musical acoustics, and aeroacoustics was investigated, respectively. The effectiveness of the proposed method to those fields was confirmed experimentally. In Chapter 8, a method to reconstruct a three-dimensional axisymmetric sound field was proposed, and the experimental results indicated that the proposed system could yield the quantitative sound pressure value with a deviation of less than 1 dB at the frequencies between 5 kHz to 20 kHz without any calibration.

9.2 Limitations and remaining issues

A limitation of the high-speed polarization interferometry was the size of its measurement area. The size was determined by the diameter of the object light. Expanding the measurement area required a large-size mirror and lens. If a system could encompass a human or an entire room, more acoustical phenomena, particularly sounds deeply related to humans such as voice and low-frequency noise, could be visualized effectively; the realization of such a system is preferable. The con-

struction of the large size system is currently hampered by its cost. Because the optical elements for the interferometer must be fabricated at the nanometer to sub-nanometer accuracy, their costs increases rapidly as their sizes increase. Therefore, for the realization of a large system, the developments of optical technologies such as a method for fabricating low-cost and large elements, and a better configuration of the optical system are necessary.

Reducing the minimum detectable sound pressure level is also desired. The level depends on the amount of noise of the measurement system and the signal processing scheme. For increasing the signal-to-noise ratio (SNR) of the measurement, increasing the power of the light source and cooling the image sensor and optical elements are effective. Using an appropriate signal processing method also contributed to increasing the SNR. Several methods have already been proposed [12,56–58,208,209], and applying them will enhance the visibility of the measurement results.

Another important issue to be addressed is the integral effect. The OMS based on the AOE measures a quantity proportional to the line integral of sound pressure along an optical path. As shown in previous chapters, the visualized field was quite informative and useful for numerous acoustical applications even though the values were integrated. However, the quantitative evaluation of an acoustical quantity and the detailed investigation of a three-dimensional sound field require the reconstruction of point-wise information. The existing reconstruction algorithms can be applied when projections from multiple angles are available. As described in Chapter 8, the reconstruction from a single measurement was achieved when a sound field was axisymmetric. Nevertheless, the instantaneous measurement and reconstruction of an arbitrary sound field have not been achieved yet.

9.3 Future remarks

The OMS resulted in the expansion of measurable sound fields; in particular, the OMS is expected to reveal acoustical phenomena and the creation of preferable acoustical environments by the observation of the spatial distribution of sound fields. For the further development of the proposed method, the following two topics should be researched as well as the improvement in fundamental performances such as the size of the measurement area.

One is the measurement of a three-dimensional sound field. As stated in the previous section, the reconstruction of an arbitrary three-dimensional sound field from the line integral of sound pressure, which is observed by the high-speed polarization interferometry and the other methods employing the AOE, has not been achieved yet. If the instantaneous, quantitative, and contactless measurement of an arbitrary three-dimensional sound field is accomplished, the recording of the sound field itself is achieved; consequently, all acoustical quantities can be calculated from the recorded data. To realize this, two approaches can be used, namely, improvement of the measurement system and development of signal processing. For the measurement system, the simultaneous operation of multiple interferometers, high-speed scanning of a probing beam, and temporal, spatial, or wavelength multiplexing of multiple projection data can be considered. In any case, the accuracy and cost of

the configuration of the optical system will be important factors. Signal processing presents many choices including the improvement of an optimization method based on the physical model of sound, applying optical digital holography, and the use of compressive sensing. Any of these can be used with others; for example, the combination of the minimum number of optical systems and advanced signal processing schemes.

The other is how to extract meaningful information from observed data. The spatial resolution of the sound field obtained by the high-speed polarization interferometer is much higher than that of an ordinal microphone array. This allows us to understand a phenomenon by only displaying the measurement results as images or videos. Meanwhile, one might misinterpret or overlook the results because important information might be hidden in the numerous data. Thus, data analysis methods that aim at extracting useful information from the numerous data, will be an important subject of research for the development of the effective applications of the high-speed polarization interferometer. If the processing schemes for the identification of sound source position, vector representation of a sound field, and calculation of acoustical quantities such as acoustical source power and directivity of a sound source are realized, the high-speed polarization interferometer can be used immediately in industrial situations.

The future impacts of the high-speed polarization interferometry and the OMS, which can be expected when the above issues are addressed, are illustrated in Figs. 9.1 and 9.2. Figure 9.1 summarizes the potential applications of the high-speed polarization interferometry. By sophisticating the measurement system, it can be applied to many acoustical problems and will contribute toward a new metrological standard. On the contrary, by generalizing the method, the commercial uses of the method will be realized. Pursuing both sophistication and generalization may yield a new interdisciplinary research field and realize the recording of an entire three-dimensional acoustic field.

Figure 9.2 illustrates the future impacts in the three categories depicted in Fig. 9.1. High-speed polarization interferometry can contribute to the progress in many branches of the acoustics including physics, society, and industry. As these measure the spatial profile of a sound field with high-spatial density and wide frequency range without any contamination to the sound field, they will contribute to solving unsolved problems in physical acoustics. The optical methods also influence our daily lives by its ability to provide new methods to observe and display the acoustic environment. The studies to establishing new acoustical standards based on the OMS has recently been started, and they will provide better standards than the current microphone-based standards. For industries, the capability of observing the spatial profile of a sound field can provide new diagnostics for investigating the acoustical properties of a product. For example, as a high spatial resolution renders the identification of the position of a sound source more accurate, the high-speed polarization interferometer can help engineers who are struggling in reducing noise.

The high-speed polarization interferometry is effective for not only acoustics but also complex physical phenomena such as fluid flow, heat, deformation, and vibration. The importance of interdisciplinary research is increasing with the complicated

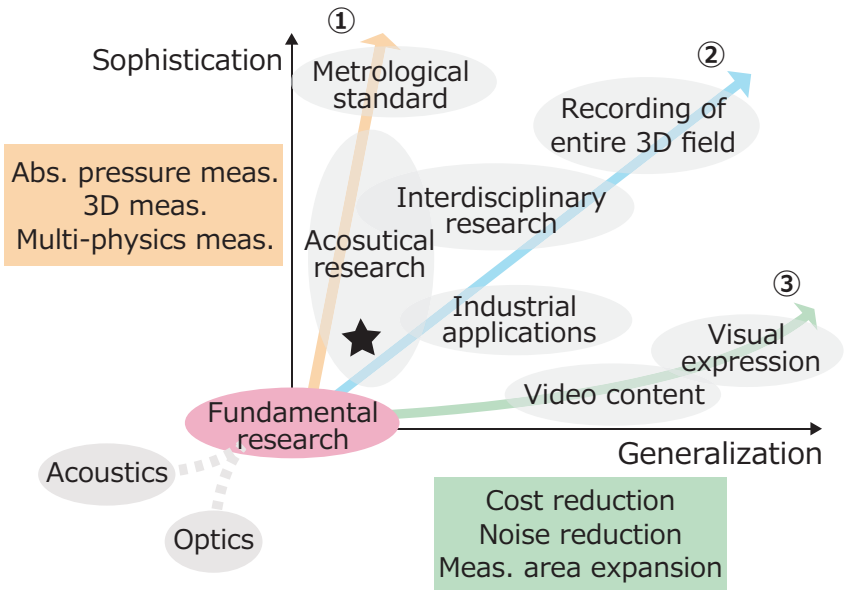

Figure 9.1: Map of the potential applications of the high-speed polarization interferometry. The star mark represents the current position.

society, and optical measurement methods will be powerful tools for solving complex issues in science and engineering. The capability of observing multiple phenomena and interactions will generate new and interesting research subjects by combining with other domains such as data science, mathematics, and art.

Another interesting topic is to interpret the measured data as a new visual expression. The proposed method provides a new experience: seeing sound. For educational purposes, seeing the generation and propagation of sound helps learners to understand the fundamentals of acoustics. The visualization of sound around us will be a new content in the entertainment industry, as well as a high-speed camera yielding visual expressions by slow-motion videos. These expressions will be more effective when used with the recent display technologies such as augmented reality, mixed reality, and holographic display.

In summary, the high-speed polarization interferometry and the OMS are promising for realizing innovations in acoustical measurements and can affect various fields. For the further development of those, the contributions from both acoustical and optical communities are required. An outstanding invention is expected through an interconnected research effect among acoustics, optics, and other fields of science, engineering, and society.

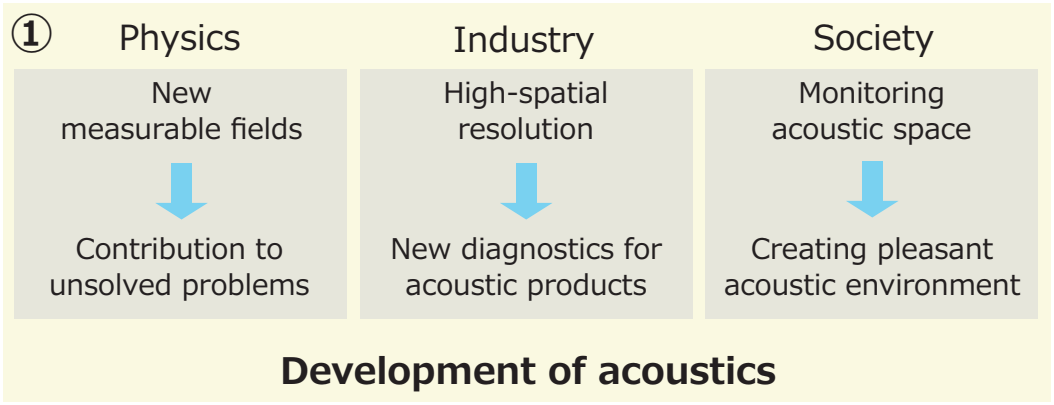

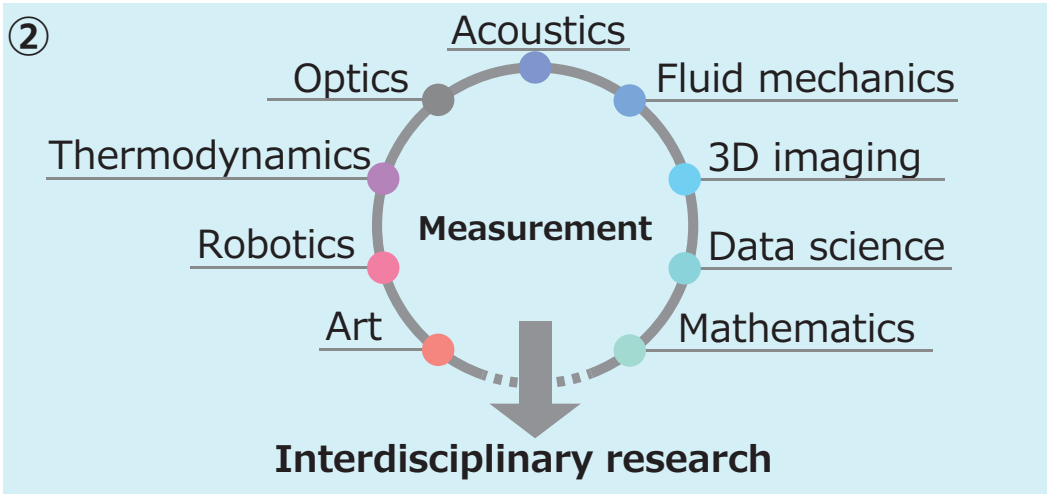

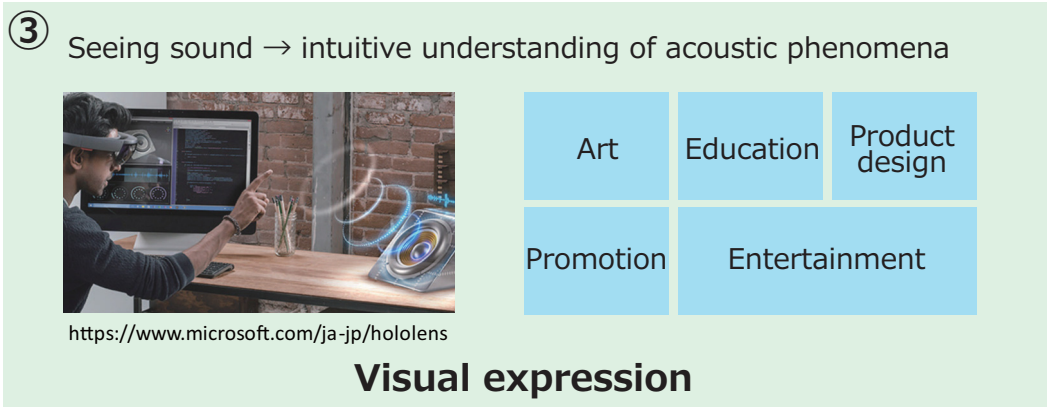

Figure 9.2: Future impacts of the high-speed polarization interferometry in the three categories depicted in Fig. 9.1.

Bibliography

[1] BIPM, *International Vocabulary of Metrology - Basic and General Concepts and Associated Terms*, 3rd ed. (2012).

[2] E. C. Wente, "A condenser transmitter as a uniformly sensitive instrument for the absolute measurement of sound intensity," Phys. Rev. **10**, 39–63 (1917).

[3] Brüel & Kjær, *Microphone handbook: Part I* (1995).

[4] G. S. Wong, *Microphones and Their Calibration*, 1061–1091 (Springer New York, New York, NY).

[5] M. Brandstein and D. Ward, eds., *Microphone Arrays*, Digital Signal Processing (Springer Berlin Heidelberg, Berlin, Heidelberg, 2001).

[6] Y. Hiranaka, O. Nishii, T. Genma, and H. Yamasaki, "Real-time visualization of acoustic wave fronts by using a two-dimensional microphone array," J. Acoust. Soc. Am. **84**(4), 1373–1377 (1988).

[7] K. Ishikawa, K. Yatabe, N. Chitanont, Y. Ikeda, Y. Oikawa, T. Onuma, H. Niwa, and M. Yoshii, "High-speed imaging of sound using parallel phase-shifting interferometry," Opt. Express **24**(12), 12922–12932 (2016).

[8] K. Ishikawa, K. Yatabe, Y. Ikeda, Y. Oikawa, T. Onuma, H. Niwa, and M. Yoshii, "Optical sensing of sound fields: Non-contact, quantitative, and single-shot imaging of sound using high-speed polarization camera," in *Proc. 5th Joint Meet. Acoust. Soc. Am. Acoust. Soc. Jpn.*, Hawaii (2016), Vol. 140.

[9] K. Ishikawa, K. Yatabe, Y. Ikeda, Y. Oikawa, T. Onuma, H. Niwa, and M. Yoshii, "Interferometric imaging of acoustical phenomena using high-speed polarization camera and 4-step parallel phase-shifting technique," Proc. SPIE **10328**, 103280I (2017).

[10] K. Ishikawa, K. Yatabe, Y. Oikawa, T. Onuma, and H. Niwa, "Optical visualization of sound field inside transparent cavity using polarization high-speed camera," in *Proc. Inter-Noise*, Illinois (2018).

[11] K. Ishikawa, R. Tanigawa, K. Yatabe, Y. Oikawa, T. Onuma, and H. Niwa, "Simultaneous imaging of flow and sound using high-speed parallel phase-shifting interferometry," Opt. Lett. **43**(5), 991–994 (2018).

[12] K. Yatabe, R. Tanigawa, K. Ishikawa, and Y. Oikawa, "Time-directional filtering of wrapped phase for observing transient phenomena with parallel phase-shifting interferometry," Opt. Express **26**(11), 13705–13720 (2018).

[13] R. Tanigawa, K. Ishikawa, K. Yatabe, Y. Oikawa, T. Onuma, and H. Niwa, "Optical visualization of a fluid flow via the temperature controlling method," Opt. Lett. **43**(14), 3273–3276 (2018).

[14] A. Töpler, "Optische Studien nach der Methode der Schlierenbeobachtung," Annalen der Physik und Chemie **207**(5), 33–55 (1867).

[15] L. Brillouin, "Diffusion of light and X-rays by a transparent homogenous body: the influence of thermal agitation," Ann. Phys. **17**, 88–122 (1922).

[16] P. Debye and F. W. Sears, "On the scattering of light by supersonic waves," Proc. Natl. Acad. Sci. U.S.A. **18**(6), 409–414 (1932).

[17] R. Lucas and P. Biquard, "Optical properties of solid and liquid medias subjected to high-frequency elastic vibrations," J. de Physique **71**, 464–477 (1932).

[18] H. M. Colbert, "Light Diffraction by Ultrasonic Waves-Fresnel Region," J. Acoust. Soc. Am. **35**(3), 359–363 (1963).

[19] R. Adler, "Interaction between light and sound," IEEE Spectrum **4**(5), 42–54 (1967).

[20] A. Korpel, "Acousto-Optics: A Review of Fundamentals," Proc. IEEE **69**(1), 48–53 (1981).

[21] K. Negishi, "Ultrasonic light diffraction using a narrow light beam transition from diffraction to deflection," Jpn. J. Appl. Phys. **24**(S1), 15–17 (1985).

[22] K. Ishikawa, K. Yatabe, Y. Ikeda, and Y. Oikawa, "Numerical analysis of acousto-optic effect caused by audible sound based on geometrical optics," in *12th West. Pac. Acoust. Conf.* (2015), pp. 165–169.

[23] G. S. Settles, *Schlieren and Shadowgraph Techniques* (Springer Berlin Heidelberg, Berlin, Heidelberg, 2001).

[24] T. Pitts, R. Kinnick, and J. Greenleaf, "Optical measurement of wideband ultrasound fields via Gabor holography," in *Proc. IEEE Ultrason. Symp.*, IEEE (1997), Vol. 1, pp. 761–764.

[25] T. A. Pitts and J. F. Greenleaf, "Three-dimensional optical measurement of instantaneous pressure," J. Acoust. Soc. Am. **108**(6), 2873–2883 (2000).

[26] R. Omura, Y. Shimazaki, S. Yoshizawa, and S. Umemura, "Quantitative measurement of focused ultrasound pressure field using subtraction shadowgraph," Jpn. J. Appl. Phys. **50**(7 PART 2), 4–7 (2011).

[27] Y. Shimazaki, S. Harigane, S. Yoshizawa, and S. I. Umemura, "Three-dimensional quantitative optical measurement of asymmetrically focused ultrasound pressure field," Jpn. J. Appl. Phys. **51**(7 PART2), 3–7 (2012).

[28] R. Miyasaka, J. Yasuda, M. Syahid, S. Yoshizawa, and S. I. Umemura, "Quantitative measurement of focused ultrasound pressure field by background-subtracted shadowgraph using holographic diffuser as screen," Jpn. J. Appl. Phys. **53**(7), 07KF24 (2014).

[29] K. Imano, "Optical observation method for ultrasonic field using the shadowgraph introducing pulse inversion averaging," IEICE Electron. Express **11**(17), 1–6 (2014).

[30] K. Johansen, J. H. Song, and P. Prentice, "Characterising focused ultrasound via high speed shadowgraphic imaging at 10 million frames per second," in *IEEE Int. Ultrason. Symp. (IUS)* (2016), pp. 1–4.

[31] P. Yuldashev, S. Ollivier, M. Averiyanov, O. Sapozhnikov, V. Khokhlova, and P. Blanc-Benon, "Nonlinear propagation of spark-generated N-waves in air: modeling and measurements using acoustical and optical methods," J. Acoust. Soc. Am. **128**(6), 3321–3333 (2010).

[32] Y. Sonoda and M. Akazaki, "Measurement of low-frequency ultrasonic waves by fraunhofer diffraction," Jpn. J. Appl. Phys. **33**(5S), 3110–3114 (1994).

[33] T. Sakoda and Y. Sonoda, "Transmission and detection of light diffraction signal by low-frequency ultrasonic wave," Jpn. J. Appl. Phys. **42**(Part 1, 9A), 5821–5825 (2003).

[34] M. Kosaka, K. Seto, M. T. I. Khan, and Y. Nakazono, "Measurement of supersonic jet noise with optical wave microphone system," J. Therm. Sci. **14**(4), 352–356 (2005).

[35] T. Sakoda and Y. Sonoda, "Visualization of sound field with uniform phase distribution using laser beam microphone coupled with computerized tomography method," Acoust. Sci. Tech. **29**(4), 295–299 (2008).

[36] Y. Nakazono, S. Aoki, and S. Saguarum, "Near-Field Acoustic Characteristics of Underexpanded Jets from Notched Nozzles," J. Jpn. Soc. Exp. Mech. **11**, 47–52 (2011).

[37] Y. Sonoda and Y. Nakazono, "Development of optophone with no diaphragm and application to sound measurement in jet flow," Adv. Acoust. Vib. **2012**, 1–17 (2012).

[38] T. Kuroyama, K. Mizutani, N. Wakatsuki, and T. Ohbuchi, "Measurement of pressure amplitude of ultrasonic standing wave based on method of obtaining optical wavefront using phase retrieval," Jpn. J. Appl. Phys. **53**, 07KE12 (2014).

[39] R. B. Barnes and C. J. Burton, "Visual methods for studying ultrasonic phenomena," J. Appl. Phys. **20**(3), 286–294 (1949).

[40] J. A. Bucaro, "Sensitivity of the schlieren method for the visualization of low-frequency ultrasonic waves," J. Acoust. Soc. Am. **63**(3), 768–773 (1978).

[41] B. Porter, "Quantitative real-time schlieren system for ultrasound visualization," Rev. Sci. Instrum. **55**(2), 216–221 (1984).

[42] A. Hanafy and C. I. Zanelli, "Quantitative real-time pulsed Schlieren imaging of ultrasonic waves," in *Ultrason. Symp.* (1991), pp. 1223–1228.

[43] T. Charlebois and R. Pelton, "Quantitative 2D and 3D Schlieren imaging for acoustic power and intensity measurements," Med. Electron. 789–792 (1995).

[44] P. Krehl and S. Engemann, "August Toepler - The first who visualized shock waves," Shock Waves **5**(1-2), 1–18 (1995).

[45] P. Kwiek, W. Molkenstruck, and R. Reibold, "Optical mapping of ultrasonic fields in the intermediate range between weak and strong acousto-optical interaction," Ultrasonics **35**(7), 499–507 (1997).

[46] T. Azuma, A. Tomozawa, and S. I. Umemura, "Observation of ultrasonic wavefronts by synchronous Schlieren imaging," Jpn. J. Appl. Phys. **41**(Part 1, 5B), 3308–3312 (2002).

[47] N. Kudo, H. Ouchi, K. Yamamoto, and H. Sekimizu, "A simple Schlieren system for visualizing a sound field of pulsed ultrasound," J. Phys.: Conf. Series **1**, 146–149 (2004).

[48] T. Neumann and H. Ermert, "Schlieren visualization of ultrasonic wave fields with high spatial resolution," Ultrasonics **44**, 1561–1566 (2006).

[49] C. Unverzagt, S. Olfert, and B. Henning, "A new method of spatial filtering for Schlieren visualization of ultrasound wave fields," Phys. Procedia **3**(1), 935–942 (2010).

[50] G. Caliano, A. Savoia, and A. Iula, "An automatic compact Schlieren imaging system for ultrasound transducer testing," IEEE Trans. Ultrason., Ferroelectr., and Freq. Control **59**(9), 2102–2110 (2012).

[51] Z. Xu, H. Chen, X. Yan, M. Qian, and Q. Cheng, "Quantitative calibration of sound pressure in ultrasonic standing waves using the Schlieren method," Opt. Express **25**(17), 20401–20409 (2017).

[52] A. Pulkkinen, J. J. Leskinen, and A. Tiihonen, "Ultrasound field characterization using synthetic schlieren tomography," J. Acoust. Soc. Am. **141**(6), 4600–4609 (2017).

[53] Z. Xu, H. Chen, X. Yan, M.-L. Qian, and Q. Cheng, "Three-dimensional reconstruction of nonplanar ultrasound fields using Radon transform and the schlieren imaging method," J. Acoust. Soc. Am. **142**(1), EL82–EL88 (2017).

[54] J. A. Bucaro, "Visualization of ultrasonic waves in air," J. Acoust. Soc. Am. **62**(6), 1506–1507 (1977).

[55] M. J. Hargather, G. S. Settles, and M. J. Madalis, "Schlieren imaging of loud sounds and weak shock waves in air near the limit of visibility," Shock Waves **20**(1), 9–17 (2010).

[56] N. Chitanont, K. Yaginuma, K. Yatabe, and Y. Oikawa, "Visualization of sound field by means of Schlieren method with spatio-temporal filtering," in *IEEE Int. Conf. Acoust., Speech Signal Process.* (2015), pp. 509–513.

[57] N. Chitanont, K. Yatabe, K. Ishikawa, and Y. Oikawa, "Spatio-temporal filter bank for visualizing audible sound field by Schlieren method," Appl. Acoust. **115**, 109–120 (2017).

[58] N. Chitanont, "Spatio-temporal filtering for visualizing audible sound field by schlieren method," Ph.D. thesis, Waseda University, Tokyo, Japan, 2017.

[59] A. Hirschberg, J. Gilbert, R. Msallam, and A. P. J. Wijnands, "Shock waves in trombones," J. Acoust. Soc. Am. **99**(3), 1754–1758 (1996).

[60] B. H. Pandya, G. S. Settles, and J. D. Miller, "Schlieren imaging of shock waves from a trumpet," J. Acoust. Soc. Am. **114**(6 Pt 1), 3363–3367 (2003).

[61] P. L. Rendón, R. Velasco-Segura, C. Echeverría, D. Porta, A. Pérez-López, R. T. Vázquez-Turner, and C. Stern, "Using Schlieren imaging to estimate the geometry of a shock wave radiated by a trumpet bell," J. Acoust. Soc. Am. **144**(4), EL310–EL314 (2018).

[62] M. M. Karzova, P. V. Yuldashev, V. A. Khokhlova, S. Ollivier, E. Salze, and P. Blanc-Benon, "Characterization of spark-generated N-waves in air using an optical schlieren method," J. Acoust. Soc. Am. **137**(6), 3244–3252 (2015).

[63] Q. Song, C. Moreno, F. Liu, and L. Cattafesta, "Quantitative schlieren measurements in a normal incidence acoustic impedance tube," Eur. Phys. J.: Special Topics **182**(1), 113–124 (2010).

[64] F. Zernike, "Phase contrast, a new method for the microscopic observation of transparent objects," Physica **9**(7), 686–698 (1942).

[65] F. Zernike, "Phase contrast, a new method for the microscopic observation of transparent objects part II," Physica **9**(10), 974–986 (1942).

[66] T. A. Pitts, A. Sagers, and J. F. Greenleaf, "Optical phase contrast measurement of ultrasonic fields," IEEE Trans. Ultrason., Ferroelectr., Freq. Control **48**(6), 1686–1694 (2001).

[67] T. A. Pitts and J. F. Greenleaf, "Optical measurement of ultrasonic Poynting and velocity vector fields," IEEE Trans. Ultrason., Ferroelectr., Freq. Control **49**(2), 193–203 (2002).

[68] E. K. Reichel and B. G. Zagar, "Phase contrast method for measuring ultrasonic fields," IEEE Trans. Instrum. Meas. **55**(4), 1356–1361 (2006).

[69] S. Harigane, R. Miyasaka, S. Yoshizawa, and S. Umemura, "Optical phase contrast mapping of highly focused ultrasonic fields," Jpn. J. Appl. Phys. **52**(7 PART 2), 07HF07 (2013).

[70] M. Syahid, S. Oyama, J. Yasuda, S. Yoshizawa, and S. Umemura, "Quantitative measurement of high intensity focused ultrasound pressure field by optical phase contrast method applying non-continuous phase unwrapping algorithm," Jpn. J. Appl. Phys. **54**(7), 07HC09 (2015).

[71] S. Oyama, J. Yasuda, H. Hanayama, S. Yoshizawa, and S. Umemura, "Quantitative measurement of ultrasound pressure field by optical phase contrast method and acoustic holography," Jpn. J. Appl. Phys. **55**(7), 07KB09 (2016).

[72] T. Nakamura, R. Iwasaki, S. Yoshizawa, and S. Umemura, "Quantitative measurement of ultrasonic pressure field using combination of optical phase contrast and nonlinear acoustic holography methods," Jpn. J. Appl. Phys. **57**(7S1), 07LB13 (2018).

[73] T. H. Maiman, "Stimulated Optical Radiation in Ruby," Nature **187**(4736), 493–494 (1960).

[74] C. H. Palmer, H. M. South, and T. H. Mak, "Optical interferometry for measurement of Rayleigh and dilatational waves," Ultrasonics **12**(3), 106–108 (1974).

[75] G. Smeets, "Laser interference microphone for ultrasonics and nonlinear acoustics," J. Acoust. Soc. Am. **61**(3), 872–875 (1977).

[76] J. A. Clark, "Moire processing of acoustic field holograms," Opt. Commun. **25**(2), 157–162 (1978).

[77] J. A. Clark, "Holographic visualization of acoustic fields," J. Sound Vib. **56**(2), 167–174 (1978).

[78] J. A. Clark, "Visual characteristics acoustic of waves," J. Sound Vib. **70**(2), 267–273 (1980).

[79] K. Mizutani, M. Nemoto, T. Ezure, and H. Masuyama, "Visualization of ultrasonic beam using Michelson interferometer," Jpn. J. Appl. Phys. **42**(5B), 3072–3075 (2003).

[80] T. Ezure, K. Mizutani, and H. Masuyama, "Optical measurement of sound fields estimated from multiple interference images using Mach-Zehnder interferometer," Electron. Commun. Jpn., Part II: Electron. (English translation of Denshi Tsushin Gakkai Ronbunshi) **87**(11), 20–27 (2004).

[81] T. Obuchi, H. Masuyama, K. Mizutani, and S. Nakanishi, "Optical computerized tomography for visualization of ultrasonic fields using michelson interferometer," Jpn. J. Appl. Phys. **45**(9A), 7152–7157 (2006).

[82] T. Ohbuchi, K. Mizutani, N. Wakatsuki, and H. Masuyama, "Determination of Sound Velocity in Three-Dimensional Space by Optical Probe," Jpn. J. Appl. Phys. **47**(5), 3959–3961 (2008).

[83] T. Ohbuchi, K. Mizutani, N. Wakatsuki, K. Nishimiya, and H. Masuyama, "Reconstruction of three-dimensional sound field from two-dimensional sound field using optical computerized tomography and near-field acoustical holography," Jpn. J. Appl. Phys. **48**(7 PART 2), 07GC03 (2009).

[84] P. Yuldashev, M. Karzova, V. Khokhlova, S. Ollivier, and P. Blanc-Benon, "Mach-Zehnder interferometry method for acoustic shock wave measurements in air and broadband calibration of microphones," J. Acoust. Soc. Am. **137**(6), 3314–3324 (2015).

[85] K. Bertling, J. Perchoux, T. Taimre, R. Malkin, D. Robert, A. D. Rakić, and T. Bosch, "Imaging of acoustic fields using optical feedback interferometry," Opt. Express **22**(24), 30346–30356 (2014).

[86] X. Jia, G. Quentin, M. Lassoued, and J. Berger, "Quantitative measurement of ultrasonic pressures with an optical heterodyne interferometer," in *Proc. IEEE Ultrason. Symp.* (1991), pp. 1137–1140.

[87] X. Jia, G. Quentin, and M. Lassoued, "Optical heterodyne detection of pulsed ultrasonic pressures," IEEE Trans. Ultrason., Ferroelectr., Freq. Control **40**(1), 67–69 (1993).

[88] O. Bou Matar, L. Pizarro, D. Certon, J. P. Remenieras, and F. Patat, "Characterization of airborne transducers by optical tomography," Ultrasonics **38**(1), 787–793 (2000).

[89] L. Zipser and S. Lindner, "Visualisation of vortexes and acoustic sound waves," in *17th Int. Congr. Acoust.* (2001).

[90] A. Harland, J. Petzing, and J. Tyrer, "Non-Invasive measurements of underwater pressure fields using laser Doppler velocimetry," J. Sound Vib. **252**(1), 169–177 (2002).

[91] K. Nakamura, M. Hirayama, and S. Ueha, "Measurements of air-borne ultrasound by detecting the modulation in optical refractive index of air," Proc. IEEE Ultrason. Symp. **1**(c), 609–612 (2002).

[92] K. Nakamura, M. Hirayama, and S. Ueha, "Highly directive measurements of air-borne ultrasound by detecting the optical refractive index of air," in *Proc. World Congr. Ultrason.* (2003), pp. 581–584.

[93] A. R. Harland, J. N. Petzing, J. R. Tyrer, C. J. Bickley, S. P. Robinson, and R. C. Preston, "Application and assessment of laser Doppler velocimetry for underwater acoustic measurements," J. Sound Vib. **265**(3), 627–645 (2003).

[94] L. Zipser, H. Franke, E. Olsson, N.-E. Molin, and M. Sjödahl, "Reconstructing two-dimensional acoustic object fields by use of digital phase conjugation of scanning laser vibrometry recordings," Appl. Opt. **42**(29), 5831–5838 (2003).

[95] Y. Wang, P. Theobald, J. Tyrer, and P. Lepper, "The application of scanning vibrometer in mapping ultrasound fields," J. Phys.: Conf. Series **1**, 167–173 (2004).

[96] L. Zipser and H. Franke, "Laser-scanning vibrometry for ultrasonic transducer development," Sens. Actuators A Phys. **110**(1-3), 264–268 (2004).

[97] J. M. Buick, J. A. Cosgrove, P. A. Douissard, C. A. Greated, and B. Gilabert, "Application of the acousto-optic effect to pressure measurements in ultrasound fields in water using a laser vibrometer," Rev. Sci. Instrum. **75**(10 I), 3203–3207 (2004).

[98] G. Harvey, A. Gachagan, and A. McNab, "Ultrasonic field measurement in test cells combining the acousto-optic effect, laser interferometry & tomography," Proc. IEEE Ultrason. Symp. **2**(c), 1038–1041 (2004).

[99] A. R. Harland, J. N. Petzing, and J. R. Tyrer, "Nonperturbing measurements of spatially distributed underwater acoustic fields using a scanning laser Doppler vibrometer," J. Acoust. Soc. Am. **115**(1), 187–195 (2004).

[100] Y. Oikawa, Y. Ikeda, M. Goto, T. Takizawa, and Y. Yamasaki, "Sound field measurements based on reconstruction from laser projections," in *Proc. IEEE Int. Conf. Acoust., Speech, Signal Process.* (2005), pp. 661–664.

[101] S. Vanlanduit, J. Vanherzeele, P. Guillaume, and G. De Sitter, "Absorption measurement of acoustic materials using a scanning laser Doppler vibrometer," J. Acousto. Soc. Am. **117**(3), 1168–1172 (2005).

[102] S. Frank and J. Schell, "Sound field simulation and visualisation based on laser Doppler vibrometer measurements," Forum Acousticum (1), 91–97 (2005).

[103] G. Harvey and A. Gachagan, "Noninvasive field measurement of low-frequency ultrasonic transducers operating in sealed vessels," IEEE Trans. Ultrason., Ferroelectr., Freq. Control **53**(10), 1749–1758 (2006).

[104] E. Olsson, "Locating primary sound sources in scattering media using multifrequency digital holographic reconstruction," Opt. Eng. **45**(1), 015801 (2006).

[105] P. Gren, K. Tatar, J. Granström, N.-E. Molin, and E. V. Jansson, "Laser vibrometry measurements of vibration and sound fields of a bowed violin," Meas. Sci. Tech. **17**(4), 635–644 (2006).

[106] E. Olsson and K. Tatar, "Sound field determination and projection effects using laser vibrometry," Meas. Sci. Tech. **17**(10), 2843–2851 (2006).

[107] K. Tatar, E. Olsson, and F. Forsberg, "Tomographic reconstruction of 3D ultrasound fields measured using laser vibrometry," 13th Int. Conf. Exp. Mech. (ICEM13) 337–338 (2007).

[108] A. R. Harland, J. N. Petzing, and J. R. Tyrer, "Visualising scattering underwater acoustic fields using laser Doppler vibrometry," J. Sound Vib. **305**(4-5), 659–671 (2007).

[109] E. Olsson, "Selective imaging of sound sources in air using phase-calibrated multiwavelength digital holographic reconstructions," Opt. Eng. **46**(7), 075801 (2007).

[110] J. Vanherzeele, S. Vanlanduit, and P. Guillaume, "Acoustic source identification using a scanning laser Doppler vibrometer," Opt. Lasers Eng. **45**(6), 742–749 (2007).

[111] L. Zipser and H. H. Franke, "Refracto-vibrometry - a novel method for visualizing sound waves in transparent media," in *Acoustics* (2008), pp. 1997–2001.

[112] L. Bahr and R. Lerch, "Sound pressure measurement utilizing light refractive tomography," Proc. IEEE Ultrason. Symp. 840–843 (2008).

[113] L. Bahr and R. Lerch, "Beam profile measurements using light refractive tomography," IEEE Trans. Ultrason., Ferroelectr., Freq. Control **55**(2), 405–413 (2008).

[114] C. Vuye, S. Vanlanduit, and P. Guillaume, "Accurate estimation of normal incidence absorption coefficients with confidence intervals using a scanning laser Doppler vibrometer," Opt. Lasers Eng. **47**(6), 644–650 (2009).

[115] E. Olsson and F. Forsberg, "Three-dimensional selective imaging of sound sources," Opt. Eng. **48**, 035801 (2009).

[116] Y. Oikawa, T. Hasegawa, Y. Ouchi, Y. Yamasaki, and Y. Ikeda, "Visualization of sound field and sound source vibration using laser measurement method," in *20th Int. Congr. Acoust.* (2010), pp. 1–5.

[117] A. T. Rosell, "Sound field reconstruction based on the acousto-optic effect," in *Proc. Inter-Noise* (2011), pp. 1–6.

[118] L. Chen, S. J. Rupitsch, and R. Lerch, "A reliability study of light refractive tomography utilized for noninvasive measurement of ultrasound pressure fields," IEEE Trans. Ultrason., Ferroelectr., Freq. Control **59**(5), 915–927 (2012).

[119] A. Torras-Rosell, S. Barrera-Figueroa, and F. Jacobsen, "Sound field reconstruction using acousto-optic tomography," J. Acoust. Soc. Am. **131**(5), 3786–3793 (2012).

[120] A. Torras-Rosell, S. Barrera-Figueroa, and F. Jacobsen, "An acousto-optic beamformer," J. Acoust. Soc. Am. **132**(1), 144–149 (2012).

[121] A. Torras-Rosell and S. Barrera-figueroa, "A beamforming system based on the acousto-optic effect," (2012), pp. 1048–1053.

[122] A. Torras-Rosell, O. Lylloff, S. Barrera-figueroa, and F. Jacobsen, "Reconstruction methods for sound visualization based on acousto-optic tomography," in *Proc. Inter-Noise* (2013), pp. 1–9.

[123] M. Martarelli, P. Castellini, and E. P. Tomasini, "Subsonic jet pressure fluctuation characterization by tomographic laser interferometry," Exp. Fluids **54**(12), 1626 (2013).

[124] E. Fernandez-Grande, A. Torras-Rosell, and F. Jacobsen, "Holographic reconstruction of sound fields based on the acousto-optic effect," in *Proc. Inter-Noise* (2013), pp. 3407–3416.

[125] K. Yatabe and Y. Oikawa, "PDE-based interpolation method for optically visualized sound field," in *Proc. IEEE Int. Conf. Acoust., Speech, Signal Process.* (2014), pp. 4738–4742.

[126] R. Malkin, T. Todd, and D. Robert, "A simple method for quantitative imaging of 2D acoustic fields using refracto-vibrometry," J. Sound Vib. **333**(19), 4473–4482 (2014).

[127] A. Torras-rosell and S. Barrera-figueroa, "An Acousto-Optic Method for Free-Field Microphone Calibration," in *Int. Congr. Sound Vib.* (2015), pp. 12–16.

[128] R. Malkin, T. Todd, and D. Robert, "Quantitative imaging of acoustic reflection and interference," J. Phys.: Conf. Series **581**, 012007 (2015).

[129] K. Yatabe and Y. Oikawa, "Optically visualized sound field reconstruction based on sparse selection of point sound sources," in *Proc. IEEE Int. Conf. Acoust., Speech, Signal Process.* (2015), pp. 504–508.

[130] Y. Ikeda, N. Okamoto, T. Konishi, Y. Oikawa, Y. Tokita, and Y. Yamasaki, "Observation of traveling wave with laser tomography," Acoust. Sci. Tech. **37**(5), 231–238 (2016).

[131] N. R. Huber, T. M. Huber, and M. T. Huber, "Optical imaging of propagating Mach cones in water using refracto-vibrometry," J. Acoust. Soc. Am. **141**(3), EL239–EL242 (2017).

[132] R. Jackett, B. Piper, and R. J. Hughes, "Characterization of acoustic diffusion using refracto-vibrometry," J. Sound Vib. **392**, 70–76 (2017).

[133] K. Yatabe, K. Ishikawa, and Y. Oikawa, "Acousto-optic back-projection: Physical-model-based sound field reconstruction from optical projections," J. Sound Vib. **394**, 171–184 (2017).

[134] S. Hisada, T. Suzuki, S. Nakahara, and T. Fujita, "Visualization and measurements of sound pressure distribution of ultrasonic wave by stroboscopic real-time holographic interferometry," Jpn. J. Appl. Phys. **41**(Part 1, No. 5B), 3316–3324 (2002).

[135] P. Zheng, E. Li, J. Zhao, J. Di, W. Zhou, H. Wang, and R. Zhang, "Visualized measurement of the acoustic levitation field based on digital holography with phase multiplication," Opt. Commun. **282**(22), 4339–4344 (2009).

[136] O. Matoba, H. Inokuchi, K. Nitta, and Y. Awatsuji, "Optical voice recorder by off-axis digital holography," Opt. Lett. **39**(22), 6549–6552 (2014).

[137] S. K. Rajput and O. Matoba, "Optical voice encryption based on digital holography," Opt. Lett. **42**(22), 4619–4622 (2017).

[138] S. K. Rajput, O. Matoba, and Y. Awatsuji, "Characteristics of vibration frequency measurement based on sound field imaging by digital holography," OSA Continuum **1**(1), 200–212 (2018).

[139] O. J. Lokberg, "Recording of sound emission and propagation in air using TV holography," J. Acoust. Soc. Am. **96**(4), 2244–2250 (1994).

[140] O. J. Lokberg, "Sound in flight: measurement of sound fields by use of TV holography," Appl. Opt. **33**(13), 2574–2584 (1994).

[141] M. Espeland, O. J. Lokberg, and R. Rustad, "Full field tomographic reconstruction of sound fields using TV holography," J. Acoust. Soc. Am. **98**(1), 280–287 (1995).

[142] O. J. Lokberg, M. Espeland, and H. M. Pedersen, "Tomographic reconstruction of sound fields using TV holography," Appl. Opt. **34**(10), 1640–1645 (1995).

[143] R. Rustad, O. J. Lokberg, H. M. Pedersen, K. Klepsvik, and T. Storen, "TV holography measurements of underwater acoustic fields," J. Acoust. Soc. Am. **102**(3), 1904–1906 (1997).

[144] R. Rustad, "Acoustic field of a medical ultrasound probe operated in continuous-wave mode investigated by TV holography," Appl. Opt. **37**(31), 7368–7377 (1998).

[145] R. Rustad and L. H. Morset, "Investigation of the near field of a loudspeaker using tomographic reconstruction from TV-holography measurements," J. Acoust. Soc. Am. **104**(3), 1503–1508 (1998).

[146] P. Gren, S. Schedin, and X. Li, "Tomographic reconstruction of transient acoustic fields recorded by pulsed TV holography," Appl. Opt. **37**(5), 834–840 (1998).

[147] A. Runnemalm, "Standing waves in a rectangular sound box recorded by TV holography," J. Sound Vib. **224**(4), 689–707 (1999).

[148] H. Joost and K. D. Hinsch, "Sound field monitoring by tomographic electronic speckle pattern interferometry," Opt. Commun. **259**(2), 492–498 (2006).

[149] F. Souris, J. Grucker, P. Jacquier, J. Dupont-Roc, A. Arvengas, and F. Caupin, "Time-resolved quantitative multiphase interferometric imaging of a highly focused ultrasound pulse," Appl. Opt. **49**(31), 6127–6133 (2010).

[150] A. O. Wåhlin, P. O. Gren, and N. Molin, "On structure-borne sound: Experiments showing the initial transient acoustic wave field generated by an impacted plate," J. Acoust. Soc. Am. **96**, 2791–2797 (1994).

[151] S. Schedin, P. O. Gren, and A. O. Wa, "Transient acoustic near field in air generated by impacted plates," J. Acoust. Soc. Am. **99**(2), 700–705 (1996).

[152] S. Schedin, C. Lambourg, and A. Chaigne, "Transient sound fields from impacted plates: comparison between numerical simulations and experiments," J. Sound Vib. **221**(3), 471–490 (1999).

[153] H. Sobral, M. Villagrán-Muniz, R. Navarro-González, and A. C. Raga, "Temporal evolution of the shock wave and hot core air in laser induced plasma," Appl. Phys. Lett. **77**(20), 3158–3160 (2000).

[154] Q. Qin and K. Attenborough, "Characteristics and application of laser-generated acoustic shock waves in air," Appl. Acoust. **65**(4), 325–340 (2004).

[155] N. Hosoya, M. Nagata, and I. Kajiwara, "Acoustic testing in a very small space based on a point sound source generated by laser-induced breakdown: Stabilization of plasma formation," J. Sound Vib. **332**(19), 4572–4583 (2013).

[156] J. Gómez Bolaños, V. Pulkki, P. Karppinen, and E. Hæggström, "An optoacoustic point source for acoustic scale model measurements," J. Acoust. Soc. Am. **133**(4), EL221–EL227 (2013).

[157] J. Gómez Bolaños, S. Delikaris-Manias, V. Pulkki, J. Eskelinen, and E. Hæggström, "Laser-induced acoustic point source for accurate impulse response measurements within the audible bandwidth," J. Acoust. Soc. Am. **135**(6), EL298–EL303 (2014).

[158] A. Torras-rosell, "New measurement techniques optical methods for characterizing sound fields," Ph.D. thesis, Technical University of Denmark, Kongens Lyngby, Denmark, 2014.

[159] H. Schreiber and J. H. Bruning, "Phase Shifting Interferometry," in *Optical Shop Testing* (John Wiley & Sons, Inc., Hoboken, NJ, USA, 2006), pp. 547–666.

[160] G. Lai and T. Yatagai, "Generalized phase-shifting interferometry," J. Opt. Soc. Am. A **8**(5), 822–827 (1991).

[161] M. Servin, J. C. Estrada, and J. A. Quiroga, "The general theory of phase shifting algorithms," Opt. Express **17**(24), 21867–21881 (2009).

[162] K. Yatabe, K. Ishikawa, and Y. Oikawa, "Improving principal component analysis based phase extraction method for phase-shifting interferometry by integrating spatial information," Opt. Express **24**(20), 22881–22891 (2016).

[163] K. Yatabe, K. Ishikawa, and Y. Oikawa, "Simple, flexible, and accurate phase retrieval method for generalized phase-shifting interferometry," J. Opt. Soc. Am. A **34**(1), 87–96 (2016).

[164] K. Yatabe, K. Ishikawa, and Y. Oikawa, "Hyper ellipse fitting in subspace method for phase-shifting interferometry: practical implementation with automatic pixel selection," Opt. Express **25**(23), 29401–29416 (2017).

[165] T. Yatagai, B. J. Jackin, A. Ono, K. Kiyohara, M. Noguchi, M. Yoshii, M. Kiyohara, H. Niwa, K. Ikuo, and T. Onuma, "Instantaneous phase-shifting fizeau interferometry with high-speed pixelated phase-mask camera," in *SPECKLE 2015: VI Int. Conf. .Speckle Metrol.*, edited by F. M. Santoyo and E. R. Mendez, SPIE (2015).

[166] T. Onuma and Y. Otani, "A development of two-dimensional birefringence distribution measurement system with a sampling rate of 1.3 MHz," Opt. Commun. **315**, 69–73 (2014).

[167] Y. Awatsuji, M. Sasada, and T. Kubota, "Parallel quasi-phase-shifting digital holography," Appl. Phys. Lett. **85**(6), 1069–1071 (2004).

[168] J. E. Millerd, N. J. Brock, J. B. Hayes, M. B. North-Morris, M. Novak, and J. C. Wyant, "Pixelated phase-mask dynamic interferometer," Proc. SPIE **5531**(520), 304–314 (2004).

[169] E. Collett, *Field Guide to Polarization* (SPIE, 2005).

[170] P. E. Ciddor, "Refractive index of air: new equations for the visible and near infrared," Appl. Opt. **35**(9), 1566–1573 (1996).

[171] J. Kuroda and Y. Oikawa, "Piezoelectric transducer with resonant modes control for parametric speaker," Acoust. Sci. Tech. **39**(1), 1–10 (2018).

[172] T. Kakue, Y. Endo, T. Nishitsuji, T. Shimobaba, N. Masuda, and T. Ito, "Digital holographic high-speed 3D imaging for the vibrometry of fast-occurring phenomena," Sci. Rep. **7**(1), 10413 (2017).

[173] M. Ney, A. Safrani, and I. Abdulhlaim, "Instantaneous high-resolution focus tracking and a vibrometery system using parallel phase shift interferometry," J. Opt. **18**(9), 09LT02 (2016).

[174] M. Ney, A. Safrani, and I. Abdulhalim, "Three wavelengths parallel phase-shift interferometry for real-time focus tracking and vibration measurement," Opt. Lett. **42**(4), 719–722 (2017).

[175] T. Kakue, R. Yonesaka, T. Tahara, Y. Awatsuji, K. Nishio, S. Ura, T. Kubota, and O. Matoba, "High-speed phase imaging by parallel phase-shifting digital holography," Opt. Lett. **36**(21), 4131–4133 (2011).

[176] T. Fukuda, Y. Wang, P. Xia, Y. Awatsuji, T. Kakue, K. Nishio, and O. Matoba, "Three-dimensional imaging of distribution of refractive index by parallel phase-shifting digital holography using abel inversion," Opt. Express **25**(15), 18066–18071 (2017).

[177] P. Xia, Y. Awatsuji, K. Nishio, and O. Matoba, "One million fps digital holography," Electron. Lett. **50**(23), 1693–1695 (2014).

[178] T. Tahara, K. Ito, T. Kakue, M. Fujii, Y. Shimozato, Y. Awatsuji, K. Nishio, S. Ura, T. Kubota, and O. Matoba, "Parallel phase-shifting digital holographic microscopy," Biomed. Opt. Express **1**(2), 610–616 (2010).

[179] A. Safrani and I. Abdulhalim, "Full-field parallel interferometry coherence probe microscope for high-speed optical metrology," Appl. Opt. **54**(16), 5083–5086 (2015).

[180] A. Safrani and I. Abdulhalim, "High-speed 3D imaging using two-wavelength parallel-phase-shift interferometry," Opt. Lett. **40**(20), 4651–4654 (2015).

[181] M. J. Lighthill, "On sound generated aerodynamically I. General theory," Proc. R. Soc. London A **211**(1107), 564–587 (1952).

[182] P. J. Morris and G. M. Lilley, *Aerodynamic noise: theory and applications*, 128–158 (John Wiley & Sons, Inc.).

[183] C. Talotte, "Aerodynamic noise: a critical survey," J. Sound Vib. **231**(3), 549–562 (2000).

[184] S. Wagner, R. Bareiß, and G. Guidati, *Wind Turbine Noise* (Springer Berlin Heidelberg, Berlin, Heidelberg, 1996).

[185] C. E. Willert and M. Gharib, "Digital particle image velocimetry," Exp. Fluids **10**(4), 181–193 (1991).

[186] R. J. Adrian, "Twenty years of particle image velocimetry," Exp. Fluids **39**(2), 159–169 (2005).

[187] R. J. Adrian and J. Westerweel, *Particle image velocimetry* (Cambridge University Press, 2011).

[188] D. R. Jonassen, G. S. Settles, and M. D. Tronosky, "Schlieren PIV for turbulent flows," Opt. Laser Eng. **44**(3), 190–207 (2006).

[189] M. Raffel, "Background-oriented Schlieren (BOS) techniques," Exp. Fluids **56**(3), 1–17 (2015).

[190] J. Panda, "An experimental investigation of screech noise generation," J. Fluid Mech. **378**, 71–96 (1999).

[191] J. I. Hileman, B. S. Thurow, E. J. Caraballo, and M. Samimy, "Large-scale structure evolution and sound emission in high-speed jets: real-time visualization with simultaneous acoustic measurements," J. Fluid Mech. **544**(1), 277–307 (2005).

[192] A. Henning, K. Kaepernick, K. Ehrenfried, L. Koop, and A. Dillmann, "Investigation of aeroacoustic noise generation by simultaneous particle image velocimetry and microphone measurements," Exp. Fluids **45**(6), 1073–1085 (2008).

[193] Y. Nakazono, Y. Sonoda, Y. Ouchi, and Y. Nasu, "Near-field acoustic characteristics of screech jet exhausted from a nozzle with a hard reflecting plate," J. Vis. **11**(2), 153–162 (2008).

[194] G. Raman, "Cessation of screech in underexpanded jets," J. Fluid Mech. **336**, 69–90 (1997).

[195] G. Raman, "Supersonic jet screech: half-century from powell to the present," J. Sound Vib. **225**(3), 543–571 (1999).

[196] J. W. Coltman, "Acoustics of the flute," Phys. Today **21**(11), 25–32 (1968).

[197] M. S. Howe, "Contributions to the theory of aerodynamic sound, with application to excess jet noise and the theory of the flute," J. Fluid Mech. **71**(4), 625–673 (1975).

[198] D. Watt and C. Vest, "Digital interferometry for flow visualization," Exp. Fluids **5**(6), 401–406 (1987).

[199] N. Andrés, P. Arroyo, and M. Quintanilla, "Velocity measurements in a convective flow by holographic interferometry," Appl. Opt. **36**(27), 6997–7007 (1997).

[200] W. Sun, J. Zhao, J. Di, Q. Wang, and L. Wang, "Real-time visualization of karman vortex street in water flow field by using digital holography," Opt. Express **17**(22), 20342–20348 (2009).

[201] D. Watt and C. Vest, "Turbulent flow visualization by interferometric integral imaging and computed tomography," Exp. Fluids **8**(6), 301–311 (1990).

[202] T. Koukoulas and B. Piper, "Towards direct realisation of the SI unit of sound pressure in the audible hearing range based on optical free-field acoustic particle measurements," Appl. Phys. Lett. **106**(16), 164101 (2015).

[203] B. Piper and T. Koukoulas, "Sensing sound pressure in an anechoic chamber using backscattered laser light," Acta Physica Polonica A **127**(1), 128–131 (2015).

[204] J. Sharpe, T. Koukoulas, B. Piper, N. Sungar, and J. Tompkins, "Impact of tracer particle size on optical measurement of sound fields," Appl. Acoust. **120**, 54–58 (2017).

[205] E. G. Williams, "Chapter 6 - spherical waves," in *Fourier Acoustics*, edited by E. G. Williams (Academic Press, London, 1999), pp. 183–234.

[206] B. Kimbrough, "Correction of Errors in Polarization Based Dynamic Phase Shifting Interferometers," Int. J. Optomechatroni. **8**(4), 304–312 (2014).

[207] P. C. Hansen, J. G. Nagy, and D. P. O'Leary, *Deblurring Images: Matrices, Spectra, and Filtering* (Soc. Ind. Appl. Math., Philadelphia, PA, USA, 2006).

[208] K. Yatabe, K. Ishikawa, and Y. Oikawa, "Compensation of fringe distortion for phase-shifting three-dimensional shape measurement by inverse map estimation," Appl. Opt. **55**(22), 6017–6024 (2016).

[209] K. Yatabe and Y. Oikawa, "Convex optimization-based windowed fourier filtering with multiple windows for wrapped-phase denoising," Appl. Opt. **55**(17), 4632–4641 (2016).

Publications

Journal

1. ◯K. Ishikawa, R. Tanigawa, K. Yatabe, Y. Oikawa, T. Onuma, and H. Niwa, "Simultaneous imaging of flow and sound using high-speed parallel phase-shifting interferometry," Optics Letters, vol. 43, no. 5, pp. 991–994, 2018.

2. ◯K. Ishikawa, K. Yatabe, N. Chitanont, Y. Ikeda, Y. Oikawa, T. Onuma, H. Niwa, and M. Yoshii, "High-speed imaging of sound using parallel phase-shifting interferometry," Optics Express, vol. 24, no. 12, pp. 12922–12932, 2016.

3. R. Tanigawa, K. Ishikawa, K. Yatabe, and Y. Oikawa, T. Onuma, and H. Niwa, "Optical visualization of a fluid flow via the temperature controlling method," Optics Letters, vol. 43, no. 14, pp. 3273–3276, 2018.

4. K. Yatabe, R. Tanigawa, K. Ishikawa, and Y. Oikawa, "Time-directional filtering of wrapped phase for observing transient phenomena with parallel phase-shifting interferometry," Optics Express, vol. 26, no. 11, pp. 13705–13720, 2018.

5. K. Yatabe, K. Ishikawa, and Y. Oikawa, "Hyper ellipse fitting in subspace method for phase-shifting interferometry: Practical implementation with automatic pixel selection," Optics Express, vol. 25, no. 23, pp. 29401–29416, 2017.

6. K. Yatabe, K. Ishikawa, and Y. Oikawa, "Acousto-optic back-projection: Physical-model-based sound field reconstruction from optical projections," Journal of Sound and Vibration, vol. 394, pp.171–184, 2017.

7. K. Yatabe, K. Ishikawa, and Y. Oikawa, "Simple, flexible and accurate phase retrieval method for generalized phase-shifting interferometry," Journal of Optical Society of America A, vol. 34, no. 1, pp. 87–96, 2017.

8. N. Chitanont, K. Yatabe, K. Ishikawa, and Y. Oikawa, "Spatio-temporal lter bank for visualizing audible sound eld by Schlieren method," Appled. Acoustics, vol. 115, pp. 109–120, 2017.

9. K. Yatabe, K. Ishikawa, and Y. Oikawa, "Improving principal component analysis based phase extraction method for phase-shifting interferometry by integrating spatial information," Optics Express, vol. 24, no. 20, pp. 22881–22891, 2016.
10. K. Yatabe, K. Ishikawa, and Y. Oikawa, "Compensation of fringe distortion for phase-shifting 3D shape measurement by inverse map estimation," Applied Optics, vol. 55, no. 22, pp. 6017–6024, 2016.

International conference

1. ◯K. Ishikawa, K. Yatabe, Y. Oikawa, T. Onuma, and H. Niwa, "Optical visualization of sound field inside transparent cavity using polarization high-speed camera," 47th International Congress and Exposition on Noise Control Engineering (inter-noise), Illinois, Aug. 2018.
2. R. Tanigawa, K. Ishikawa, K. Yatabe, Y. Oikawa, T. Onuma, and H. Niwa, "Optical visualization of sound source of edge tone using parallel phase-shifting interferometry," 47th International Congress and Exposition on Noise Control Engineering (inter-noise), Illinois, Aug. 2018.
3. D. Hermawanto, K. Ishikawa, K. Yatabe, and Y. Oikawa, "Measurement of sound pressure inside tube using optical interferometry," 47th International Congress and Exposition on Noise Control Engineering (inter-noise), Illinois, Aug. 2018.
4. Y. Oikawa, K. Ishikawa, K. Yatabe, T. Onuma, and H. Niwa, "Seeing the sound we hear: Optical technologies for visualizing sound wave," Three-dimensional Imaging, Visualization, and Display, Florida, Apr. 2018.
5. R. Tanigawa, K. Ishikawa, K. Yatabe, Y. Oikawa, T. Onuma, and H. Niwa, "Simultaneous visualization of flow and sound using parallel phase-shifting interferometry," 11th Pacific Symposium on Flow Visualization and Image Processing (PSFVIP), Kumamoto, Dec. 2017.
6. K. Ishikawa, R. Tanigawa, K. Yatabe, Y. Oikawa, T. Onuma, and H. Niwa, "Experimental visualization of flow-induced sound using high-speed polarization interferometer," 14th International Conference on Flow Dynamics (ICFD2017), Sendai, Nov. 2017.
7. ◯K. Ishikawa, K. Yatabe, Y. Ikeda, Y. Oikawa, T. Onuma, H. Niwa, and M. Yoshii, "Interferometric imaging of acoustical phenomena using high-speed polarization camera and 4-step parallel phase-shifting technique," Proc. SPIE 10328, Selected Papers from the 31st International Congress on High-Speed Imaging and Photonics, 103280I (2017).

8. ◯K. Ishikawa, K. Yatabe, Y. Ikeda, Y. Oikawa, T. Onuma, H. Niwa, and M. Yoshii, "Optical sensing of sound fields: Non-contact, quantitative, and single-shot imaging of sound using high-speed polarization camera," 5th Joint Meeting of Acoustical Society of America and Acoustical Society of Japan, Hawaii, Nov.–Dec. 2016.

9. K. Yatabe, K. Ishikawa, and Y. Oikawa "Signal processing for optical sound field measurement and visualization," 5th Joint Meeting of Acoustical Society of America and Acoustical Society of Japan, Hawaii, Nov.–Dec. 2016.

10. Y. Oikawa, K. Yatabe, K. Ishikawa, and Y. Ikeda, "Optical sound field measurement and imaging using laser and high-speed camera," 45th International Congress and Exposition on Noise Control Engineering (inter-noise), Hamburg, Aug. 2016.

11. K. Ishikawa, K. Yatabe, Y. Ikeda, and Y. Oikawa, "Numerical analysis of acousto-optic effect caused by audible sound based on geometrical optics," 12th Western Pacific Acoustics Conference, pp.165–169, 2015.

Domestic conference

1. 石川憲治，谷川理佐子，南翔汰，矢田部浩平，及川靖広,"早稲田大学本庄キャンパスに構築した音響光計測実験室," 日本音響学会講演論文集, pp. 305–306, Sep. 2018.

2. 谷川理佐子，石川憲治，矢田部浩平，及川靖広, "光学的可視化における空間周波数フィルタを用いた流れと音の分離," 日本音響学会講演論文集, pp. 517–518, Sep. 2018.

3. 今枝文彦，石川憲治，矢田部浩平，及川靖広, "１万チャネル音響データに対する部分空間法を用いたノイズ除去," 日本音響学会講演論文集, pp. 147–148, Sep. 2018.

4. 石川憲治， 矢田部浩平, 及川靖広, 大沼隼志, 丹羽隼人, "偏光高速度干渉計を用いた軸対称音場の３次元・瞬時・定量可視化計測," 日本音響学会講演論文集, pp. 625–626, Mar. 2018.

5. 谷川理佐子, 石川憲治， 矢田部浩平, 及川靖広, 大沼隼志, 丹羽隼人, "偏光高速度干渉計を用いた空力音の可視化," 日本音響学会講演論文集, pp. 865–866, Mar. 2018.

6. 矢田部浩平, 石川憲治， 及川靖広, "レーザ干渉計による音圧分布の非接触計測 ~ これまでの動向と近年の発展~ ," 信学技報, vol.117, no.399, pp.33–40, 2018.

7. 石川憲治， 谷川理佐子, 矢田部浩平, 及川靖広, 大沼隼志, 丹羽隼人, “偏光高速度干渉計を用いた音場イメージング計測法の原理と応用, ” 日本音響学会アコースティックイメージング研究会資料, AI-2017-24, Oct. 2017.

8. 石川憲治， 谷川理佐子, 矢田部浩平, 及川靖広, 大沼隼志, 丹羽隼人, “偏光高速度干渉計を用いた透明筐体内部音場の 2 次元イメージング計測,” 日本音響学会講演論文集, pp. 489–490, Sep. 2017.

9. D. Hermawanto, K. Ishikawa, K. Yatabe, and Y. Oikawa, “Very near field sound pressure visualization of MEMS microphone by optical interferometer,” 日本音響学会講演論文集, pp. 633–634, Sep. 2017.

10. 谷川理佐子, 石川憲治， 矢田部浩平, 及川靖広, 大沼隼志, 丹羽隼人,“流れと音の光学的可視化のための流体温度調節法,” 日本音響学会講演論文集, pp. 1257–1258, Sep. 2017.

11. 石川憲治， 矢田部浩平, 池田雄介, 及川靖広, 大沼隼志, 丹羽隼人,“光による音場イメージング計測法の楽器計測への応用,” 日本音響学会講演論文集, pp. 1323–1324, Mar. 2017.

12. 谷川理佐子, 石川憲治， 矢田部浩平, 池田雄介, 及川靖広, 大沼隼志, 丹羽隼人,“偏光高速度干渉計を用いた流れと音の同時可視化,” 日本音響学会講演論文集, pp. 1125–1126, Mar. 2017.

13. 矢田部浩平, 石川憲治， 及川靖広,“音の光干渉計測のための干渉縞解析,” 日本音響学会講演論文集, pp.633–634, Mar. 2017.

14. 石川憲治， 矢田部浩平, 池田雄介, 及川靖広, 大沼隼志, 丹羽隼人,“偏光高速度干渉計によるスピーカ放射音場の 1mm 分解能イメージング計測,” 日本音響学会講演論文集, pp. 343–344, Sep. 2016.

15. 矢田部浩平, 石川憲治， 及川靖広,“Herglotz 波動関数の球面調和関数展開による光学的測定データからの三次元音場復元,” 日本音響学会講演論文集, pp. 387–388, Sep. 2016.

16. 石川 憲治, 矢田部 浩平, Nachanant Chitanont, 池田 雄介, 及川 靖広, 大沼 隼志, 丹羽 隼人,“偏光高速度干渉計を用いた定量的かつサブミリメートルの空間分解能を持つ光学的音場計測法,” 日本音響学会講演論文集, pp. 593–594, Mar. 2016.

17. 石川 憲治, 矢田部 浩平, 池田 雄介, 及川 靖広,“空気中可聴音場による光波変調のモデル化に関する検討,” 日本音響学会講演論文集, pp. 559–560, Sep. 2015.

18. 矢田部浩平, 石川憲治， 池田雄介, 及川靖広,“光を使って音を録る ~ 光学的音響測定とその信号処理~ ,” 情報処理学会研究報告, vol.2015-MUS-107, no.11, pp.1–6, May 2015.

Other

1. INCE Young Professional Congress Attendance Grants (YP Grants) in 47th International Congress on Noise Control Engineering (INTER-NOISE 2018).

2. Spotlight on Optics, Mar. 2018. (Simultaneous imaging of flow and sound using high-speed parallel phase-shifting interferometry, Opt. Lett., 2018)

3. 及川靖広, 石川憲治, 大沼隼志, “偏光高速度カメラによる音のイメージング計測,” O plus E, vol.39, no.3, pp.264–268, 2017.

4. 及川靖広, 矢田部浩平, 石川憲治, “音を撮影するカメラ~ 偏光高速度干渉計,”Shake Hands, vol.5, pp.8–9, Sep. 2017.

5. 竹内大起，山中悠勢，石川憲治，池田雄介，及川靖広,“三次元音場創生を目的とした256ch 高速1bit スピーカシステム,” 日本音響学会講演論文集, pp.633–634, Mar. 2017.

6. 石川憲治, 矢田部浩平, 池田雄介, 及川靖広, “光を用いた音場可視化装置,” 日本音響学会誌, vol.72, no.7, pp.430–431, 2016.

7. 杉山真望, 石川憲治, 矢田部浩平, 池田雄介, 及川靖広,“回転非対称の素子からなる音響メタマテリアルの特性の可視化,” 日本音響学会講演論文集, pp.1107–1108, Sep. 2016.

8. 中村歩己, 矢田部浩平, 石川憲治, 池田雄介, 及川靖広,“フリーリード楽器における空気流出側の構造が発音に与える影響,” 日本音響学会講演論文集, pp.691–692, Sep. 2016.

9. K. Ishikawa, Y. Oikawa, and Y. Yamasaki, “Non-intrusive sound pressure measurement using light scattering,” Acoustical Science and Technology, vol. 36, no. 5, pp. 408–418, 2015.

Award

1. Best Presentation Award in 14th International Conference on Flow Dynamics (ICFD2017).

2. First Prize - Best Student Paper Award in Engineering Acoustics, 5th Joint Meeting of Acoustical Society of America and Acoustical Society of Japan, 2016.

3. 日本音響学会 第42回粟屋潔学術奨励賞, 2017.

4. 日本音響学会 第13回学生優秀発表賞, 2016.